The Astrophysical Journal Supplement Series, 219:18 (36pp), 2015 August doi:10.1088/0067-0049/219/2/18

A *HERSCHEL* STUDY OF 24 μm-SELECTED AGNs AND THEIR HOST GALAXIES

Lei Xu[1], G. H. Rieke[1], E. Egami[1], M. J. Pereira[1], C. P. Haines[1,2], and G. P. Smith[3]
[1] Steward Observatory, 933 N. Cherry Ave, University of Arizona, Tucson, AZ 85721, USA
[2] Departamento de Astronoma, Universidad de Chile, Casilla 36-D, Correo Central, Santiago, Chile
[3] School of Physics and Astronomy, University of Birmingham, Birmingham B15 2TT, UK
Received 2014 February 18; accepted 2015 April 30; published 2015 July 30

ABSTRACT

We present a sample of 290 24 μm-selected active galactic nuclei (AGNs) mostly at $z \sim 0.3$–2.5, within 5.2 deg^2 distributed as $25' \times 25'$ fields around each of 30 galaxy clusters in the Local Cluster Substructure Survey. The sample is nearly complete to 1 mJy at 24 μm, and has a rich multiwavelength set of ancillary data; 162 are detected by *Herschel*. We use spectral templates for AGNs, stellar populations, and infrared (IR) emission by star-forming galaxies to decompose the spectral energy distributions (SEDs) of these AGNs and their host galaxies, and estimate their star formation rates, AGN luminosities, and host galaxy stellar masses. The set of templates is relatively simple: a standard Type-1 quasar template; another for the photospheric output of the stellar population; and a far-infrared star-forming template. For the Type-2 AGN SEDs, we substitute templates including internal obscuration, and some Type-1 objects require a warm component ($T \gtrsim 50$ K). The individually *Herschel*-detected Type-1 AGNs and a subset of 17 Type-2 AGNs typically have luminosities $>10^{45}$ ergs s^{-1}, and supermassive black holes of $\sim 3 \times 10^8\ M_\odot$ emitting at ~10% of the Eddington rate. We find them in about twice the numbers of AGNs identified in SDSS data in the same fields, i.e., they represent typical high-luminosity AGNs, not an IR-selected minority. These AGNs and their host galaxies are studied further in an accompanying paper.

Key words: galaxies: active – infrared: galaxies – quasars: general

1. INTRODUCTION

The bright continua of active galactic nuclei (AGNs) in the X-ray, UV, and optical are powered directly by accretion—the growth of supermassive black holes (SMBHs). At the current epoch, there is a tight correlation between the SMBH masses and the host galaxy stellar bulge masses, indicating a link between the integrated accretion by black holes and the star formation in their host galaxies (e.g., Magorrian et al. 1998; Tremaine et al. 2002). The level of accretion is indicated by a variety of metrics, e.g., X-rays, optical emission lines, and optical–IR continua. These indicators can drown out many metrics for the level of star formation, but it is thought that the far-infrared (FIR) emission remains dominated by this mechanism, providing a strong motivation for studies of the FIR outputs of galaxies with active nuclei.

Prior to *Herschel*, the measurements of rest-frame FIR emission from luminous AGNs were limited to a small population (e.g., Omont et al. 2001; Haas et al. 2003; Dicken et al. 2008). With the advent of *Herschel*, it is possible to study the FIR properties efficiently for a large sample of AGNs (e.g., Hatziminaoglou et al. 2010; Shao et al. 2010; Mullaney et al. 2012; Leipski et al. 2013, 2014; Rosario et al. 2013). To augment these studies, we describe *Herschel* measurements of 205 Type-1 AGNs uniformly selected from a 5.2 deg^2 survey area; the sample is nearly complete at 24 μm down to 1 mJy, and verified by spectroscopy. These AGNs are complemented by 85 Type-2 objects similarly selected from a 3.6 deg^2 subset of the same data. A multiband data set from the UV to the FIR, including optical spectroscopy, allows detailed study of the AGNs and their host galaxies in this sample. We use spectral templates for (1) the UV to FIR output of AGNs; (2) stellar populations; and (3) the infrared (IR) emission of star-forming galaxies to decompose their spectral energy distributions (SEDs) and estimate their IR star formation luminosities, AGN luminosities, and their host galaxy stellar masses. The black hole masses are estimated from the Type-1 AGN broad optical emission lines, and from the stellar masses for the Type-2 objects. More than 55% of the sample are detected individually by *Herschel*, and we stack the signals from the rest for comparison purposes. This paper presents the data and a basic analysis; in a companion paper (Xu et al. 2015), we use these results to explore the evolutionary stage of the AGN host galaxies—whether they are starbursting or normal star-forming galaxies; and whether there is a causal connection between nuclear and star formation (SF) activity for these objects.

This paper is structured as follows. In Section 2 we present the data, and in Section 3 we describe the selection and completeness of our sample of Type-1 AGNs. We also show their SEDs and discuss the FIR excesses. Section 4 is a parallel discussion of the Type-2 objects. In Section 5 we analyze both samples together, calculating the physical properties of the AGNs and their host galaxies, such as Eddington rates, host stellar masses, and star formation rates (SFRs). A summary is provided in Section 6. Throughout this paper we assume $\Omega_M = 0.3$, $\Omega_\Lambda = 0.7$, and $H_0 = 70$ km s^{-1} Mpc^{-1}.

2. DATA

2.1. LIRAS: Local Cluster Substructure Survey (LoCuSS) IR AGN Survey

LoCuSS[4] is a large survey of X-ray-luminous galaxy clusters at $z = 0.15$–0.3 (e.g., Smith et al. 2010). This paper exploits the extensive LoCuSS multiwavelength data set for 30 clusters, which includes data from *Chandra*, *GALEX*, SUBARU, United Kingdom IR Telescope (UKIRT), *Spitzer*/MIPS, and *Herschel*. The *Spitzer* and *Herschel* data cover a total area of ~5.2 deg^2 ($25' \times 25' \times 30$), at the central coordinates listed in Table 1.

[4] http://www.sr.bham.ac.uk/locuss/

Table 1
Cluster Fields

Cluster	R.A. (J2000)	Decl. (J2000)	Redshift
A68	00:37:05.28	+09:09:10.8	0.255
A115	00:55:50.65	+26:24:38.7	0.197
Z348[a]	01:06:49.50	+01:03:22.1	0.160
A209	01:31:53.00	−13:36:34.0	0.206
RXJ0142	01:42:02.64	+21:31:19.2	0.280
A267[a]	01:52:48.72	+01:01:08.4	0.230
A291	02:01:43.11	−02:11:48.1	0.196
A383[a]	02:48:02.00	−03:32:15.0	0.188
A586[a]	07:32:20.42	+31:37:58.8	0.171
A611[a]	08:00:55.92	+36:03:39.6	0.288
Z1693[a]	08:25:57.84	+04:14:47.5	0.225
A665[a]	08:30:57.36	+65:51:14.4	0.182
A689[a]	08:37:24.57	+14:58:21.1	0.279
Z1883[a]	08:42:56.06	+29:27:25.7	0.194
A697[a]	08:42:57.69	+36:21:58.5	0.282
Z2089[a]	09:00:36.86	+20:53:40.0	0.235
A963[a]	10:17:01.20	+39:01:44.4	0.205
A1689[a]	13:11:30.00	−01:20:07.0	0.183
A1758[a]	13:32:44.47	+50:32:30.5	0.280
A1763[a]	13:35:16.32	+40:59:45.6	0.228
A1835[a]	14:01:02.40	+02:52:55.2	0.253
A1914	14:25:59.78	+37:49:29.1	0.171
Z7160[a]	14:57:15.23	+22:20:34.0	0.258
A2218	16:35:52.80	+66:12:50.4	0.171
A2219[a]	16:40:22.56	+46:42:21.6	0.228
RXJ1720[a]	17:20:10.14	+26:37:30.9	0.164
A2345	21:27:13.73	−12:09:46.1	0.176
RXJ2129[a]	21:29:40.02	+00:05:20.9	0.235
A2390	21:53:36.72	+17:41:31.2	0.233
A2485	22:48:31.13	−16:06:25.6	0.247

Note.
[a] Type-2 AGNs are selected using MMT/Hectospec spectra in these 21 cluster fields. Because the selection depends on emission line ratios, we did not select Type-2 AGNs in 9 cluster fields where the spectra were not flux-calibrated due to the lack of standard stars.

Since most cluster members are members of the old galaxy population, which is not bright in the mid-infrared (MIR) and FIR, this wide-field coverage allows us to conduct a serendipitous AGN survey independent of the existence of galaxy clusters in the observed fields. In LIRAS, we take advantage of these multiwavelength data sets (described in this section) to study the properties of a 24 μm-selected IR-luminous Type-1 AGN sample over the entire 5.2 deg^2 area (as discussed in Section 3 below). In Section 4, we show how we also identified Type-2 AGNs selected from 21 out of the 30 cluster fields (i.e., 3.6 deg^2), as indicated in Table 1.

2.2. Mid-infrared Observations

Each cluster field was observed at 24 μm between 2007 November and 2008 November with MIPS (Rieke et al. 2004) on *Spitzer* (Werner et al. 2004), utilizing a 5 × 5 grid of pointings in fixed cluster or raster mode (PID: 40872; PI: G.P. Smith). Two cycles of small-field photometry with a frame time of 3 s were performed at each grid point, for a total per pixel exposure time of 90 s. The central 5′ × 5′ of some clusters had already been imaged by GTO program 83 to greater depth (~3000 s pixel^{-1}). All the available data were combined for our survey. The images were processed with the MIPS Data Analysis Tool (DAT; Gordon et al. 2005). The beam size at 24 μm is 5.″9 with 2.″49 pixel; the images were combined with a pixel scale of 1.″245, half the physical pixel scale. The 24 μm fluxes were measured by SExtractor (Bertin & Arnouts 1996) within a fixed circular aperture of diameter 21″ and with an aperture correction of a factor 1.29. The 90% completeness limits at 24 μm are in the range 300–500 μJy. Details of the reduction, source extraction, and photometry can be found in Haines et al. (2009).

WISE[5] data are also available in our survey fields. We utilize *WISE* 3.4, 4.6, and 12 μm measurements in our SED decomposition fitting. The detection limit at 22 μm is 6 mJy, an order of magnitude higher than achieved with MIPS. Since this band is so close to the MIPS 24 μm one, we do not use it.

2.3. Far-infrared Data

Our *Herschel* (Pilbratt et al. 2010) data were taken between 2009 December 22 and 2011 October 10 (LoCuSS *Herschel* Key Programme, Smith et al. 2010). Each cluster field was observed with both the Photodetector Array Camera and Spectrometer (PACS; Poglitsch et al. 2010) at 100 and 160 μm, and the Spectral and Photometric Imaging Receiver (SPIRE; Griffin et al. 2010) at 250, 350, and 500 μm. The images were reduced using HIPE V6.0 (Ott 2010). Because the PACS images are relatively shallow and the beam size is relatively small, confusion is not an issue and the photometry could be performed with SExtractor. However, confusion is an issue for the SPIRE data. Therefore the photometry of the SPIRE images was performed with IRAF/DAOphot, using the 24 μm source positions (for all sources above the 3σ detection limit) as priors to position the point-spread function (PSF) on the SPIRE maps. We rotated the *Herschel* PSF to match the position angle of each map, registered the 24 μm and *Herschel* maps with the isolated point sources, and then fixed the source positions. We extracted fluxes on the SPIRE maps using the empirical fine-scale PSF provided by the HSC[6] instead of constructing one from our own data, because of the lack of isolated point sources with high signal-to-noise ratio (S/N) on our maps. Parameters adopted for the maps and photometry (such as the pixel size, FWHM of point source, photometry aperture radius, aperture correction, and sky annulus radius) are summarized in Table 2.

2.4. Near-infrared, Optical, and Ultraviolet Data

Near-infrared (NIR) images of 26 of the 30 cluster fields were obtained with WFCAM (Casali et al. 2007) at J- and K-bands on the 3.8 m UKIRT in service mode over multiple semesters starting in 2008 March. The data acquisition used the same strategy as was used by the UKIDSS Deep Extragalactic Survey (Lawrence et al. 2007), covering 52′ × 52′ to depths of $J \sim 21$, $K \sim 19$, with exposure times of 640 s, pixel size of 0.″2 (half the physical pixel size) and PSF FWHMs ~0.″7–1.″2. The remaining four cluster fields were observed with NEWFIRM on the 4.0 m Mayall telescope at Kitt Peak on 2008 May 17 and 2008 December 28. The NEWFIRM data consist of dithered and stacked J- and *K*-band images covering fields of 27′ × 27′ with a 0.″4 pixel scale and PSF FWHM ~1.″0–1.″5. The total exposure times in each filter were 1800 s, and the images also reach depths of $J \sim 21$ mag and $K \sim 19$ mag (Vega, 5σ).

[5] http://irsa.ipac.caltech.edu/Missions/wise.html
[6] ftp://ftp.sciops.esa.int/pub/hsc-calibration/SPIRE/PHOT/Beams_v1.0_old/beam_release_note_v1-1.pdf

Table 2
Herschel Photometry Parameters

Parameter	Units	100 μm	160 μm	250 μm	350 μm	500 μm
Pixel size	arcsec	3	3	6	9	12
FWHM	arcsec	6.8	11.4	18.1	24.8	36.6
Photometry radius	arcsec	6	12	22	27	36
Aperture correction	arcsec	1.706	1.499	1.229	1.120	1.211
Sky annulus	arcsec	N/A	N/A	24–60	36–90	48–120

SDSS photometry (Data Release 7) is available for 26 out of 30 cluster fields, covering a total of 4.51 deg^2 survey area. The SDSS five-band photometry we used is corrected for Galactic extinction. Optical images in R or I band using Subaru/Suprime-Cam (Okabe et al. 2010) with seeing $\sim$0.″6 allow us to study the morphology of the Type-2 AGN hosts (see Appendix A). The data were reduced as described by Okabe & Umetsu (2008), using the Suprime-Cam pipeline software SDFRED for flat-fielding, instrumental distortion correction, differential refraction, PSF matching, sky subtraction, and stacking. The astrometric solution was based on 2MASS stars. Standard stars were interspersed with the cluster imaging. Further information about the optical imaging, including the initial publication of the data for most of the clusters, can be found in Okabe et al. (2010).

GALEX near-UV observations were obtained for 26 of the cluster fields (omitting those for A586, A689, A2485, and RXJ0142), and simultaneously in the far-UV for 21 fields under Guest Investigator Programs GI4-090 and GI6-046 (PIs G.P. Smith and S. Moran, respectively). The exposure times ranged from 3 to 29 ks; additional details about these observations and their reduction can be found in Haines et al. (2015).

2.5. Chandra X-ray Imaging

Twenty-one of the thirty clusters were observed with *Chandra* in the I mode of the ACIS-I, which has a field of view (FOV) of 16.′9 × 16.′9. Seven more were observed with the ACIS-S (8.′3 × 8.′3 FOV). Two of the clusters (Abell 2345 and Abell 291) do not have X-ray data. The exposure times for the cluster fields range from 10 to 100 ks (Table 1 in Haines et al. 2012), with a typical integration time of 20 ks.

Sanderson et al. (2009) discuss the reduction and analysis of the X-ray observations. To detect X-ray point sources that are potential AGNs, we used the wavelet-detection algorithm CIAO WAVDETECT; a minimum of six counts in the broad energy range (0.3–7 keV) was the threshold for source detection. The observations in this band were converted to fluxes assuming a $\Gamma = 1.7$ power-law spectrum with Galactic absorption, following Kenter et al. (2005). The X-ray flux sensitivity limit for the cluster fields ranges from 6×10^{-16} to 8×10^{-15} erg cm^{-2} s^{-1} with a median of 3.5×10^{-15} erg cm^{-2} s^{-1}. We calculated the luminosities for all sources with redshifts, assuming K-corrections of the form $(1 + z)^{\Gamma-2}$. We also calculated the X-ray luminosity limit for each non-detected AGN.

2.6. Spectroscopic Data

We use spectra from the Arizona Cluster Redshift Survey (ACReS; M. J. Pereira et al. 2015, in preparation), a long-term spectroscopic program to observe the fields of the 30 galaxy clusters with MMT/Hectospec. Hectospec is a 300 fiber multi-object spectrograph with a circular FOV of 1° diameter (Fabricant et al. 2005) and fibers that project to 1.″5 on the sky, mounted on the 6.5 m MMT at Mount Hopkins, Arizona. We used the 270 line grating, which provides a wide wavelength range (3650–9200 Å) at 6.2 Å resolution ($R = 1000$). This ensures coverage of the most important emission lines suitable for identifying AGNs. The spectroscopy data were reduced using HSRED.[7] Redshifts were determined by comparison of the reduced spectra with stellar, galaxy, and quasar template spectra, choosing the template and redshift that minimized the χ^2 between model and data. The target selection is described in detail in Haines et al. (2013). Virtually all sources with 24 μm flux above 1 mJy, and K-band $<$19 mag, were targeted by Hectospec. See Section 3 and Appendix B for a summary of the spectroscopic coverage of the 24 μm sources.

3. 24 μm-SELECTED TYPE-1 AGNs

The MIR continuum emission of Type-1 AGNs arises from warm dust heated by the AGN (e.g., Rieke 1978; Polletta et al. 2000; Haas et al. 2003), and on average there are only modest variations among quasars in the average fraction of the bolometric luminosity emitted at these wavelengths (Krawczyk et al. 2013). Therefore, the 24 μm selection of Type-1 AGNs is expected to be highly efficient and complete.

3.1. Type-1 AGN Identification

3.1.1. Approach

Members of our sample of LIRAS Type-1 AGNs (see Table 3 for those detected and Table 4 for those undetected with *Herschel*) were required to have:

1. *Spitzer*/MIPS 24 μm flux densities above 1 mJy; and
2. optical spectra showing broad emission lines with FWHM $>$ 1200 km s^{-1}.

All sources in the surveyed regions with 24 μm flux densities above 1 mJy and with K-band $<$19 mag were given the highest priority for spectroscopy, irrespective of NIR color or morphology (resolved/unresolved in the NIR). We excluded those that were clearly stars (being both unresolved in the K-band data and having blue NIR colors ($J - K < 1.0$)) and asteroids (very luminous at 24 μm, but with no counterparts in all other bands). Over the 5.2 deg^2 survey area covered at both 24 μm and in the *Herschel* bands, there were 2439 sources with 24 μm flux density above 1 mJy, of which 1827 remained after excluding stars, asteroids, and sources with no optical/NIR counterparts. From this list, 1729 sources were observed with Hectospec while another 18 have spectra from SDSS. Therefore, the completeness of spectroscopic coverage is about 94.6% (see Appendix B for a summary of the reasons that we

[7] http://mmto.org/~rcool/

Table 3
Fluxes of the 24 μm-selected *Herschel*-detected Type-1 AGN Sample[a]

#	Source LIRAS	R.A. (J2000)	Decl. (J2000)	J (mJy)	K (mJy)	3.4 μm (mJy)	4.6 μm (mJy)	12 μm (mJy)	24 μm (mJy)	100 μm (mJy)	160 μm (mJy)	250 μm (mJy)	350 μm (mJy)	500 μm (mJy)
1	J024818.61−031956.9	42.0775358	−3.3324640	1.131	1.784	1.52	1.54	4.26	8.27	42.58	60.40	53.94	35.84	24.08
2	J020120.00−022447.7	30.3333465	−2.4132541	1.361	2.683	2.63	3.57	10.36	18.43	98.39	49.37	49.65	14.15	<12.39
3	J212928.91+000415.9	322.3704400	0.0710740	0.518	0.833	0.46	0.44	1.09	2.56	24.91	42.34	26.08	<10.99	<12.39
4	J073243.17+314111.4	113.1798658	31.6865098	0.279	0.527	0.50	0.54	1.32	3.05	<10.89	24.61	15.24	14.19	<12.39
5	J082626.42+041231.0	126.6100938	4.2086221	0.143	0.300	0.25	0.25	0.56	1.37	11.40	<16.89	<10.19	<10.99	<12.39
6	J084352.28+292854.0	130.9678493	29.4819339	0.378	0.686	0.42	0.36	0.80	1.33	<10.89	<16.89	11.68	<10.99	<12.39
7	J014200.86+213752.6	25.5035744	21.6312836	0.095	0.186	0.16	0.18	0.46	1.13	19.02	32.18	13.94	<10.99	<12.39
8	J212930.74+001347.2	322.3781001	0.2297864	0.548	1.732	3.13	4.33	8.45	17.72	68.90	65.95	32.71	16.75	<12.39
9	J003730.63+092255.6	9.3776456	9.3821238	0.188	0.386	0.40	0.44	1.04	1.88	<10.89	<16.89	34.70	31.54	12.86
10	J212911.74−000438.2	322.2989151	−0.0772764	0.186	0.407	0.31	0.30	0.90	3.88	28.64	<16.89	12.57	<10.99	<12.39
11	J024838.05−031730.8	42.1585241	−3.2918841	0.224	0.419	0.36	0.34	1.08	2.95	<10.89	<16.89	31.41	20.29	<12.39
12	J212629.76−120555.5	321.6239890	−12.0987418	0.060	0.114	0.00	0.00	0.00	2.33	28.19	55.71	30.70	11.73	<12.39
13	J084234.94+362503.2	130.6455700	36.4175490	0.038	0.055	0.40	0.31	1.09	7.38	<10.89	<16.89	27.66	11.63	<12.39
14	J080126.90+360059.1	120.3620723	36.0164225	0.100	0.186	0.19	0.12	0.29	1.07	<10.89	<16.89	19.95	<10.99	<12.39
15	J215343.83+172912.9	328.4326439	17.4869215	0.113	0.293	0.38	0.38	1.91	3.11	139.65	168.22	90.85	54.25	23.56
16	J083107.34+654653.9	127.7806029	65.7816461	0.190	0.425	0.87	1.36	3.39	6.23	59.62	75.03	47.68	30.40	<12.39
17	J080013.86+355831.3	120.0577417	35.9753679	0.163	0.324	0.70	1.18	2.86	5.17	33.37	30.14	40.47	13.26	<12.39
18	J164110.54+464911.8	250.2939165	46.8199518	0.108	0.163	0.30	0.43	1.00	2.41	<10.89	<16.89	14.80	19.75	14.42
19	J090026.52+204158.8	135.1104847	20.6996599	0.331	0.948	2.48	4.45	11.44	19.95	72.89	75.44	68.22	31.57	<12.39
20	J083118.85+660117.8	127.8285389	66.0216065	0.080	0.173	0.23	0.24	0.84	1.98	22.33	26.44	33.63	13.22	<12.39
21	J084256.20+361325.3	130.7341671	36.2236985	0.094	0.204	0.49	0.94	2.01	4.98	27.68	30.85	13.14	<10.99	16.13
22	J163934.02+464314.2	249.8917588	46.7206074	0.119	0.227	0.34	0.39	0.95	1.46	20.57	27.10	25.14	16.35	<12.39
23	J073155.69+312529.2	112.9820625	31.4247697	0.062	0.130	0.16	0.16	0.57	1.71	<10.89	<16.89	25.44	17.08	<12.39
24	J080108.38+355222.4	120.2849374	35.8728943	0.114	0.201	0.36	0.63	1.83	4.60	11.14	<16.89	12.76	<10.99	<12.39
25	J083747.73+145041.6	129.4488867	14.8448955	0.049	0.135	0.23	0.43	0.90	2.49	<10.89	<16.89	27.79	18.76	<12.39
26	J101708.92+385557.6	154.2871852	38.9326698	0.135	0.211	0.38	0.46	1.03	1.70	12.27	<16.89	<10.19	<10.99	<12.39
27	J014245.21+213449.8	25.6883589	21.5804995	0.161	0.414	1.02	1.65	2.64	3.95	36.50	<16.89	33.88	24.57	14.41
28	J082949.41+653919.8	127.4558897	65.6555134	0.050	0.094	0.16	0.23	0.72	2.23	24.38	24.74	40.99	30.31	14.14
29	J015215.36+010514.9	28.0639854	1.0874585	0.045	0.051	0.00	0.00	0.00	1.02	<10.89	<16.89	24.95	14.14	<12.39
30	J101755.30+390430.8	154.4804209	39.0752210	0.198	0.258	0.44	0.61	1.47	3.81	11.62	40.50	40.54	23.40	20.05
31	J131206.62−013129.0	198.0275910	−1.5249945	0.087	0.195	0.35	0.42	0.88	1.95	52.52	79.32	54.24	31.89	<12.39
32	J212720.66−120612.9	321.8361015	−12.1035767	0.047	0.081	0.15	0.13	0.57	1.35	11.80	19.57	27.06	17.32	<12.39
33	J133529.41+405828.0	203.8725321	40.9747129	0.040	0.100	0.18	0.16	0.72	1.47	28.20	87.16	63.26	57.70	<12.39
34	J131107.34−012857.9	197.7805951	−1.4827610	0.092	0.134	0.29	0.42	1.20	1.50	<10.89	21.48	27.87	26.33	18.27
35	J133434.70+410623.4	203.6445956	41.1064984	0.111	0.146	0.34	0.54	1.54	4.68	16.77	<16.89	30.47	22.10	<12.39
36	J145639.07+222516.6	224.1627999	22.4212821	0.113	0.177	0.25	0.37	0.96	2.00	33.35	26.41	29.24	13.79	<12.39
37	J083008.79+654521.5	127.5366098	65.7559612	0.106	0.156	0.32	0.44	1.05	4.07	16.85	<16.89	29.21	15.42	<12.39
38	J145816.29+222625.1	224.5678757	22.4403190	0.296	0.299	0.49	0.88	2.05	3.85	<10.89	<16.89	16.02	22.72	23.23
39	J083806.01+150827.3	129.5250425	15.1409106	0.054	0.084	0.15	0.22	0.43	1.50	<10.89	<16.89	28.86	20.30	<12.39
40	J140130.51+030358.0	210.3771116	3.0661160	0.076	0.102	0.27	0.35	0.43	1.42	<10.89	17.92	11.47	13.75	<12.39
41	J101730.81+384941.5	154.3783933	38.8281933	0.046	0.069	0.11	0.12	0.30	1.45	17.39	<16.89	18.04	15.16	<12.39
42	J131109.29−011953.9	197.7887054	−1.3316458	0.019	0.038	0.09	0.14	0.59	1.06	33.01	47.80	44.99	40.66	21.90
43	J133549.20+411306.1	203.9550015	41.2183561	0.041	0.070	0.00	0.00	0.00	1.89	18.25	25.92	22.71	22.14	<12.39
44	J212738.37−120050.6	321.9098789	−12.0140684	0.027	0.064	0.10	0.15	0.53	1.19	11.31	<16.89	14.61	17.67	<12.39
45	J131109.74−011329.8	197.7905847	−1.2249454	0.038	0.089	0.20	0.24	0.83	1.59	14.25	17.67	30.61	24.03	26.17
46	J073247.15+313429.5	113.1964456	31.5748536	0.046	0.076	0.00	0.00	0.00	3.34	27.29	19.46	32.50	17.54	<12.39
47	J164020.70+465142.6	250.0862632	46.8618386	0.057	0.086	0.18	0.29	0.72	1.58	<10.89	<16.89	18.26	11.17	<12.39

Table 3
(Continued)

#	Source LIRAS	R.A. (J2000)	Decl. (J2000)	J (mJy)	K (mJy)	3.4 μm (mJy)	4.6 μm (mJy)	12 μm (mJy)	24 μm (mJy)	100 μm (mJy)	160 μm (mJy)	250 μm (mJy)	350 μm (mJy)	500 μm (mJy)
48	J164116.66+463946.3	250.3194325	46.6628720	0.183	0.230	0.47	0.90	2.04	2.84	14.53	<16.89	<10.19	<10.99	<12.39
49	J084319.21+361606.9	130.8300428	36.2685810	0.049	0.103	0.20	0.39	1.09	2.94	17.10	<16.89	10.71	19.34	<12.39
50	J224837.78−160109.3	342.1574051	−16.0192436	0.071	0.126	0.24	0.40	0.88	2.41	18.50	<16.89	25.02	13.58	<12.39
51	J020239.22−020600.2	30.6634169	−2.1000425	0.072	0.108	0.24	0.48	1.30	2.82	21.28	29.21	23.79	24.30	14.18
52	J015248.43+011442.0	28.2017783	1.2452652	0.088	0.127	0.30	0.58	1.21	2.42	<10.89	<16.89	33.32	23.14	14.12
53	J133314.82+504526.8	203.3117652	50.7574571	0.069	0.090	0.13	0.23	0.65	1.27	<10.89	<16.89	29.45	29.43	<12.39
54	J224822.19−160711.3	342.0924580	−16.1198104	0.035	0.060	0.10	0.16	0.44	1.58	<10.89	22.45	15.93	22.85	<12.39
55	J224820.85−155924.5	342.0868693	−15.9901359	0.045	0.068	0.00	0.00	0.00	1.24	<10.89	<16.89	16.16	11.41	19.87
56	J133240.79+502434.8	203.1699751	50.4096687	0.078	0.128	0.27	0.44	0.97	2.61	29.14	41.97	40.77	25.30	<12.39
57	J133614.87+411012.4	204.0619636	41.1701002	0.033	0.073	0.12	0.24	0.75	2.17	<10.89	<16.89	48.97	38.51	<12.39
58	J014126.62+212425.3	25.3609052	21.4070315	0.047	0.071	0.12	0.18	0.28	1.69	<10.89	<16.89	16.92	18.95	<12.39
59	J212747.81−115844.5	321.9492125	−11.9790366	0.097	0.123	0.34	0.52	0.82	2.94	<10.89	<16.89	11.76	21.68	15.24
60	J010614.38+011409.6	16.5598973	1.2359962	0.106	0.138	0.27	0.51	0.72	2.97	26.82	62.98	57.48	56.76	36.45
61	J014103.82+213228.7	25.2659030	21.5412923	0.079	0.093	0.13	0.25	0.79	1.46	<10.89	<16.89	10.78	12.78	<12.39
62	J010702.23+005542.0	16.7593042	0.9283422	0.042	0.065	0.00	0.00	0.00	1.00	17.70	<16.89	24.48	12.91	<12.39
63	J073209.94+314143.0	113.0414068	31.6952905	0.048	0.076	0.11	0.20	0.73	1.28	<10.89	<16.89	15.54	16.94	<12.39
64	J015243.29+011219.7	28.1803566	1.2054624	0.128	0.127	0.19	0.34	1.30	3.29	13.48	<16.89	14.76	<10.99	<12.39
65	J172026.50+263815.0	260.1104332	26.6377714	0.064	0.114	0.23	0.41	1.00	1.72	<10.89	21.45	28.33	31.74	<12.39
66	J133313.92+503107.8	203.3079936	50.5188284	0.053	0.085	0.00	0.00	0.00	2.18	13.02	<16.89	33.23	24.57	<12.39
67	J003622.20+091828.1	9.0924996	9.3077941	0.040	0.058	0.12	0.19	0.00	1.41	<10.89	<16.89	14.40	28.76	<12.39
68	J003749.95+090711.0	9.4581154	9.1197346	0.028	0.036	0.05	0.21	0.00	1.23	14.95	23.65	17.06	13.62	<12.39
69	J215347.97+173756.5	328.4498657	17.6323664	0.048	0.055	0.11	0.22	0.73	1.48	11.74	19.41	18.60	<10.99	<12.39
70	J020144.55−022054.4	30.4356112	−2.3484456	0.067	0.098	0.23	0.43	1.02	1.27	15.41	<16.89	23.37	16.10	16.69
71	J145725.17+223133.8	224.3548667	22.5260544	0.214	0.216	0.28	0.58	2.40	4.64	15.57	<16.89	14.31	12.73	12.44
72	J133543.12+405707.8	203.9296578	40.9521684	0.020	0.032	0.06	0.14	0.45	1.51	41.95	65.91	60.58	36.71	<12.39
73	J133531.44+411617.7	203.8809808	41.2715793	0.042	0.063	0.00	0.00	0.00	1.51	<10.89	<16.89	66.85	46.90	22.85
74	J015335.62+010353.7	28.3983971	1.0649256	0.051	0.084	0.15	0.27	0.49	1.34	<10.89	38.12	48.52	51.91	37.51
75	J003755.90+090031.3	9.4829128	9.0087064	0.178	0.194	0.39	0.66	0.00	4.05	<10.89	<16.89	90.10	72.38	55.63
76	J131129.64−011603.2	197.8734827	−1.2675431	0.054	0.069	0.13	0.20	0.56	1.04	<10.89	<16.89	28.39	27.09	21.82
77	J212849.04+000447.6	322.2043500	0.0798919	0.041	0.078	0.26	0.22	0.56	1.66	<10.89	<16.89	24.18	19.18	<12.39
78	J212947.12+002026.3	322.4463500	0.3406365	0.118	0.148	0.23	0.40	0.87	1.75	<10.89	<16.89	46.46	51.48	20.39
79	J013253.29−133915.7	23.2220565	−13.6543599	0.027	0.034	0.08	0.13	0.46	1.15	<10.89	<16.89	45.24	20.06	<12.39
80	J084304.84+292953.8	130.7701621	29.4982689	0.186	0.179	0.24	0.50	1.58	2.91	15.06	<16.89	14.41	<10.99	13.08
81	J133354.56+410300.1	203.4773481	41.0500296	0.029	0.044	0.06	0.11	0.35	1.03	<10.89	<16.89	20.19	<10.99	<12.39
82	J133526.73+405957.6	203.8613726	40.9993444	0.108	0.128	0.22	0.40	1.38	3.27	<10.89	<16.89	25.25	21.30	18.35
83	J213006.22+001256.8	322.5259072	0.2157857	0.037	0.045	0.09	0.16	0.28	1.10	<10.89	<16.89	23.46	27.14	23.84
84	J163922.35+463428.6	249.8431182	46.5746003	0.016	0.018	0.00	0.00	0.00	1.20	<10.89	33.94	25.84	21.44	<12.39
85	J084327.91+361723.4	130.8662732	36.2898226	0.058	0.068	0.10	0.16	0.76	3.11	27.70	56.25	50.29	50.17	34.46
86	J142539.38+375736.8	216.4141000	37.9602120	0.366	0.424	0.15	0.19	0.80	7.25	33.81	16.98	39.26	32.72	16.34
87	J212939.66+000815.5	322.4152698	0.1376307	0.061	0.061	0.08	0.17	0.85	2.64	23.25	<16.89	26.64	22.08	<12.39
88	J073124.82+314721.2	112.8534058	31.7892242	0.015	0.036	0.00	0.00	0.00	1.11	<10.89	<16.89	34.41	35.61	31.95
89	J163950.35+463327.1	249.9597920	46.5575225	0.091	0.098	0.11	0.19	0.74	1.06	<10.89	<16.89	15.46	12.91	<12.39
90	J090122.68+204446.7	135.3445017	20.7463061	0.504	0.643	0.77	1.13	4.24	8.73	45.48	81.05	88.05	83.41	56.20
91	J020225.55−020258.0	30.6064715	−2.0494553	0.059	0.079	0.07	0.13	0.80	2.23	<10.89	35.24	19.00	20.36	12.50
92	J020101.83−021140.5	30.2576099	−2.1945804	0.101	0.152	0.17	0.34	1.90	2.59	14.04	20.09	34.60	17.72	<12.39
93	J003615.85+091328.2	9.0660365	9.2244886	0.119	0.213	0.18	0.30	0.00	1.81	15.39	<16.89	24.20	21.84	<12.39
94	J084254.20+293748.8	130.7258232	29.6302196	0.026	0.037	0.04	0.08	0.32	1.17	<10.89	<16.89	38.15	25.33	25.48

Table 3
(Continued)

#	Source LIRAS	R.A. (J2000)	Decl. (J2000)	J (mJy)	K (mJy)	3.4 μm (mJy)	4.6 μm (mJy)	12 μm (mJy)	24 μm (mJy)	100 μm (mJy)	160 μm (mJy)	250 μm (mJy)	350 μm (mJy)	500 μm (mJy)
95	J084306.40+293922.2	130.7766462	29.6561679	0.123	0.153	0.11	0.22	0.85	1.79	14.18	<16.89	21.30	28.32	12.81
96	J003706.97+091222.0	9.2790209	9.2061131	0.035	0.068	0.06	0.16	0.00	1.19	<10.89	<16.89	13.80	20.42	<12.39
97	J212709.43−120155.1	321.7893060	−12.0319625	0.030	0.059	0.00	0.00	0.00	1.57	19.16	17.66	51.47	63.10	39.86
98	J083758.17+145856.6	129.4923769	14.9823783	0.040	0.076	0.09	0.19	0.57	1.36	<10.89	<16.89	22.74	29.79	19.78
99	J224924.31−161159.9	342.3512838	−16.1999621	0.059	0.126	0.13	0.23	0.65	1.92	<10.89	<16.89	24.43	16.70	19.78
100	J024725.09−033807.9	41.8545485	−3.6355342	0.165	0.265	0.20	0.26	0.94	1.54	11.85	24.03	30.56	32.66	22.13
101	J085941.47+204815.5	134.9228058	20.8043193	0.094	0.110	0.10	0.16	0.45	1.56	<10.89	<16.89	21.75	27.72	34.52
102	J083712.89+145917.4	129.3037182	14.9881780	0.444	0.662	0.49	0.73	3.10	5.62	<10.89	<16.89	31.97	25.45	14.58
103	J131119.24−012030.9	197.8301773	−1.3419133	0.289	0.329	0.35	0.55	3.31	5.97	26.36	16.99	12.57	<10.99	<12.39
104	J163641.18+660848.3	249.1715675	66.1467513	0.069	0.137	0.18	0.19	0.62	1.67	<10.89	<16.89	25.70	22.35	13.31
105	J133223.27+503432.5	203.0969390	50.5756828	0.190	0.227	0.25	0.22	1.26	2.14	18.09	<16.89	11.52	12.43	<12.39
106	J133529.45+410126.0	203.8727200	41.0238890	0.275	0.346	0.21	0.16	0.70	2.95	15.75	<16.89	10.39	<10.99	<12.39
107	J140146.53+024434.7	210.4438700	2.7429654	0.166	0.211	0.12	0.13	1.77	2.05	<10.89	<16.89	17.07	15.15	<12.39

Note.
[a] Upper limits are 3σ.

Table 4
Fluxes of 24 μm-selected *Herschel*-non-detected Type-1 AGN Sample

#	Source LIRAS	R.A. (J2000)	Decl. (J2000)	z	J (mJy)	K (mJy)	3.4 μm (mJy)	4.6 μm (mJy)	12 μm (mJy)	24 μm (mJy)
1	J145617.60+222124.9	224.0733159	22.3569112	0.111	0.371	0.446	0.26	0.24	0.59	1.00
2	J212932.89+001045.4	322.3870342	0.1792855	0.132	0.460	0.820	0.63	0.68	1.09	2.42
3	J145735.11+223202.4	224.3963065	22.5339901	0.149	0.083	0.096	0.10	0.45	4.62	19.87
4	J020218.53–020243.4	30.5772248	–2.0453957	0.249	0.068	0.111	0.17	0.25	0.39	1.58
5	J140127.69+025606.2	210.3653800	2.9350470	0.265	0.175	0.313	0.79	1.30	3.30	4.68
6	J145720.55+223239.1	224.3356237	22.5442076	0.289	0.055	0.094	0.10	0.13	0.55	1.21
7	J024851.43–032249.3	42.2143100	–3.3803662	0.300	0.144	0.349	0.60	0.87	1.26	2.19
8	J140019.72+030346.1	210.0821561	3.0628171	0.319	0.245	0.431	0.40	0.42	0.72	1.72
9	J145619.67+221125.6	224.0819426	22.1904548	0.326	0.142	0.292	0.38	0.61	1.91	5.43
10	J140117.52+024350.3	210.3230104	2.7306321	0.363	0.125	0.232	0.24	0.27	0.44	1.12
11	J013056.38–132849.9	22.7349275	–13.4805182	0.363	0.176	0.287	0.33	0.43	1.75	6.22
12	J133236.80+503032.8	203.1533400	50.5091160	0.375	0.173	0.267	0.50	0.75	1.84	2.95
13	J163935.63+464933.4	249.8984570	46.8259344	0.393	0.200	0.308	0.51	0.71	1.30	3.31
14	J020138.92–022250.8	30.4121497	–2.3807741	0.395	0.059	0.115	0.14	0.18	0.80	2.12
15	J101616.78+391143.4	154.0699155	39.1953753	0.413	0.241	0.304	0.56	0.92	1.96	2.71
16	J131118.20–011429.0	197.8258434	–1.2416552	0.414	0.128	0.241	0.26	0.33	1.12	3.20
17	J024843.83–033650.5	42.1826278	–3.6140230	0.431	0.101	0.208	0.27	0.31	0.94	2.69
18	J145640.37+223347.5	224.1682008	22.5632037	0.433	0.112	0.252	0.32	0.35	0.98	2.54
19	J005509.17+262714.6	13.7882027	26.4540544	0.434	0.353	1.216	2.09	3.38	7.89	18.01
20	J024858.52–033639.0	42.2438462	–3.6108370	0.459	0.089	0.165	0.19	0.25	0.75	1.64
21	J101537.90+390154.2	153.9079349	39.0317329	0.510	0.132	0.299	0.51	0.77	1.50	4.00
22	J164025.01+464449.2	250.1042205	46.7470097	0.537	0.268	0.412	0.62	0.87	1.74	4.12
23	J164101.85+464813.3	250.2577029	46.8037024	0.538	0.041	0.062	0.08	0.14	0.30	1.38
24	J212939.40–000719.7	322.4141840	–0.1221444	0.553	0.261	0.506	1.12	1.73	3.35	1.60
25	J101744.06+391855.5	154.4335759	39.3154068	0.563	0.133	0.254	0.24	0.23	0.33	1.05
26	J015254.03+010435.1	28.2251178	1.0764123	0.569	0.106	0.214	0.29	0.29	0.43	1.67
27	J014157.79+213236.9	25.4908113	21.5435784	0.602	0.109	0.227	0.40	0.52	1.06	2.58
28	J084249.95+361024.0	130.7081329	36.1736077	0.610	0.056	0.109	0.16	0.14	0.33	1.03
29	J073201.47+314713.8	113.0061071	31.7871707	0.615	0.130	0.236	0.37	0.60	1.67	4.07
30	J101720.68+385738.2	154.3361648	38.9606249	0.629	0.151	0.248	0.48	0.73	1.23	2.21
31	J015258.67+010507.7	28.2444613	1.0854714	0.647	0.080	0.138	0.21	0.32	0.89	1.66
32	J212750.81–120725.3	321.9617189	–12.1236953	0.671	0.137	0.252	0.44	0.76	1.40	3.13
33	J212701.55–121455.5	321.7564446	–12.2487586	0.689	0.047	0.090	0.18	0.24	0.52	1.49
34	J142622.67+373945.4	216.5944468	37.6625988	0.701	0.046	0.080	0.11	0.12	0.17	1.01
35	J083747.88+144923.5	129.4494882	14.8231862	0.703	0.070	0.152	0.20	0.22	0.55	1.17
36	J090021.93+210803.9	135.0913743	21.1344119	0.704	0.114	0.191	0.37	0.55	1.11	2.52
37	J083649.34+150041.1	129.2055920	15.0114258	0.777	0.045	0.062	0.00	0.00	0.00	1.01
38	J171918.13+262540.2	259.8255299	26.4278381	0.797	0.126	0.141	0.22	0.28	1.14	1.85
39	J020048.36–021751.2	30.2015108	–2.2975661	0.812	0.176	0.223	0.47	0.72	1.62	2.28
40	J215359.89+174521.7	328.4995394	17.7560307	0.852	0.112	0.117	0.23	0.34	0.58	1.12
41	J073226.58+314212.9	113.1107413	31.7035956	0.859	0.085	0.122	0.22	0.32	0.67	2.34
42	J101803.66+391247.2	154.5152358	39.2131156	0.878	0.250	0.154	0.27	0.37	1.07	3.29
43	J014112.30+213018.7	25.3012390	21.5051822	0.920	0.046	0.070	0.15	0.18	0.67	1.54
44	J084327.98+361859.8	130.8665855	36.3166119	0.933	0.090	0.135	0.18	0.28	0.57	1.46
45	J224803.10–160411.1	342.0129169	–16.0697373	0.944	0.077	0.081	0.00	0.00	0.00	1.08
46	J083805.87+145152.3	129.5244700	14.8645240	0.980	0.097	0.264	0.12	0.24	0.56	9.08
47	J131055.59–012724.4	197.7316410	–1.4567915	0.999	0.224	0.251	0.51	0.62	0.94	1.48
48	J090121.71+204357.9	135.3404435	20.7327509	1.024	0.031	0.068	0.13	0.19	0.49	1.51
49	J101615.06+385027.8	154.0627539	38.8410657	1.048	0.080	0.183	0.41	0.78	2.35	4.93
50	J164134.75+463727.4	250.3948001	46.6242745	1.049	0.057	0.097	0.13	0.21	0.55	1.35
51	J083701.75+150903.2	129.2572855	15.1508762	1.051	0.038	0.057	0.10	0.12	0.49	1.99
52	J084245.96+360912.6	130.6914837	36.1535129	1.085	0.057	0.096	0.00	0.00	0.00	1.79
53	J212802.02–120252.4	322.0084361	–12.0478995	1.087	0.061	0.098	0.14	0.20	0.54	1.09
54	J133600.73+411317.8	204.0030568	41.2216018	1.125	0.016	0.027	0.06	0.11	0.35	1.07
55	J083222.28+660030.1	128.0928442	66.0083497	1.142	0.049	0.083	0.16	0.35	0.68	2.10
56	J213011.27–000432.7	322.5469763	–0.0757426	1.143	0.029	0.060	0.10	0.15	0.48	1.02
57	J015309.13+005250.2	28.2880289	0.8805977	1.159	0.073	0.115	0.23	0.43	0.89	1.49
58	J212910.65+000342.3	322.2943671	0.0617379	1.160	0.025	0.064	0.14	0.23	0.42	1.11
59	J212912.42+000236.2	322.3017563	0.0433792	1.161	0.065	0.110	0.17	0.23	0.90	1.28
60	J083226.37+654840.8	128.1098895	65.8113464	1.184	0.048	0.079	0.14	0.24	0.66	1.84
61	J080208.92+360417.7	120.5371871	36.0715826	1.202	0.296	0.333	0.49	1.01	2.31	3.40
62	J020235.38–020254.8	30.6474322	–2.0485566	1.210	0.056	0.064	0.11	0.16	0.29	1.24
63	J010653.57+004830.3	16.7232181	0.8084284	1.219	0.032	0.058	0.09	0.19	0.69	1.38

Table 4
(Continued)

#	Source LIRAS	R.A. (J2000)	Decl. (J2000)	z	J (mJy)	K (mJy)	3.4 μm (mJy)	4.6 μm (mJy)	12 μm (mJy)	24 μm (mJy)
64	J020142.58–021610.0	30.4274345	–2.2697118	1.249	0.087	0.117	0.19	0.33	0.97	2.41
65	J003734.02+091608.2	9.3917471	9.2689511	1.252	0.171	0.274	0.40	0.82	0.00	2.34
66	J133103.57+503052.1	202.7648601	50.5144585	1.302	0.078	0.098	0.21	0.42	0.97	2.08
67	J082941.60+660253.7	127.4233310	66.0482369	1.332	0.052	0.070	0.13	0.28	0.88	1.72
68	J212909.66+001214.6	322.2902318	0.2040466	1.339	0.088	0.119	0.20	0.37	1.08	2.40
69	J164038.15+465357.5	250.1589394	46.8993057	1.391	0.042	0.068	0.14	0.30	0.88	1.88
70	J212904.54–000508.0	322.2689354	–0.0855606	1.420	0.047	0.066	0.09	0.19	0.54	1.73
71	J101553.27+384725.8	153.9719421	38.7904969	1.458	0.121	0.114	0.21	0.57	1.55	2.62
72	J133114.04+503859.8	202.8084850	50.6499324	1.487	0.090	0.088	0.12	0.25	0.61	1.36
73	J084308.19+362439.8	130.7841107	36.4110470	1.500	0.044	0.049	0.06	0.16	0.31	1.05
74	J084309.91+292919.8	130.7912860	29.4888350	1.509	0.094	0.104	0.15	0.27	1.09	1.62
75	J084226.71+292943.6	130.6113009	29.4954535	1.541	0.084	0.107	0.11	0.16	0.54	1.02
76	J024831.84–032420.5	42.1326874	–3.4057045	1.550	0.089	0.107	0.16	0.30	1.31	3.06
77	J164104.44+463852.8	250.2684968	46.6480030	1.572	0.179	0.166	0.22	0.47	1.32	2.02
78	J003721.71+090940.8	9.3404766	9.1613400	1.595	0.036	0.046	0.08	0.15	0.00	1.14
79	J101653.69+385501.9	154.2237164	38.9172001	1.600	0.054	0.051	0.10	0.19	0.49	1.67
80	J083027.88+655926.4	127.6161497	65.9906731	1.614	0.024	0.032	0.08	0.13	0.47	1.03
81	J010603.85+010506.4	16.5160297	1.0851213	1.617	0.102	0.104	0.15	0.25	0.64	1.18
82	J133222.65+504930.6	203.0943922	50.8251692	1.719	0.066	0.058	0.10	0.18	0.47	1.51
83	J213014.92+000320.9	322.5621719	0.0557977	1.775	0.043	0.055	0.07	0.10	0.32	1.08
84	J133444.91+410929.2	203.6871235	41.1581027	1.776	0.038	0.056	0.06	0.14	0.42	1.45
85	J083629.77+144719.4	129.1240572	14.7887154	1.812	0.049	0.070	0.07	0.14	0.91	1.95
86	J084218.60+362619.9	130.5775168	36.4388689	1.831	0.106	0.103	0.15	0.24	0.99	1.56
87	J010616.39+005656.9	16.5682822	0.9491375	1.868	0.043	0.053	0.08	0.14	0.49	1.05
88	J145710.80+221844.3	224.2950047	22.3123025	1.874	0.147	0.164	0.17	0.25	0.73	1.79
89	J131137.33–013008.6	197.9055371	–1.5023761	1.901	0.070	0.081	0.14	0.17	0.82	1.82
90	J133308.73+503359.4	203.2863608	50.5664955	1.938	0.033	0.056	0.11	0.15	0.47	1.52
91	J082604.12+042535.9	126.5171495	4.4266369	1.981	0.140	0.133	0.15	0.29	0.80	2.83
92	J080151.80+360854.7	120.4658345	36.1485281	2.089	0.026	0.040	0.06	0.09	0.60	1.15
93	J131216.87–013142.7	198.0703031	–1.5285371	2.159	0.030	0.049	0.06	0.12	0.75	2.86
94	J212655.37–120639.9	321.7307101	–12.1110704	2.352	0.066	0.144	0.00	0.00	0.00	1.19
95	J224853.33–161926.6	342.2221902	–16.3240569	2.380	0.122	0.194	0.13	0.17	0.61	1.59
96	J083659.87+151155.7	129.2494400	15.1988120	2.609	0.019	0.044	0.77	1.37	4.23	1.33
97	J215356.08+174830.2	328.4836797	17.8083773	3.344	0.017	0.017	0.00	0.00	0.00	2.58
98	J073240.61+315121.6	113.1692239	31.8559987	5.075	0.022	0.016	0.00	0.00	0.00	1.14

missed 5.4% of the targets). Among the 1729 sources targeted by Hectospec, 1263 yielded spectroscopic redshifts with a corresponding success rate of 73%.

To identify Type-1 AGNs, we fitted each emission line in the optical spectra with single or double Gaussian profiles. We list the FWHM of typical broad emission lines in Table 5. Sources showing emission lines (specifically, Mg II, C IV, Hβ, or Hα) with FWHM over 1200 km s^{-1} were selected as Type-1 AGNs (Hao et al. 2005). Finally 205 sources satisfied our Type-1 AGN selection criteria, 177 confirmed with Hectospec and 28 confirmed with SDSS.[8] More details of the sample selection can be found in Appendix B. Figure 1 shows the 24 μm flux distribution and spectroscopic status of the members of our sample. Figure 2 shows the redshift distribution of the AGNs; virtually all of them are far behind the clusters. They are also far from the cluster centers (typically by 1′ or more), so they are not significantly magnified. We exclude any AGNs in the clusters according to the source redshift.

[8] The spectra were inspected visually to confirm the classification. One ambiguous case (#6 J084352.28+292854.0) was retained because its SED decomposition fit (see Section 3.4) supported the classification. J084234.94+362503.2 (#13) falls slightly below our line width criterion but was retained because spectropolarimetry shows it to have a hidden Type-1 nucleus (Zakamska et al. 2005).

3.1.2. Results

Of the 205 24 μm-selected Type-1 AGNs we identified, 107 are securely detected by *Herschel*, 101 in at least two bands. For these sources, Table 3 presents coordinates, redshifts, and observed flux densities in the NIR (J and K bands from UKIRT and NEWFIRM), MIR (3.4, 4.6, and 12 μm from *WISE*; 24 μm from *Spitzer*), and FIR (100, 160, 250, 350, and 500 μm from *Herschel*). Similar information is provided in Table 4 for the sources not detected with *Herschel*. Below we discuss the basic properties of the *Herschel*-detected sources and compare them with those not detected by *Herschel* through a stacking analysis of the latter. In Section 3.5, we show that the SDSS colors of the *Herschel*-detected and *Herschel*-non-detected sample members do not differ significantly, showing that the dust emitting in the FIR is not producing significant extinction along the line of sight toward the AGNs. This result is consistent with the hypothesis that this dust is not associated with the active nuclei and simplifies the comparison of the *Herschel*-detected and non-detected sources.

3.1.3. Completeness

We ran simple simulations to test the completeness of the Type-1 AGN identification. The two plots in the upper panel of

Table 5
Redshifts, Luminosities, Broad Emission Line Widths, Black Hole Masses, and Stellar Masses for the *Herschel*-detected Type-1 Sources

#	Source LIRAS	z	$L_{0.5-8\ \mathrm{keV}}$ ($10^{10}L_{\odot}$)	L_B ($10^{11}L_{\odot}$)	$L_{\mathrm{tot,IR}}$ ($10^{11}L_{\odot}$)	$L_{\mathrm{SF,IR}}$[a] ($10^{11}L_{\odot}$)	$L_{\mathrm{AGN,IR}}$ ($10^{11}L_{\odot}$)	L_{warm}[b] ($10^{11}L_{\odot}$)	Line	FWHM (km s^{-1})	$M_{\bullet}$[c] ($10^{8}M_{\odot}$)	M_{*} ($10^{11}M_{\odot}$)
1	J024818.61−031956.9	0.127	⋯	0.71	0.41	0.22(0.00)	0.19	(0.00)	Hβ	2521	0.29	0.95[d]
2	J020120.00−022447.7	0.136	⋯	1.02	0.90	0.40(−0.10)	0.50	(0.20)	Hβ	2594	0.51	0.85[d]
3	J212928.91+000415.9	0.180	0.05	0.01	0.71	0.61(−0.55)	0.11	(0.09)	Hα	>1200	N/A	0.82[d]
4	J073243.17+314111.4	0.276	0.49	1.36	0.78	0.43(0.00)	0.36	(0.00)	Hβ	3313	0.69	0.87[d]
5	J082626.42+041231.0	0.324	0.30	0.00	0.82	0.62(−0.16)	0.20	(0.07)	Hβ	3017	0.43	0.81[d]
6	J084352.28+292854.0	0.336	⋯	1.50	0.68	0.44(−0.06)	0.24	(0.07)	Hβ	11620	6.99	1.92[d]
7	J014200.86+213752.6	0.381	⋯	1.28	1.29	1.07(−0.04)	0.23	(0.12)	Hβ	2225	0.25	0.65[d]
8	J212930.74+001347.2	0.395	⋯	2.48	7.34	1.92(−1.00)	5.41	(6.26)	Hβ	2326	1.34	0.94
9	J003730.63+092255.6	0.397	⋯	6.45	2.10	1.42(0.00)	0.68	(0.00)	Hβ	4405	1.69	1.32[d]
10	J212911.74−000438.2	0.425	⋯	16.74	1.90	1.45(−0.13)	0.45	(0.75)	Hβ	9412	6.35	1.76[d]
11	J024838.05−031730.8	0.428	⋯	0.30	2.42	1.76(0.00)	0.66	(0.00)	Hβ	4127	1.46	1.55[d]
12	J212629.76−120555.5	0.444	⋯	0.44	3.26	2.35(0.00)	0.91	(0.03)	Hβ	4238	1.81	1.27
13	J084234.94+362503.2	0.561	⋯	0.01	3.76	2.82(−0.04)	0.94	(4.13)	Mg II	1037	0.11	3.97[d]
14	J080126.90+360059.1	0.579	⋯	0.00	2.21	1.86(−0.07)	0.35	(0.43)	Mg II	2072	0.26	1.89[d]
15	J215343.83+172912.9	0.595	⋯	0.29	18.12	16.32(−0.09)	1.80	(4.64)	Mg II	3476	1.67	1.64[d]
16	J083107.34+654653.9	0.638	8.65	3.08	16.80	7.38(0.00)	9.42	(0.00)	Hβ	5562	10.03	7.02
17	J080013.86+355831.3	0.678	⋯	1.38	9.63	5.74(−0.64)	3.90	(10.31)	Mg II	3410	2.36	2.57[d]
18	J164110.54+464911.8	0.694	⋯	3.53	5.22	2.16(0.00)	3.06	(0.00)	Mg II	3998	2.87	2.01
19	J090026.52+204158.8	0.705	⋯	0.00	51.16	0.00	11.59	39.57	Mg II	3140	3.45	2.42
20	J083118.85+660117.8	0.708	⋯	0.00	6.57	5.40(−0.16)	1.18	(2.69)	Mg II	4140	1.91	2.14[d]
21	J084256.20+361325.3	0.722	⋯	0.33	6.90	3.88(−0.88)	3.02	(11.02)	Mg II	2110	0.80	2.23[d]
22	J163934.02+464314.2	0.728	⋯	0.50	6.59	4.96(−0.18)	1.63	(2.49)	Mg II	7099	6.62	2.60[d]
23	J073155.69+312529.2	0.737	⋯	1.01	4.85	3.73(−0.28)	1.12	(2.33)	Mg II	2044	0.46	1.64[d]
24	J080108.38+355222.4	0.756	⋯	1.95	5.73	2.41(−1.00)	3.33	(8.10)	Mg II	2579	1.25	0.87
25	J083747.73+145041.6	0.765	⋯	4.40	8.78	5.61(−0.05)	3.17	(1.43)	Mg II	3493	2.25	1.57
26	J101708.92+385557.6	0.770	⋯	3.88	4.85	2.16(−0.27)	2.69	(1.61)	Mg II	3214	1.74	1.22
27	J014245.21+213449.8	0.812	⋯	5.65	20.40	7.53(0.00)	12.87	(0.00)	Mg II	2151	1.72	1.21
28	J082949.41+653919.8	0.834	⋯	0.00	11.66	9.72(−0.32)	1.94	(5.98)	Mg II	2112	0.64	1.19[d]
29	J015215.36+010514.9	0.834	⋯	0.00	7.12	4.52(0.00)	2.60	(0.00)	Mg II	2618	1.15	0.80
30	J101755.30+390430.8	0.840	⋯	0.00	16.16	6.39(0.00)	9.77	(0.00)	Mg II	3280	3.46	2.42
31	J131206.62−013129.0	0.845	⋯	0.04	19.49	16.19(−0.06)	3.30	(2.57)	Mg II	4435	3.68	2.31[d]
32	J212720.66−120612.9	0.895	⋯	0.16	8.44	6.52(−0.26)	1.93	(3.54)	Mg II	3304	1.56	1.24[d]
33	J133529.41+405828.0	0.900	0.89	0.00	24.53	16.41	0.62	7.50	Mg II	2360	0.51	2.45[d]
34	J131107.34−012857.9	0.916	⋯	0.14	12.04	5.35(0.00)	6.69	(0.00)	Mg II	4024	4.30	3.01
35	J133434.70+410623.4	0.924	⋯	0.00	15.25	7.43(−0.05)	7.82	(1.80)	Mg II	3660	3.88	2.71
36	J145639.07+222516.6	0.952	⋯	3.02	13.67	8.82(−0.10)	4.85	(3.35)	Mg II	4740	5.12	2.97[d]
37	J083008.79+654521.5	0.962	⋯	2.51	14.06	7.93(−0.05)	6.13	(1.52)	Mg II	3759	3.60	2.52
38	J145816.29+222625.1	0.979	⋯	0.01	17.40	5.12(0.00)	12.29	(0.00)	Mg II	3530	4.49	6.32[d]
39	J083806.01+150827.3	1.006	⋯	7.22	12.75	9.37(0.00)	3.38	(0.00)	Mg II	2163	0.89	0.62
40	J140130.51+030358.0	1.013	⋯	1.54	5.04	3.52(−0.33)	1.52	(7.60)	Mg II	6255	4.95	4.00[d]
41	J101730.81+384941.5	1.013	⋯	0.00	15.82	12.74(−0.19)	3.08	(2.65)	Mg II	3154	1.79	1.26
42	J131109.29−011953.9	1.026	⋯	0.00	25.01	15.99	0.81	8.21	Mg II	2289	0.49	1.07[d]
43	J133549.20+411306.1	1.028	⋯	0.22	12.44	9.49(−0.38)	2.95	(8.84)	Mg II	3551	2.23	1.56
44	J212738.37−120050.6	1.064	⋯	0.00	9.74	6.84(−0.42)	2.90	(6.20)	Mg II	1580	0.44	0.31
45	J131109.74−011329.8	1.070	⋯	0.00	13.42	9.98(−0.24)	3.44	(6.41)	Mg II	5308	5.37	1.85[d]

Table 5
(Continued)

#	Source LIRAS	z	$L_{0.5-8\ \mathrm{keV}}$ ($10^{10}L_\odot$)	L_B ($10^{11}L_\odot$)	$L_{\mathrm{tot,IR}}$ ($10^{11}L_\odot$)	$L_{\mathrm{SF,IR}}$[a] ($10^{11}L_\odot$)	$L_{\mathrm{AGN,IR}}$ ($10^{11}L_\odot$)	L_{warm}[b] ($10^{11}L_\odot$)	Line	FWHM (km s^{-1})	$M_\bullet$[c] ($10^8M_\odot$)	M_* ($10^{11}M_\odot$)
46	J073247.15+313429.5	1.082	2.60	1.60	17.72	11.47(−0.55)	6.25	(21.40)	Mg II	2306	1.37	0.96
47	J164020.70+465142.6	1.120	⋯	1.02	12.50	6.32(0.00)	6.17	(0.00)	Mg II	4557	5.30	3.71
48	J164116.66+463946.3	1.129	⋯	1.56	23.68	3.56(0.00)	20.12	(0.00)	Mg II	5055	11.78	8.25
49	J084319.21+361606.9	1.131	⋯	4.52	15.98	6.45(−0.36)	9.54	(4.26)	Mg II	3367	3.63	2.54
50	J224837.78−160109.3	1.132	3.20	2.03	17.60	9.19(−0.07)	8.41	(2.62)	Mg II	4268	5.43	3.80
51	J020239.22−020600.2	1.139	⋯	0.92	22.65	10.97(−0.01)	11.68	(0.37)	Mg II	5584	10.98	7.68
52	J015248.43+011442.0	1.172	⋯	1.29	25.17	12.89(0.00)	12.28	(0.00)	Mg II	5791	12.08	8.46
53	J133314.82+504526.8	1.173	⋯	0.01	20.45	11.50(0.00)	8.95	(0.00)	Mg II	2859	2.51	1.76
54	J224822.19−160711.3	1.178	1.13	0.63	11.48	7.13(−0.11)	4.35	(5.64)	Mg II	2235	N/A	N/A
55	J224820.85−155924.5	1.201	5.94	0.97	10.69	5.63(−0.07)	5.06	(3.66)	Mg II	6157	8.77	6.14
56	J133240.79+502434.8	1.227	⋯	0.01	32.72	20.57(−0.01)	12.15	(0.19)	Mg II	6174	13.66	9.56
57	J133614.87+411012.4	1.259	⋯	0.05	28.61	21.97(−0.09)	6.63	(11.82)	Mg II	5019	6.71	4.70
58	J014126.62+212425.3	1.299	⋯	0.39	14.83	7.86(0.00)	6.97	(0.00)	Mg II	5083	7.01	4.91
59	J212747.81−115844.5	1.325	⋯	0.43	23.21	6.89(0.00)	16.32	(0.00)	Mg II	4998	10.38	7.26
60	J010614.38+011409.6	1.351	⋯	3.94	54.00	42.36(−0.07)	11.64	(7.77)	Mg II	3284	3.78	2.65
61	J014103.82+213228.7	1.367	⋯	1.40	16.33	5.15(0.00)	11.17	(0.00)	Mg II	3291	3.72	2.61
62	J010702.23+005542.0	1.367	⋯	0.00	16.70	12.39(−0.16)	4.31	(7.22)	Mg II	5005	5.35	2.10[d]
63	J073209.94+314143.0	1.382	⋯	1.37	18.30	10.00(−0.25)	8.31	(5.14)	Mg II	4438	5.88	4.11
64	J015243.29+011219.7	1.407	⋯	0.01	28.56	8.30(−0.52)	20.26	(10.34)	Mg II	5294	12.98	9.09
65	J172026.50+263815.0	1.414	⋯	0.01	31.79	16.76(0.00)	15.02	(0.00)	Mg II	2997	3.58	2.51
66	J133313.92+503107.8	1.425	⋯	0.05	25.54	19.79(−0.40)	5.75	(27.96)	Mg II	2588	1.66	3.52[d]
67	J003622.20+091828.1	1.452	⋯	1.21	21.26	11.78(−0.05)	9.48	(3.17)	Mg II	4209	5.62	3.94
68	J003749.95+090711.0	1.522	⋯	0.89	18.94	12.53(−0.34)	6.40	(15.47)	Mg II	4007	4.18	2.93
69	J215347.97+173756.5	1.524	⋯	1.67	22.74	10.55(−0.12)	12.20	(4.97)	Mg II	3039	3.32	2.32
70	J020144.55−022054.4	1.562		1.56	32.06	15.31(0.00)	16.76	(0.00)	Mg II	7589	24.27	16.99
71	J145725.17+223133.8	1.578	⋯	0.01	52.93	6.15(0.00)	46.78	(0.00)	Mg II	3561	8.92	6.24
72	J133543.12+405707.8	1.579	⋯	0.16	68.89	35.91	3.23	29.75	Mg II	2009	N/A	2.19[d]
73	J133531.44+411617.7	1.606	⋯	0.25	47.54	43.55(−0.16)	3.99	(30.51)	Mg II	4629	N/A	3.92[d]
74	J015335.62+010353.7	1.622	⋯	0.76	51.83	39.77(0.00)	12.06	(0.00)	C IV	13560	67.24	47.07
75	J003755.90+090031.3	1.626	⋯	2.18	105.48	66.30(−0.01)	39.19	(2.95)	Mg II	4211	11.42	8.00
76	J131129.64−011603.2	1.655	18.81	0.16	36.42	24.35(0.00)	12.08	(0.00)	Mg II	4298	6.60	4.62
77	J212849.04+000447.6	1.685	⋯	0.01	51.39	9.95(0.00)	41.43	(0.00)	Mg II	4505	13.44	9.41
78	J212947.12+002026.3	1.722	⋯	0.63	70.93	39.49(0.00)	31.44	(0.00)	Mg II	7293	30.66	21.46
79	J013253.29−133915.7	1.730	⋯	1.19	35.02	27.17(−0.16)	7.85	(20.50)	Mg II	17310	N/A	N/A
80	J084304.84+292953.8	1.737	34.64	9.73	64.20	8.19(0.00)	56.01	(0.00)	Mg II	5018	19.38	13.56
81	J133354.56+410300.1	1.758	⋯	0.08	21.81	13.61(−0.19)	8.20	(11.17)	Mg II	2287	1.54	1.08
82	J133526.73+405957.6	1.763	12.89	0.40	52.99	18.69(−0.16)	34.30	(8.29)	Mg II	4206	10.65	7.46
83	J213006.22+001256.8	1.801	⋯	8.24	35.48	22.91(0.00)	12.57	(0.00)	Mg II	2715	2.70	N/A
84	J163922.35+463428.6	1.809	⋯	0.37	49.80	18.82	6.13	24.86	Mg II	1382	N/A	N/A
85	J084327.91+361723.4	1.883	⋯	1.34	117.11	40.55	10.86	65.70	Mg II	2429	N/A	N/A
86	J142539.38+375736.8	1.905	⋯	0.01	128.10	39.86(−1.00)	88.24	(211.42)	Mg II	4059	15.98	N/A
87	J212939.66+000815.5	2.005	5.78	2.23	96.29	9.74	15.80	70.75	C IV	6170	16.09	N/A
88	J073124.82+314721.2	2.065	⋯	0.00	53.85	44.30(−0.23)	9.55	(38.86)	C IV	1740	N/A	N/A
89	J163950.35+463327.1	2.090	⋯	1.23	44.08	14.82(0.00)	29.26	(0.00)	C IV	1142	N/A	N/A

Table 5
(Continued)

#	Source LIRAS	z	$L_{0.5-8\ \mathrm{keV}}$ ($10^{10}L_{\odot}$)	L_B ($10^{11}L_{\odot}$)	$L_{\mathrm{tot,IR}}$ ($10^{11}L_{\odot}$)	$L_{\mathrm{SF,IR}}$[a] ($10^{11}L_{\odot}$)	$L_{\mathrm{AGN,IR}}$ ($10^{11}L_{\odot}$)	L_{warm}[b] ($10^{11}L_{\odot}$)	Line	FWHM (km s^{-1})	$M_{\bullet}$[c] ($10^{8}M_{\odot}$)	M_{*} ($10^{11}M_{\odot}$)
90	J090122.68+204446.7	2.094	⋯	0.00	307.14	89.77(0.00)	217.37	(0.00)	C IV	6990	82.94	N/A
91	J020225.55−020258.0	2.133	⋯	0.79	49.53	24.69(−0.61)	24.83	(57.48)	C IV	5179	N/A	N/A
92	J020101.83−021140.5	2.162	⋯	0.42	89.52	25.80(−0.27)	63.72	(27.15)	C IV	>1200	N/A	N/A
93	J003615.85+091328.2	2.203	⋯	5.21	71.72	28.88(−0.05)	42.84	(6.11)	C IV	>1200	N/A	N/A
94	J084254.20+293748.8	2.230	⋯	0.00	57.69	45.97(−0.18)	11.72	(33.27)	C IV	4756	8.15	N/A
95	J084306.40+293922.2	2.230	⋯	1.37	118.54	63.14(−0.61)	55.40	(25.89)	C IV	5340	23.40	N/A
96	J003706.97+091222.0	2.265	⋯	0.00	53.69	24.62(0.00)	29.06	(0.00)	C IV	2921	5.01	N/A
97	J212709.43−120155.1	2.315	⋯	0.32	139.21	66.65	10.64	61.92	C IV	2524	2.39	N/A
98	J083758.17+145856.6	2.346	⋯	0.00	69.44	37.75(−0.04)	31.70	(5.43)	C IV	>1200	N/A	N/A
99	J224924.31−161159.9	2.385	⋯	0.00	56.39	33.39(−0.64)	23.00	(74.58)	C IV	>1200	N/A	N/A
100	J024725.09−033807.9	2.420	⋯	0.64	117.35	45.75(0.00)	71.59	(0.00)	C IV	2687	6.79	N/A
101	J085941.47+204815.5	2.474	⋯	8.85	88.44	45.20(0.00)	43.24	(0.00)	C IV	6138	27.11	N/A
102	J083712.89+145917.4	2.506	⋯	1.07	228.56	24.88(−1.00)	203.68	(58.94)	C IV	5423	48.11	N/A
103	J131119.24−012030.9	2.591	17.43	0.04	147.75	0.86(−1.00)	146.89	(62.36)	C IV	9483	123.72	N/A
104	J163641.18+660848.3	3.157	48.19	1.75	100.28	55.63(−0.70)	44.66	(126.14)	C IV	1478	N/A	N/A
105	J133223.27+503432.5	3.807	⋯	0.01	228.63	0.00(0.00)	228.63	(27.79)	C IV	5918	60.92	N/A
106	J133529.45+410126.0	4.280	⋯	0.01	322.04	0.00(0.00)	322.04	(98.61)	C IV	5611	N/A	N/A
107	J140146.53+024434.7	4.418	⋯	0.01	315.26	32.81(−1.00)	282.45	(148.39)	C IV	5337	55.41	N/A

Notes.
[a] Numbers in parentheses are the decrease in the fraction of the SF IR luminosities if we add the warm component as a degree of freedom in the SED decomposition precedure. For the case that the warm component is required in order to obtain good SED fits, we do not provide this decrease fraction with parentheses.
[b] Numbers in parentheses are the warm component luminosities if we add the warm component as a degree of freedom in the SED decomposition precedure. For some sources, the warm component is required in order to obtain good SED fits. The warm component luminosities for such sources are provided with no parentheses.
[c] Some AGNs are broad absorption line quasars, and their broad emission line FWHM is above 1200 km s^{-1}, but is not well constrained. Some AGNs have low S/N optical spectra, and the emission line fitting is not good enough to estimate the black hole mass.
[d] Host galaxy stellar masses derived from K-band luminosity; all other masses are estimated from the local $M_{\bullet}/M_{*}$ ratio.

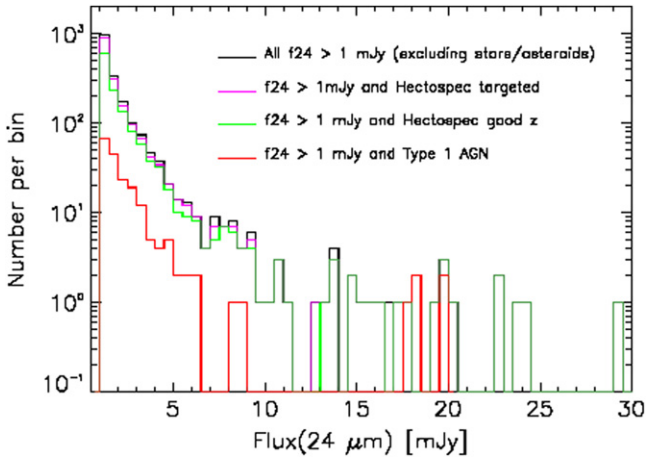

Figure 1. 24 μm flux density distributions of sources in our survey area. The black histogram shows the distribution of all sources with 24 μm flux density >1 mJy excluding stars and asteroids. The magenta curve shows the distribution of sources targeted by Hectospec fibers (1729). The green curve shows the distribution of sources with well determined redshifts from Hectospec spectroscopy (1209). The red histogram is Type-1 AGNs with emission line FWHM > 1200 km s^{-1} (205).

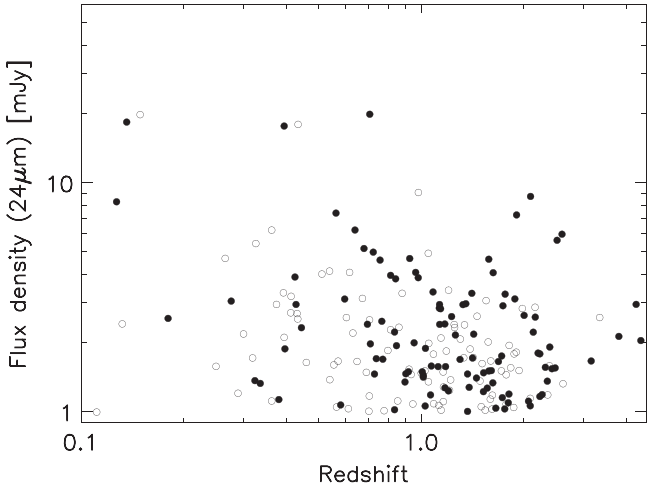

Figure 2. 24 μm flux density vs. redshift for Type-1 AGNs with 24 μm flux density >1 mJy in our survey area. The filled circles show *Herschel*-detected Type-1 AGNs. The unfilled circles show *Herschel*-non-detected Type-1 AGNs.

Figure 3 show the expected apparent K-band and r' band (SDSS) magnitudes as a function of 24 μm flux density for Type-1 AGNs, represented by the template of Elvis et al. (1994). The K and r' band magnitudes are functions of redshift and dust extinction. To simulate these effects, the template of Elvis et al. (1994) was redshifted incrementally over the range $z = 0$ to $z = 3.6$, covering the redshift range over which we identified AGNs. We added extinction using a composite reddening law: (1) the Galactic extinction curve above 1 μm (Rieke & Lebofsky 1985); and (2) a SMC extinction curve below 1 μm (Gordon et al. 2003);[9] the value of A_V ranged from 0 to 1.5. We rescaled the AGN template to make the 24 μm flux density always above 1 mJy. We used the same range of the flux level and A_V to generate the data points in the two plots in the upper panel of Figure 3; in other words, the data points in these two plots are from the same AGN populations. The simulation then lets us compare the incompleteness resulting from our detection limits for K-band and for optical spectroscopy.

Sources fainter than our K-band detection limit of 19 mag (Vega, 5σ) were not targeted in ACReS, but this K-band limit does not affect our AGN survey significantly. As shown in the upper left of Figure 3, all sources with 24 μm flux density above 1 mJy and A_V smaller than 1.5 mag have K-band magnitudes brighter than 19 (Vega), and therefore were targeted. The K-band limit would only exclude a few very red AGNs close to the 24 μm 1 mJy flux density cutoff. The r' band simulation shows that such very red AGNs would drop below the limit for successful optical spectra. As can be seen from the lower left of Figure 3, the K-band distribution of our 205 Type-1 AGNs declines steeply from 17.5 to 19 mag (Vega), probably because the optical spectroscopy sets a tighter constraint for inclusion in our sample than does the K-band cutoff. As expected, reddening affects the r' band more than the K-band (see upper panels of Figure 3). The lower right of Figure 3 compares the distribution of r' magnitude for targets that were put on Hectospec fibers and targets where emission lines were detected (for sources with 24 μm flux density above 1 mJy). The redshift success rate starts declining from $r' = 19.5$ mag (AB), and declines steeply for sources fainter than 20.5 mag (AB). We conclude that our spectroscopic survey is incomplete at the lowest 24 μm flux density levels for red sources with A_V above 0.5 mag.

However, Figure 3 implies that the completeness will increase rapidly as the 24 μm threshold is raised above 1 mJy. In confirmation, Figure 1 shows that the fraction of Type-1 AGNs within the total sample targeted for spectra is roughly constant above 2 mJy, but is somewhat lower in the 1–2 mJy bin. This drop toward 1 mJy is the behavior expected from incompleteness, but a part of the drop is also likely to be intrinsic, as shown by Brand et al. (2006). From Brand et al. (Figure 4, both data and Pearson models), we estimate that the intrinsic fraction at 1–1.5 mJy should be about 70% of the asymptotic value at larger flux densities. We then predict 100 AGNs in the 1–1.5 mJy bin, where only 68 are detected, i.e., we are potentially missing about 30 AGNs. There is no evidence from the counts for any missing AGNs in the 1.5–2 mJy or higher bins. We therefore estimate that the incompleteness in our sample is about 30/235 = 13%, concentrated in the 1–1.5 mJy range and largely due to incompleteness in the optical spectroscopy. Combining with the incompleteness of 5.4% in the spectroscopy itself, the total of missing sources is about 18%.

In addition to the missing Type-1 AGNs, our sample will miss other types of active object. For example, from Dey et al. (2008), nearly half of the objects not targeted for spectroscopy because they did not have optical counterparts (see Appendix B) are likely to be dust-obscured galaxies. Because of their low accretion efficiency and low Eddington ratios, our sample will also not include a significant number of jet-mode AGNs (Yuan & Narayan 2014). Our sample is therefore confined to traditional Type-1 AGNs identified by optical spectroscopy, selected to a uniform level of MIR flux density.

[9] Studies show that the reddening toward quasars is dominated by SMC-like dust at the quasar redshift (e.g., Richards et al. 2003; Hopkins et al. 2004; also see the "Gray" extinction curve in Czerny et al. 2004 and Gaskell et al. 2004).

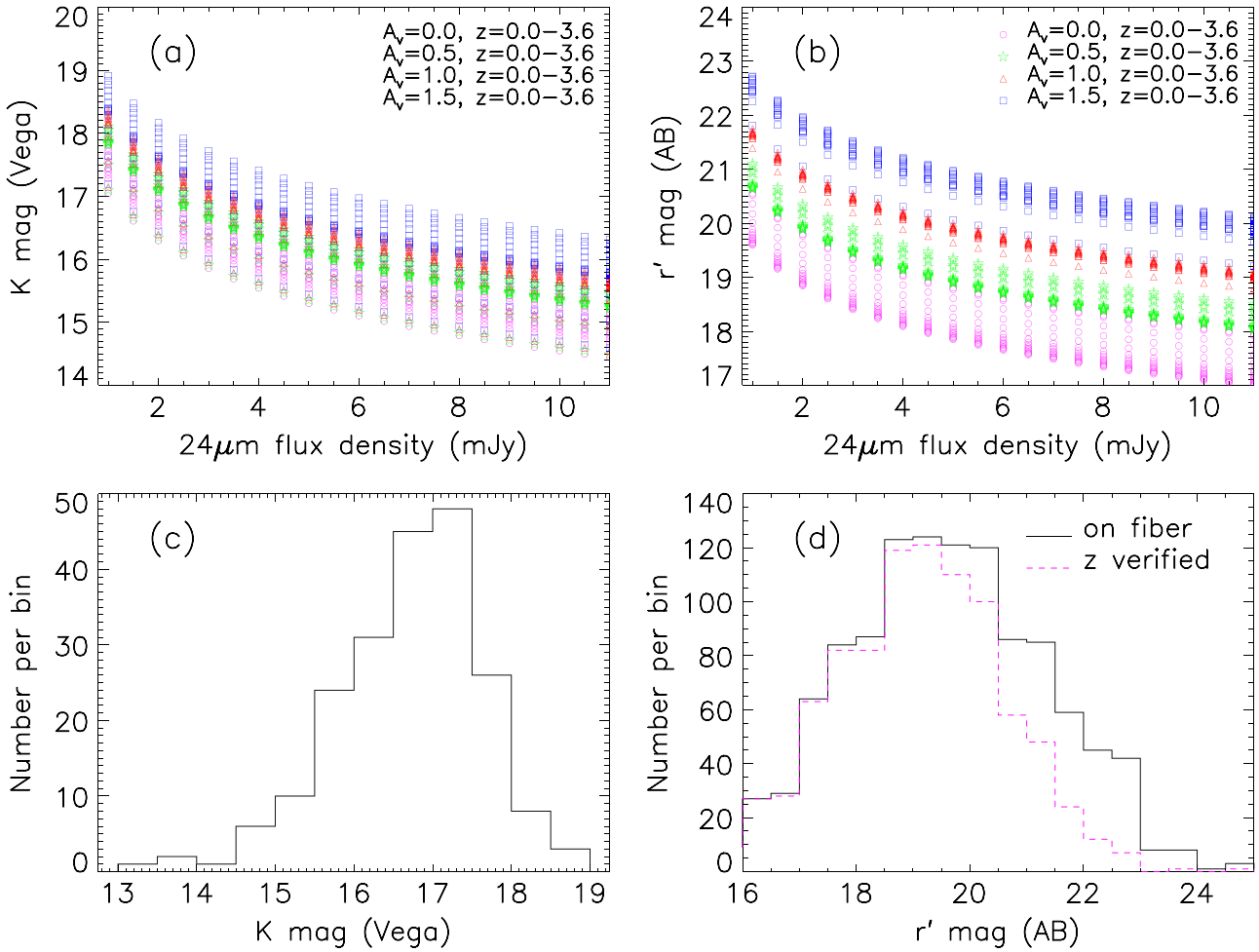

Figure 3. (a) Simulation results showing the expected apparent *K*-band magnitude as a function of 24 μm flux for Type-1 AGNs, as functions of redshift (z = 0–3.6) and dust extinction (A_V = 0–1.5). (b) Same as (a) but for r' band. (c) *K*-band magnitude (Vega) distribution of 205 Type-1 AGNs with 24 μm flux density >1 mJy in our survey area. (d) Distribution of r' band magnitudes for targets that were put on Hectospec fibers and targets that are successfully identified with emission lines.

3.2. Type-1 AGN Properties

3.2.1. Redshift Distribution

Figure 2 shows the redshift distribution of our Type-1 AGN sample.[10] We omit four sources at $z > 3$ (numbers 104–107 in Table 3) from further analysis because of the very small number statistics in our sample at these redshifts. The distributions for the *Herschel*-detected subsample and the *Herschel*-non-detected one are very similar. The two-sample Kolmogorov–Smirnov test (K–S test) is consistent at the 5% level (P-value = 0.053) with the null hypothesis that these two subsamples are drawn from the same distribution; that is, they are statistically indistinguishable. This situation is only possible if the luminosity of the FIR excess (which we will attribute to star formation) grows with the increasing AGN luminosity that results from the flux limit of our AGN selection.

3.2.2. Spectral Energy Distributions

Three typical examples of the SEDs of these AGNs are illustrated in Figure 4. In $\nu f_\nu - \lambda$ units, some of the SEDs look flat from the optical to the FIR, while some show peaks in the UV and optical, or in the FIR, or both. The FIR peak has a Rayleigh–Jeans tail, declining steeply toward the millimeter-wave region. The SEDs of some sources at lower redshift show a peak near 1 μm (rest-frame).

By stacking signals over a large number of source positions, we can study the FIR properties of sources too faint to detect with *Herschel* individually. We stacked the signals for *Herschel*-non-detected Type-1 AGNs in three redshift bins: 0.1–0.7, 0.7–1.2, and 1.2–1.9. There are 24, 24, and 18 sources in these three bins, respectively. All the sources were well detected from the UV to 24 μm. At these wavelengths, we took the average of the measured fluxes in each band for all of the sources in a redshift bin, after eliminating the 3σ outliers. For the five *Herschel* bands, we registered PACS/SPIRE images with the 24 μm image by aligning the bright isolated point sources, and then isolated a small image centered on the source position. We checked the images individually, and rejected those contaminated by close bright objects. For each redshift bin and each *Herschel* band, we then clipped the 3σ outliers for each aligned pixel over the full set of images. Since the *Herschel* maps were roughly uniform in exposure and noise, we could then take the straight average of all the remaining data. Where there was a detection on the stacked image, we did aperture photometry, including applying aperture corrections

[10] From SDSS spectroscopy, there are a number of sources detected by *Herschel* at $z > 2$; however, they are not included in our study because at these redshifts the *Herschel* bands may be significantly influenced by emission from the AGN.

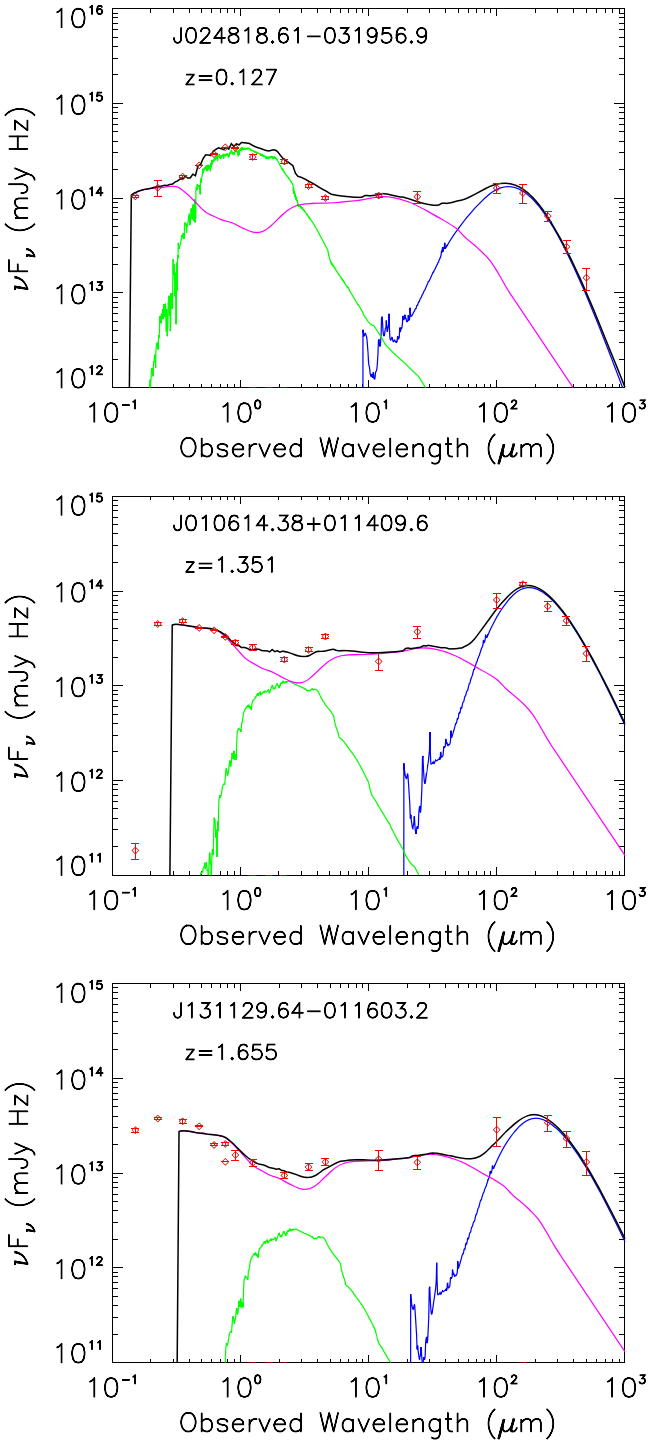

Figure 4. Examples of SEDs and decomposition results. The diamond points are the average fluxes at FUV, NUV, and five SDSS bands (u', g', r', i', z'), J, K, and three *WISE* bands (3.4, 4.6, and 12 μm), 24 μm, and five *Herschel* bands (100, 160, 250, 350, and 500 μm). The solid lines show the SED decomposition results: the magenta line is the rescaled Type-1 AGN template (Elvis et al. 1994); the green line is the stellar photospheric component; the blue line is the best fitted star formation template. The black line is the total of AGN, stellar, and star formation components.

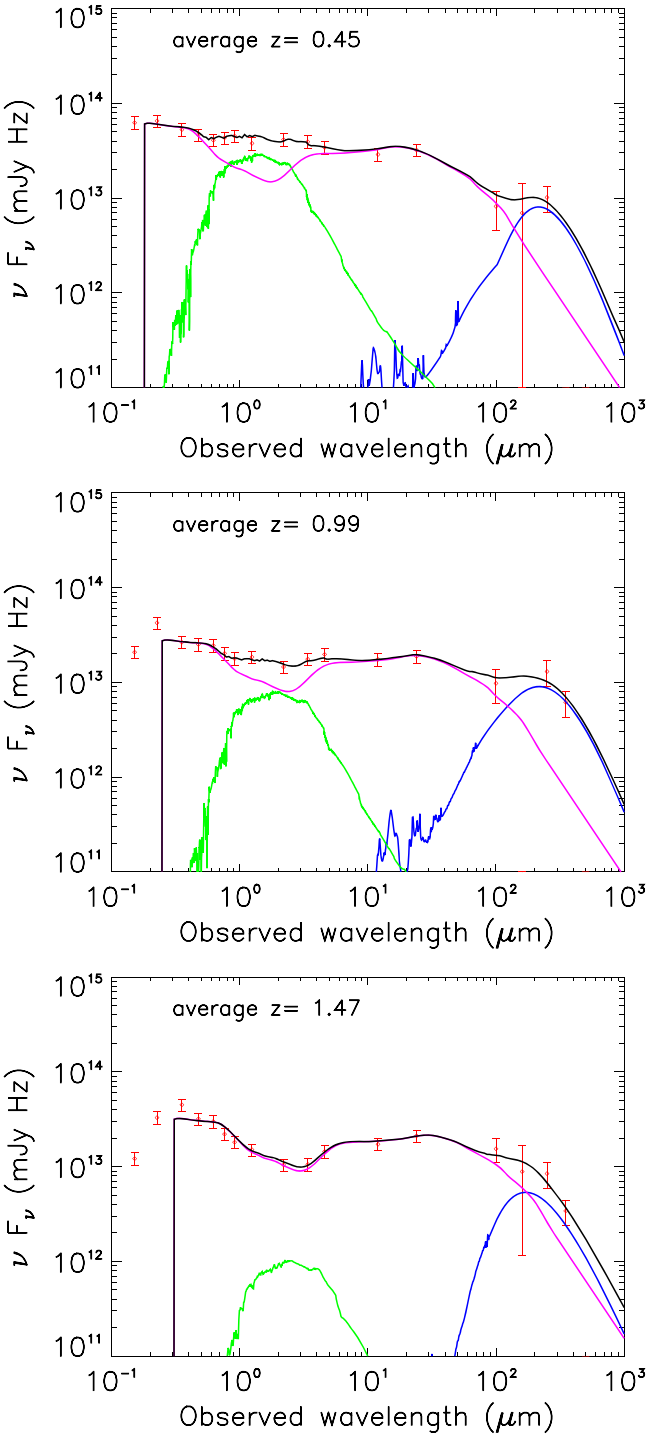

Figure 5. Average SEDs for Type-1 AGNs with no formal FIR detections in our sample in three discrete redshift bins: z = 0.1–0.7 (top, 24 sources), 0.7–1.2 (middle, 24 sources), and 1.2–1.9 (bottom, 18 sources). Symbols are the same as in Figure 4.

according to the parameters in Table 2. The resulting average SEDs in the three redshift bins (i.e., z = 0.1–0.7, 0.7–1.2, and 1.2–1.9) are shown in Figure 5, to be compared with the SEDs of the sources detected individually (e.g., Figure 4). The SEDs are similar, except the FIR peak is modestly weaker in the SEDs of the stacked signals.

3.2.3. Nature of the Far-infrared Excess

We now explore the nature of the FIR peak in the quasar SEDs. We display the [250/24 μm] flux ratio for the individual *Herschel*-detected objects as a function of redshift in Figure 6, along with the upper limits for the *Herschel*-non-detected

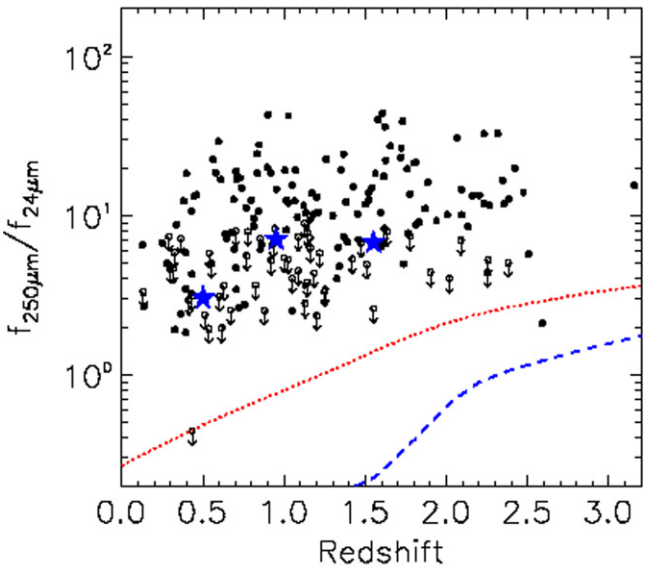

Figure 6. Observed-frame [250/24 μm] flux ratio vs. source redshift for the Type-1 AGNs in our sample. The downward pointing arrows indicate the sources not detected at 250 μm, based on 3σ upper limits. The five-pointed stars are the average values for *Herschel*-non-detected Type-1 AGNs from our stacking analyses (see Section 3.2.2). The dotted (red) line is the [250/24 μm] flux ratio of the Type-1 AGN template from Elvis et al. (1994). The dashed (blue) line is the flux ratio of a typical Type-1 AGN template from Fritz et al. (2006).

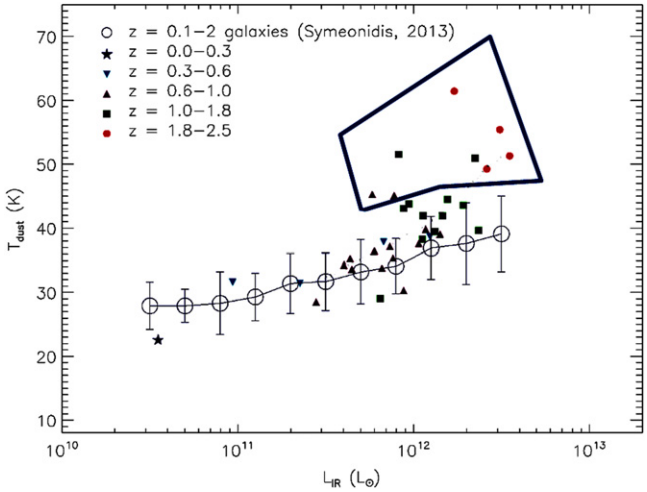

Figure 7. FIR dust temperature vs. total infrared luminosity (rest-frame 8–1000 μm). The big circles (blue) show the *L–T* relation of star-forming galaxies (z = 0.1–2) derived from HerMES and PEP data in COSMOS, GOODS-S, and GOODS-N fields (Symeonidis et al. 2013). The error bars show the 1σ scatter of the *L–T* relation. The blue irregular polygon encloses the sources with strong warm infrared components. The remaining sources are compatible with the *L–T* relation, particularly if one allows for modest warm components in a few of them.

AGNs and the three average values for the stacked SEDs. We also plot the flux ratios of a theoretical AGN template from Fritz et al. (2006) and a Type-1 AGN template from Elvis et al. (1994). The individual sources, upper limits, and stacked points all fall far above the model predictions. That is, AGN dust heating is unlikely to produce adequate FIR emission even if large (kpc-scale) tori are assumed (Ballantyne et al. 2006; Fritz et al. 2006). Therefore, the prominent FIR excess over the AGN templates indicates that a star formation component may contribute significantly to the FIR. Support for this conclusion is provided in Section 3.4, where we show that the FIR SEDs for most of the sources are similar to those of normal star-forming galaxies of similar luminosity.

3.3. The FIR Dust Temperature and Mass

We estimate the temperature of the FIR-emitting dust using a single-temperature gray-body model, of the form $B_\nu(T_d)[1 - e^{-\tau_d}]$, where $B_\nu(T)$ is the Planck function and τ_d is the frequency-dependent dust optical depth. The dust is optically thin in the FIR, and we have $1 - e^{-\tau_d} \approx \tau(\nu) = \tau(\nu_0)(\nu/\nu_0)^\beta$. Studies of local galaxies (Hildebrand 1983; Dunne & Eales 2001; Gordon et al. 2010) show that a value of $\beta = 1.5$ is a good estimate of the emissivity index for active star formation regions. We use the same criteria as in Hwang et al. (2010) to select sources with well-sampled SEDs around the peak of the FIR emission, i.e., there should be at least one flux measurement shortwards and longwards of the FIR peak, and the FIR SED should be physical (convex, not concave). There are 36 Type-1 AGNs in our sample that meet these conditions. The dust temperatures of these AGNs have large scatter from 22 to 62 K. As shown in Figure 7, we compared the results with the luminosity–temperature relation for star-forming galaxies at z = 0.1–2 derived from HerMES and PEP data in the COSMOS, GOODS-S, and GOODS-N fields (Symeonidis et al. 2013). The majority of the AGNs with cold dust temperatures lie within the 1σ range of dust temperature of star-forming galaxies, suggesting that the origin of their FIR emission is the same as for the cold dust in normal galaxies, that is star formation. Most such AGNs are at the lower luminosity end. The galaxies with temperatures significantly above expectations for star-forming galaxies all have warm components (Section 3.4.3) that make determining the behavior of any cold dust ambiguous.

For the galaxies where the FIR is dominated by the emission of cold dust, we can estimate the required mass of interstellar material. In the optically thin limit,

$$M_{\rm dust} = \frac{S_\nu D_{\rm L}^2}{\left(1+z\right)\kappa\left(\nu_{\rm r}\right)B_{\nu_{\rm r}}\left(T_{\rm dust}\right)}, \quad (1)$$

where S_ν is the observed flux density at ν, $\nu_{\rm r}$ is the rest-frame frequency, and the mass absorption coefficient, $\kappa(\nu_{\rm r}) = \kappa_0(\nu_{\rm r}/\nu_0)^\beta$, is approximated by a power law. Here we take $\kappa_0(125\ \mu{\rm m}) = 18.75\ {\rm cm^2\ g^{-1}}$ from Hildebrand (1983). The FIR-emitting dust mass ranges up to $9 \times 10^8\ M_\odot$, with a median value of $2 \times 10^8\ M_\odot$, indicating huge reservoirs of gas in these systems. The large FIR luminosities for most of the other *Herschel*-detected systems also indicate large amounts of interstellar material.

3.4. Type-1 SED Decomposition

We will show that the SEDs in Figures 4 and 5 can be explained in terms of three dominant SED components: (1) an averaged Type-1 quasar continuum to supply the UV (the "big blue bump" and to fill in the NIR; (2) the FIR SED of a luminous star-forming galaxy; and (3) the SED of a moderately old stellar population, which peaks at wavelengths slightly longer than 1 μm. These components are shown in the figures. In a few cases we need to add a warm FIR component. The overall simplicity of the SED (only three dominant

components) underlies the success of our fitting it to extract the underlying properties of the sources. SED decomposition can determine quantitatively the relative contribution of the AGN and the old stellar population in the NIR and of the AGN and star formation in the FIR.

3.4.1. Decomposition Procedures

One of the uncertainties for the SED decomposition is the lack of a clean template of a naked Type-1 AGN SED. Numerical AGN models and semi-analytic models provide candidate templates. The numerical models assume a central point-like energy source with a broken power-law SED surrounded by a smooth or clumpy dust distribution, and then solve the radiative transfer equation (e.g., Fritz et al. 2006). Templates generated using this method must make assumptions about the dust distribution geometry and compositions. For semi-analytic methods (e.g., Mullaney et al. 2011; Sajina et al. 2012), the SED is taken to be a broken power law based on physical assumptions for hot and warm components, and a modified blackbody beyond a given wavelength. Thus, both the numerical and semi-analytic methods are based on assumptions and introduce a number of free parameters.

To minimize the number of free parameters in our fits, we use an empirical AGN SED template (Elvis et al. 1994) to determine the FIR properties of our sources, and to estimate the relative contribution from the AGN and the host. This template may include a contribution from star formation and hence be too bright in the FIR. In Appendix C, we derive a correction to the template that represents a bounding condition for maximal star formation. We begin with the published template and consider the implications of this second case in Section 3.4.2.

We model the observed SED as a linear sum of a stellar component, a star formation component, and an AGN component. We also assume that the UV emission arises from the AGN rather than star formation. The star formation and AGN are taken to be independent and not to affect each other. For the star formation component, we use the ten IR galaxy templates from Rieke et al. (2009) for luminosities of $10^{9.75}\,L_{\odot}$ to $10^{12}\,L_{\odot}$. This restricted range of IR luminosity has been shown to give appropriate FIR SEDs for galaxies at the redshifts in our study (Rujopakarn et al. 2013). For the stellar component, we use 24 simple stellar population SEDs from Bruzual & Charlot (2003), assuming a Salpeter initial mass function (IMF), Padova evolutionary tracks, and solar metallicity, at ages from 0.4 Myr to 13 Gyr. Populations older than 1 Gyr have very similar SEDs in the NIR and beyond, with any differences confined to shorter wavelengths (where the stellar output is overwhelmed by that of the AGN). We also make sure the stellar component is not older than the age of the universe. As necessary, we apply foreground extinction to the AGN template; we use the Galactic extinction curve above 1 μm (Rieke & Lebofsky 1985), and use a SMC extinction curve below 1 μm (Gordon et al. 2003) (see Section 3.1.3 for more details about the reddening model).

We fit the above model to the data for rest wavelengths from 1216 Å to 1000 μm (we do not use the photometry short of 1216 Å due to Lyα forest absorption). Specifically, we use photometry from *GALEX*, SDSS, *J*, *K*, *WISE* (3.4, 4.6, and 12 μm bands), 24 μm, *Herschel* (100, 160, 250, 350, and 500 μm bands) if they are available. There are six degrees of freedom in the fitting: choosing the best fitting (1) IR star formation and (2) optical/NIR stellar population templates from the libraries, (3) determining the extinction to the AGN, and normalizing (4) the Type-1 AGN, (5) star formation, and (6) stellar population templates. We use Levenberg–Marquardt least-squares fitting to find the best solution among these degrees of freedom.

3.4.2. SED Decomposition Results

Figures 4 and 5 display examples of the SED decomposition results. In the rest-frame UV band and the MIR, the AGN always dominates the emission for our sample. The UV and optical are dominated by thermal emission from an accretion disk, and a significant portion of the NIR output is from hot dust warmed by the AGN. Many SEDs show a minimum at 1 μm (rest-frame), resulting from the upper temperature limit (sublimation temperature) for grains that can survive in the vicinity of an AGN. The stellar component contributes in the NIR, sometimes producing a NIR peak, or making the SED flat near 1 μm. The contribution from the stellar component is generally more significant at lower redshift. It fades quickly as the redshifts of the sources increase, as a result of our 24 μm selection being dominated by the AGN and selecting increasingly luminous AGNs with increasing redshift. A star formation component is needed for 95% (102 out of 107) of the *Herschel*-detected sources, but the contribution of this component in the FIR varies substantially from source to source. A star formation component is also required in all three redshift bins for the stacked SEDs of the sources not detected individually with *Herschel*.

We have tested the necessity for star formation in the SED fits on the minority of sources where the FIR luminosity is relatively small, namely quasars number 8, 24, 27, 38, 48, 49, 61, 64, 69, 71, 77, 90 (distributed over nearly the full redshift range of the sample, i.e., from $z = 0.4$ to $z = 2.1$). We determined the minimum χ^2 for fits to the measurements at rest-frame wavelengths $> 6\,\mu$m, assuming 20% minimum effective error (larger errors for low S/N measurements) for each photometric measurement and using just the Elvis template. We evaluated the quality of the fits based on the values of χ^2 and the number of degrees of freedom for each galaxy, and then compared with the result with a star-forming template added. The probability of the fit being adequate with the Elvis template alone was <0.3% in every case. With the star-forming template added, the probability that the fit was adequate was >15% for seven (of twelve) cases, ⩾1% in three more, and was always much larger than the probability without the star-forming template. The two cases with bad fits had FIR measurements that were incompatible with any smooth fit (i.e., the measurements indicated minima in the FIR, which is not a physically plausible behavior), suggesting that the issue is the data. Thus, even for the individual systems where we find relatively weak star formation, it is an essential part of the SED fits. This conclusion is consistent with our finding in stacking the sources not detected individually that a spectral component due to star formation is present on average, although weaker than for the individual *Herschel*-detected objects.

A source of systematic error in the decompositions is the probable inclusion of some FIR emission due to star formation in the Elvis AGN template. We have determined a bounding case (maximal level of star formation) for this effect as described in Appendix C. Around 160 μm, this estimate attributes 75% of the template emission to star formation, so it is impossible to apply a substantially larger correction. We

have repeated the SED decomposition with this star formation-adjusted template and find for typical cases (where the FIR star formation component of the decomposition is substantially stronger than the AGN template) that the upward correction in the star-forming luminosity is only ~10%. Larger corrections apply for the 12 sources listed in the preceding paragraph with relatively weak star formation. Based on the star formation-adjusted Elvis template, the individual corrections to the estimated star-forming luminosities for these systems are 18%, 9%, 11%, 17%, 40%, 11%, 9%, 17%, 8%, 48%, 29%, and 11% respectively for galaxies 8, 24, 27, 38, 48, 49, 61, 64, 69, 71, 77, and 90. For the stacked SEDs, the possible increases in the SFRs are 25%, 10%, and 46% respectively, for $0.1 < z < 0.7$, $0.7 < z < 1.2$, and $1.2 < z < 1.9$. Applying these corrections would increase the necessity for star-forming templates in fitting the *Herschel*-detected objects and would put the stacked results closer to the ones for the *Herschel*-detected galaxies and emphasize that the non-detected galaxies are, on average, similar but modestly fainter in the FIR.

There is another important conclusion indicated by Figures 4 and 5 and the SED decomposition. For all members of our sample, the 24 μm flux density is dominated by emission from the AGN, whereas the emission in the *Herschel* bands is dominated by star formation. Thus, the sample selection criteria are unaffected by the level of star formation in the host galaxies. The fact that the *Herschel* detection rate does not fall significantly with increasing redshift indicates that both the AGN and star-forming luminosities in the sample increase with redshift at roughly similar rates, that is, the star formation in the host galaxy must be roughly proportional to AGN luminosity (at least that at 24 μm).

3.4.3. Warm Excess

We found a strong excess above the SED decomposition result from 3 to 60 μm (rest-frame) for some sources (see Figure 8 as an example); an additional warm component in addition to the star formation and AGN templates is needed to obtain a good fit. A similar excess is also found in some $z \sim 6$ quasar SEDs (Leipski et al. 2013, 2014). A theoretical model of a parsec-scale starburst disk (Thompson et al. 2005; Ballantyne 2008) predicts that a warm component heated by star formation would emit strongly in this wavelength range. To introduce a minimum of free parameters, we added a component with this specific spectrum (Ballantyne 2008, Figure 7) to the SED decomposition template library. There are of course alternative possible origins for this emission. Figure 8 shows the comparison in one example of the SED fits before and after adding the warm component. The emission from the parsec-scale starburst disk reproduces the hot excess very well. The total luminosity from the warm component for this source accounts for 56% of the total IR luminosity in this example.

We judge the fits to require the warm component if the observed 12, 24, and 100 μm fluxes are about twice (or more) the fluxes from the SED decomposition only using AGN, stellar, and star formation templates. The results are summarized in Table 5. There are eight sources that require a warm component to achieve a satisfactory fit, with a contribution to the total IR luminosity in the range of 30%–75%.

We also tested the influence of a warm component on the conclusions from all of the fits where it did not appear to be required; the results are also in Table 5. The column for $L_{\rm SF,IR}$

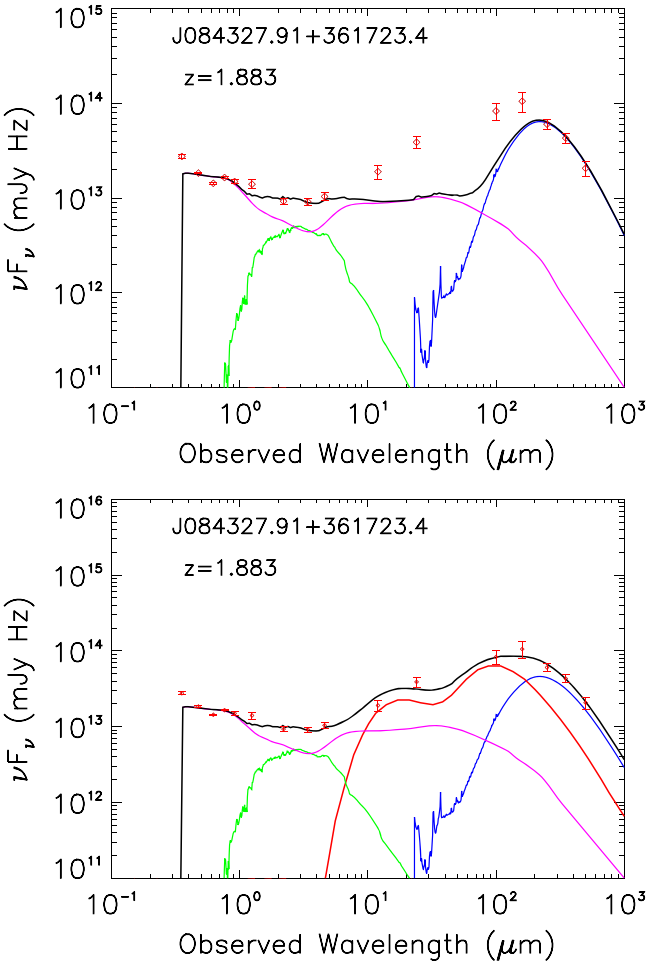

Figure 8. SED decomposition results for an AGN at $z = 1.883$. Top: decomposition with stellar, AGN, and star-forming galaxy templates only. The measurements from 10 to 200 μm (3 to 60 μm in the rest frame) are high, indicating a warm excess from the MIR to FIR. Bottom: the same as the top part but an additional warm component based on a model of a circumnuclear starburst has been added to improve the fit.

shows in parenthesis the fractional reduction in the luminosity of the star-forming component if the warm component is added to the fit; for example, for source 1, the fit is not improved with a warm component and there is no change in $L_{\rm SF,IR}$, whereas for source 2 the warm component improves the fit and reduces $L_{\rm SF,IR}$ by 10%. In this latter case, the total luminosity captured by the fit is also increased with the warm component, indicating that it accounts for measurements that lie above the simpler fit.

For galaxies that are relatively faint in the FIR, the introduction of a warm component can make the optimum fit ambiguous. For example, of the 12 galaxies with relatively weak FIR discussed in the preceding section, three (8, 24, and 64) could be fitted with a substantial warm component. Nonetheless, the purely star-forming FIR fits are also valid, all having probabilities >20% of being satisfactory according to the values of χ^2. Given that the warm component seems to be prominent at high redshift and/or high luminosity, and that these galaxies have low FIR luminosities and are at modest redshift, the star-forming template is the preferred fit.

In summary, the decomposition inputs are surprisingly simple: (1) a fixed AGN SED from Elvis et al. (1994) with adjustable foreground screen reddening; (2) a FIR SED appropriate for local LIRGs; (3) a stellar population

component—although we allowed a broad range of stellar population SEDs, the fits always converged on one appropriate for a relatively old population; and (4) the warm IR component.

3.5. Comparisons with Other Samples

3.5.1. Comparison of Herschel-detected and Non-detected AGNs in the UV and Optical

As discussed in Section 3.2.1, for the Type-1 AGNs there is no obvious difference between the *Herschel*-detected and *Herschel*-non-detected populations in the 24 μm flux density distribution, nor in the redshift distribution. We now expand that comparison to consider any differences in the UV and optical. The SDSS quasars are initially selected through a combination of optical colors and confirmed by optical spectroscopy (Richards et al. 2002). Richards et al. (2003) found that for them the relative color $\Delta(g' - i')$ is a good indicator of quasar redness for redshifts between 0.3 and 2.2. The relative color is the difference between the measured color of a given quasar and the median colors of quasars at the same redshift: a quasar with large $\Delta(g' - i')$ could either be intrinsically red or be reddened by dust.

There is SDSS coverage of 4.51 deg^2 of our survey area. There are 84 SDSS optically selected Type-1 AGNs in this area and 185 AGNs in our 24 μm-selected sample. 61 AGNs are selected by both samples; 23 SDSS AGNs are not included in our sample due to their 24 μm flux densities being below 1 mJy. The plot in the upper panel of Figure 9 shows the colors of the 185 SDSS-detected-and-24 μm-detected quasars $(g' - i')$ (corrected for Galactic extinction) compared with those of SDSS quasars in general. We determine the median colors of quasars at a given redshift (the solid line) using data from the SDSS DR7 Quasar Catalog (Schneider et al. 2010). They represent a quasar population that is optically bright and not or only slightly affected by dust reddening. The 24 μm-detected quasars range from this line to being significantly (~1 mag) redder; this behavior is independent of FIR properties. The K–S test shows that the relative color distributions of *Herschel*-detected and -non-detected AGNs are not statistically distinguishable (P-value = 0.948). In other words, *Herschel*-detected Type-1 AGNs are not significantly redder than *Herschel*-non-detected ones in the optical. This indicates that the dust responsible for the *Herschel* detections is not producing any significant dust extinction along the line of sight toward the AGNs. This does not contradict our fits that included reddening of the quasar template; it just indicates that the dust responsible does not dominate the FIR emission.

3.5.2. SDSS Optically Selected Type-1 AGNs

In Figure 10 we compare the redshift and i' band magnitude distributions for the SDSS and 24 μm samples. Basically the two samples select sources in the same redshift range. The 24 μm sample includes more sources faint in the i' band than the SDSS sample. The 23 SDSS AGNs that are not included in the 24 μm sample are evenly distributed over $z \sim 0$–4, and most of them lie at the faint end of the i' band magnitude distribution. The majority of these 23 SDSS AGNs are detected at 24 μm, with flux densities in the range of 0.2–1.0 mJy. Therefore the bright 24 μm source selection has a large overlap with SDSS selection, but in addition finds many more (by a factor ~2) Type-1 AGNs based on their optical spectra.

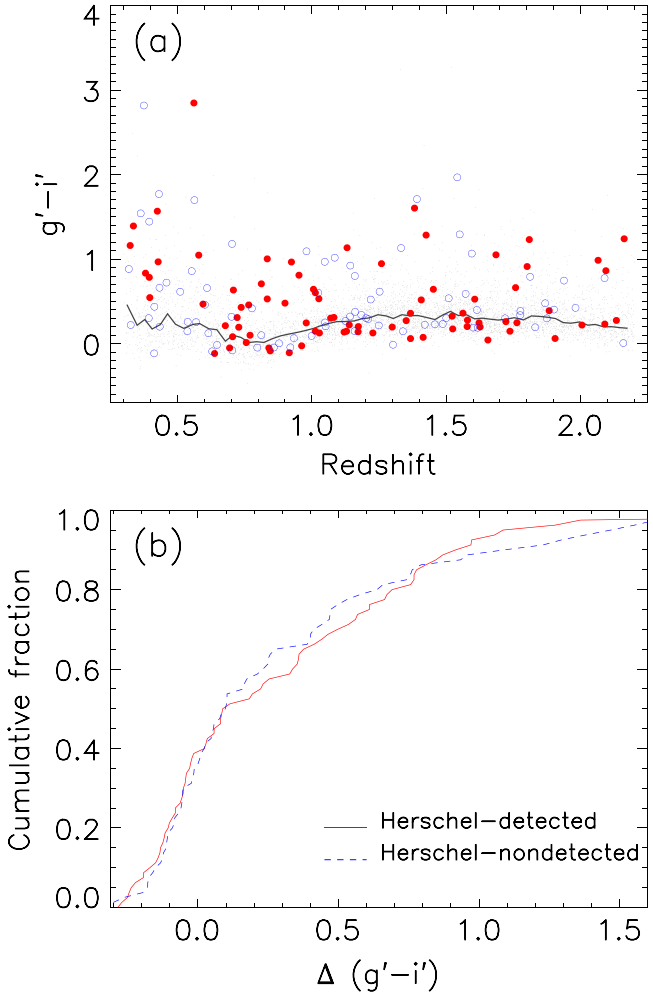

Figure 9. (a) Observed-frame color $(g' - i')$ of Type-1 AGNs in our sample as a function of redshift. The filled circles (red) show *Herschel*-detected Type-1 AGNs; the unfilled circles (blue) show *Herschel*-non-detected Type-1 AGNs. The small dots (gray) represent the SDSS optically selected Type-1 quasars from the SDSS Data Release 7 Quasar Catalog (Schneider et al. 2010). The solid black line is the median value of the color of SDSS optically selected Type-1 quasars. (b) The K–S test shows that the relative color distributions of *Herschel*-detected (red solid) and non-detected (blue dashed) AGNs are not statistically distinguishable (P-value = 0.973).

In the upper panel of Figure 11 we plot the relative color $\Delta(g' - i')$ (see Section 3.5.1) as a function of redshift for these two samples. Most SDSS AGNs are scattered around the relative color $\Delta(g' - i') = 0.0$. This indicates that the SDSS AGNs in our survey fields are typical of SDSS AGNs in general since the the median value of the color $g' - i'$ is calculated from the large SDSS Type-1 AGN sample. Our 24 μm-selected sample includes additional red sources not identified by optical colors. At $z < 1$, the red colors in our sample may partly arise from the contribution of the stellar component in the optical. Above $z \sim 1$, the 24 μm selection picks up more luminous AGNs, and the SED is dominated by the AGN from the UV to the MIR; these red sources probably have either strong dust reddening or intrinsically red AGN continua.

The lower panel of Figure 11 shows the observed-frame [24 μm/i'] flux ratio as a function of redshift for these two samples. The 23 SDSS AGNs that our 24 μm selection missed show small [24 μm/i'] flux ratios due to their low 24 μm flux

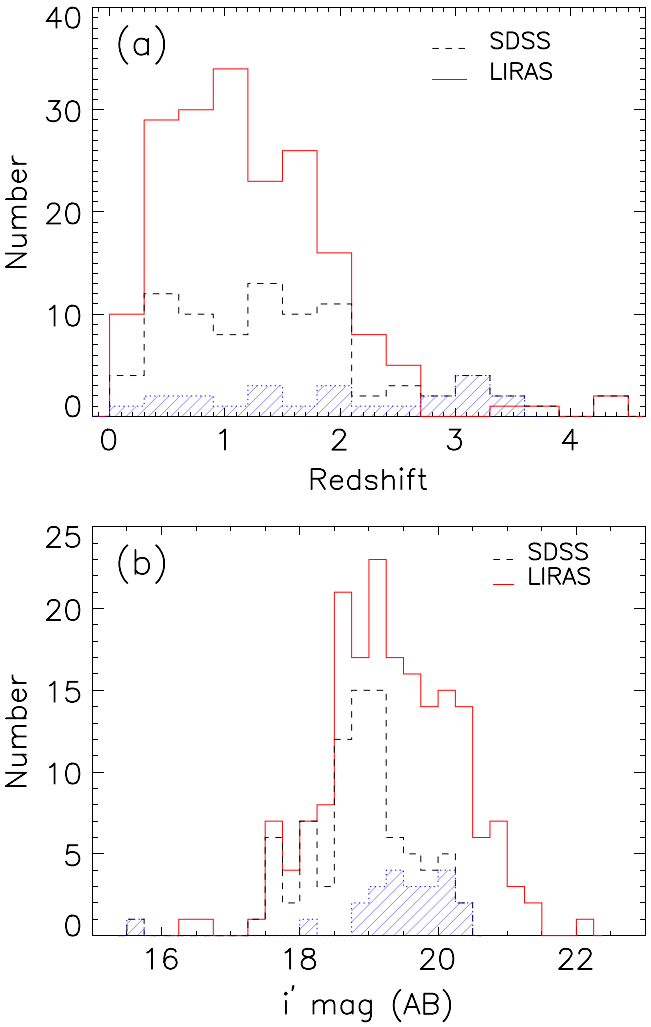

Figure 10. Comparison of Type-1 AGNs in our sample and SDSS optically selected Type-1 AGNs. (a) Redshift distribution. The red-solid histogram is Type-1 AGNs in our sample, while the black-dashed histogram is the SDSS optically selected sample. The blue hatched histogram is the SDSS AGNs that are not included in our sample due to their 24 μm flux density being below 1 mJy. (b) i' magnitude distribution. The symbols are the same as in the top panel.

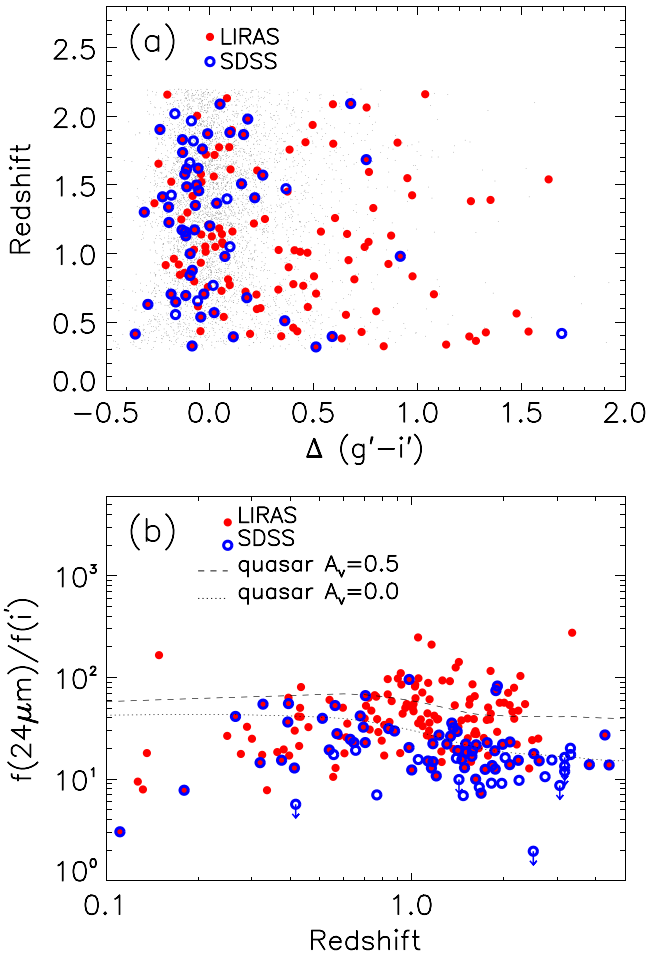

Figure 11. Comparison of Type-1 AGNs in our sample and SDSS optically selected Type-1 AGNs. (a) The relative observed-frame color $\Delta(g' - i')$ as a function of redshift. The red filled circles show Type-1 AGNs in our sample. The blue circles show the SDSS optically selected AGN sample within the same area; they are open if the source is not in our sample. The small dots (gray) represent the SDSS optically selected Type-1 quasars from SDSS Data Release 7 Quasar Catalog (Schneider et al. 2010). (b) The [24 μm/i'] flux ratio as a function of redshift. Symbols are the same as in the upper panel. The dotted and dashed lines are the flux ratios calculated from Elvis's quasar template (1994) with reddening $A_V = 0$ and 0.5, respectively.

densities, and most of them are above $z \sim 1$. The contribution of the stellar component is also reflected in the [24 μm/i'] flux ratio for sources at $z < 1$ for both samples. For most of the AGNs at $z < 1$, the [24 μm/i'] ratios are lower than that predicted by a quasar template. At $z > 1$, the SDSS-selected AGNs are more consistent with the ratios predicted by the quasar template with $A_V = 0$, while about half of the 24 μm-selected AGNs are more consistent with the template-predicted ratios with $A_V = 0.5$. The redder color of [24 μm/i'] for 24 μm-selected AGNs may partly be due to dust reddening or to intrinsically red continua in the optical, or partly due to the warm excess in the MIR enhancing the 24 μm flux density. In any case, these results demonstrate that 24 μm selection yields a substantial number of red quasars that are absent in purely optical selection.

3.5.3. X-Ray-selected AGNs

We estimated the equivalent AGN X-ray flux to our 1 mJy selection threshold at 24 μm using the bolometric conversion from Lusso et al. (2012), obtaining a flux of 10^{-14} erg cm^{-2} s^{-1} in the 0.5–2 keV band. From the number of X-ray sources at a similar detection limit found by Cardamone et al. (2008), we expect a total of ~260 X-ray-selected AGNs above this flux level in our total field. Our sample includes 205 IR-selected sources, or about 240 if corrected for the ~18% incompleteness. However, from Cardamone et al. (2008), we expect the two samples to have different properties, despite the near coincidence in numbers.

The intrinsic X-ray luminosity in the [2–10] keV band for a typical AGN at $z \sim 1$ in our sample is 2×10^{44} erg s^{-1}, converted from a bolometric luminosity ($\sim 5 \times 10^{45}$ erg s^{-1}) using the bolometric to X-ray luminosity correction in Figure 9 of Lusso et al. (2012). The failure to detect ~80% of the sample in X-rays suggests that some members are moderately absorbed, consistent with their selection in the IR. From these arguments, most of the AGNs in our sample are intrinsically more luminous in the X-ray, compared with the X-ray-selected, moderate-luminosity ($L_X = 10^{42} - 10^{44}$ erg s^{-1}) AGN sample in Mullaney et al. (2012). AGNs in both samples have

comparable IR star formation luminosities and (specific) SFRs, and all reside in massive, main-sequence star-forming galaxies. However, in the optical and NIR, the SEDs of those X-ray-selected, moderate-luminosity AGNs are dominated by stellar emission (see the average SED in Figure 12 of Mullaney et al. 2012), while for our sample, emission from the AGNs is dominant in the optical and NIR, except for some sources in the lowest redshift bins. From Cardamone et al. (2008), the X-ray sample is expected to include nearly 50% of sources where the NIR is dominated by stellar emission, whereas the IR-selected sample is expected to be dominated by power-law sources in the NIR (see Donley et al. 2008). That is, a significantly higher fraction of the AGN luminosity emerges in the IR for our IR-selected sample than is the case for X-ray-selected samples.

4. 24 μm-SELECTED TYPE-2 AGNs

We now describe the Type-2 AGNs identified from the same data set. Many members of the Type-2 sample are at relatively low redshift and their AGNs tend to be of lower luminosity than the Type-1 objects. After finding the Type-2 objects, we will identify a subsample that is directly comparable with the Type-1 AGNs in terms of redshift, black hole mass, and accretion rate.

4.1. Type-2 AGN Identification

The sample of LIRAS Type-2 AGNs is constructed based on the following selection criteria:

1. *Spitzer*/MIPS 24 μm flux densities above 1 mJy.
2. Optical spectra showing narrow permitted emission lines (FWHM $< 1200\,\mathrm{km\,s^{-1}}$) with high-ionization line ratios.
3. If $z > 0.34$, [Ne V]$\lambda\lambda$3347, 3427 detected or FWHM ([O III]) $> 400\,\mathrm{km\,s^{-1}}$.

Because the primary identification is based on emission line strengths rather than widths, well-calibrated spectra are required. To maintain consistency in the classification, we only used Hectospec data; as a result, a few AGNs identified in SDSS that were not targeted with Hectospec may have been omitted from the Type-2 sample (see Tables 6 and 7). We exclude any AGNs in the clusters according to the source redshift.

A Hectospec fiber diameter subtends 1.″5 on the sky. At $z = 0.3$, 1.″5 subtends about 6.7 kpc, and at $z = 0.6$, 10 kpc, so the Hectospec fiber includes substantial light from the host galaxy. The AGN emission lines can therefore be contaminated by stellar absorption lines from the galaxy. Following Hao et al. (2005), we used the following procedures to subtract the host galaxy contribution before measuring the AGN emission lines. First, we select a sample of 212 high S/N spectra of pure absorption-line galaxies from SDSS Data Release 7.[11] Second, we apply principal component analysis to construct a library of galaxy absorption-line spectral templates. Third, we fit a galaxy template, an A-type star template to account for the young stellar population in the host galaxy, and a power-law component proportional to $\lambda^{-\alpha}$ for the nonthermal component from the AGN. A χ^2 minimizing algorithm was used to determine the synthetic stellar absorption spectrum. Only after stellar and power-law continuum subtraction from all the spectra do we measure the emission lines.

[11] http://www.sdss.org/dr7/

We fitted the following emission lines for each spectrum: Hα, [N II]$\lambda\lambda$6584, 6548, Hβ, [O III]λ5007. We rejected all objects with broad components (FWHM $> 1200\,\mathrm{km\,s^{-1}}$) in their emission lines (i.e., in Hα, Hβ, or Mg II 2800). The minimum [O III] line width criterion of $400\,\mathrm{km\,s^{-1}}$ was based on the fitted width with no allowance for the spectral resolution. Given the resolution of $R \sim 1000$, it corresponds to a threshold of about $270\,\mathrm{km\,s^{-1}}$ for the intrinsic quasar line width. It should therefore not eliminate legitimate AGNs (Brotherton 1996) but protects against inclusion of chance anomalous star-forming galaxies (e.g., Stanway et al. 2014). We also rejected weak emission-line galaxies, i.e., the equivalent width of one of Hα, [O III], or Hβ was required to be greater than 3 Å.

There are several line flux ratio criteria to distinguish Type-2 AGNs from other narrow emission line objects (e.g., Kewley et al. 2001; Kauffmann et al. 2003). Here we use the one from Kewley et al. (2001) for objects at $z < 0.34$,

$$\log\left(\frac{[\mathrm{O\,III}]\,\lambda5007}{\mathrm{H}\beta}\right) > \frac{0.61}{\log([\mathrm{N\,II}]/\mathrm{H}\alpha) - 0.47} + 1.19. \quad (2)$$

Since [N II] is redshifted out of Hectospec spectroscopic range at $z > 0.34$, we use the following (Zakamska et al. 2003) for objects at $0.34 < z < 0.76$:

$$\log\left(\frac{[\mathrm{O\,III}]\,\lambda5007}{\mathrm{H}\beta}\right) > 0.3. \quad (3)$$

A few AGNs at $z < 0.34$ are identified from the BPT diagram even if their [O III] lines are narrower than $400\,\mathrm{km\,s^{-1}}$. Selection of Type-2 AGNs with $z > 0.76$ is not possible with our spectra since [O III] is redshifted out of the spectroscopic range.

The upper panel of Figure 12 shows the emission-line diagnostic diagram for Type-2 AGNs at $z < 0.34$ selected in our sample using Equation (2). The lower panel of Figure 12 shows the distribution of the [O III] to Hβ line ratio for all selected Type-2 AGNs at $0.34 < z < 0.76$.

4.1.1. Results

We identified a total of 85 24 μm-selected Type-2 AGNs over the 3.6 deg^2 survey area; 55 are securely detected at least in two *Herschel* bands, as listed in Table 6. Figure 13 shows two typical SEDs for *Herschel*-detected AGNs. The remaining 30 sources not detected with *Herschel* are listed in Table 7. The redshifts and key derived parameters of the *Herschel*-detected objects can be found in Table 8. We stacked the signals for *Herschel*-non-detected Type-2 AGNs in two redshift bins: 0.0–0.4 and 0.4–0.8. There are 14 and 13 sources in these two bins respectively, after rejecting those contaminated by close bright objects. The stacked SEDs are shown in Figure 14.

4.2. Morphologies

We visually examined the Suprime-Cam images (shown in Appendix A) to classify the *Herschel*-detected host galaxy morphologies (51 out of 55 sources have images of adequate quality). Although the images are not of sufficient resolution for a definitive determination of the morphologies of the entire Type-2 sample, they allow us to make plausible assignments for most members (summarized in Table 8). 12 of the 55 *Herschel*-detected galaxies either have no useful imaging

Table 6
Fluxes of the 24 μm-selected *Herschel*-detected Type-2 AGN Sample[a]

#	Source LIRAS	R.A. (J2000)	Decl. (J2000)	J (mJy)	K (mJy)	3.4 μm (mJy)	4.6 μm (mJy)	12 μm (mJy)	24 μm (mJy)	100 μm (mJy)	160 μm (mJy)	250 μm (mJy)	350 μm (mJy)	500 μm (mJy)
1	J101756.90+390528.0	154.4870647	39.0911158	2.140	2.337	1.14	0.86	3.33	6.41	95.45	100.84	52.66	24.71	12.98
2	J101805.64+385009.7	154.5235201	38.8360315	3.217	3.689	0.00	0.00	0.00	6.15	…	…	132.04	55.62	17.77
3	J145753.24+222422.7	224.4718447	22.4063113	1.190	1.550	0.70	0.53	1.01	1.51	31.49	43.06	24.72	13.63	<12.39
4	J133250.99+501816.1	203.2124640	50.3044596	0.445	0.801	0.50	0.45	1.12	1.49	39.55	56.07	27.41	10.88	<12.39
5	J083713.49+150037.4	129.3061885	15.0103981	0.681	1.135	0.54	0.40	1.00	1.23	…	…	43.56	16.00	<12.39
6	J080102.09+355132.2	120.2587258	35.8589486	0.432	0.519	0.32	0.25	1.00	4.93	21.28	13.53	8.82	<10.99	<12.39
7	J133644.33+405854.9	204.1847156	40.9819103	0.594	0.903	0.43	0.35	0.95	2.34	…	…	25.00	19.81	11.59
8	J101623.97+385840.1	154.0998940	38.9778032	0.464	0.818	0.48	0.51	2.29	9.09	567.79	548.25	297.52	149.83	62.02
9	J172109.90+263455.1	260.2912375	26.5819727	1.077	1.369	0.73	0.61	1.64	3.33	77.08	…	67.66	40.55	13.02
10	J172022.13+263626.6	260.0922172	26.6073774	0.436	0.574	0.28	0.34	1.15	3.10	25.15	17.24	9.25	8.61	<12.39
11	J212928.92+000415.0	322.3704858	0.0711106	0.518	0.833	0.46	0.44	1.09	2.56	24.91	42.34	26.08	8.98	<12.39
12	J133323.14+503028.2	203.3464326	50.5078346	0.177	0.317	0.16	0.15	0.54	1.29	37.53	44.30	22.42	16.43	<12.39
13	J073313.08+313954.6	113.3045032	31.6651796	0.276	0.422	0.17	0.16	0.54	1.80	25.52	32.16	24.88	15.79	<12.39
14	J073133.58+314113.0	112.8898963	31.6869460	0.278	0.430	0.25	0.21	0.73	2.34	23.76	53.87	20.98	12.54	<12.39
15	J172004.43+262701.2	260.0184527	26.4503445	0.565	0.885	0.58	0.61	2.10	2.75	50.98	36.52	36.13	17.08	<12.39
16	J080128.61+355046.1	120.3692138	35.8461340	0.370	0.606	0.56	0.58	3.40	11.44	…	…	152.02	75.30	38.84
17	J142511.92+374729.5	216.2996725	37.7915255	0.252	0.444	0.27	0.28	1.05	2.33	49.33	74.71	32.26	10.96	<12.39
18	J084213.26+363020.5	130.5552534	36.5056852	0.230	0.379	0.22	0.24	1.29	1.80	50.51	55.41	33.23	18.71	<12.39
19	J131130.41−013216.1	197.8767161	−1.5378040	0.302	0.426	0.23	0.21	1.56	3.09	34.49	43.67	31.76	11.78	<12.39
20	J084339.40+292025.2	130.9141872	29.3403267	0.098	0.169	0.10	0.10	0.94	3.16	34.81	61.08	24.18	19.97	<12.39
21	J082644.54+040705.4	126.6855883	4.1181584	0.324	0.628	0.35	0.50	1.18	3.29	43.12	60.37	29.16	11.38	<12.39
22	J171957.79+264027.3	259.9907836	26.6742595	0.475	0.694	0.34	0.41	1.82	7.97	28.20	20.81	15.77	8.74	19.18
23	J133428.33+502829.0	203.6180277	50.4747238	0.300	0.567	0.40	0.32	0.67	1.15	…	…	37.80	20.14	<12.39
24	J101641.15+384703.4	154.1714461	38.7842743	0.133	0.284	0.21	0.22	0.97	1.15	63.80	80.88	47.15	21.36	<12.39
25	J084209.68+293836.1	130.5403523	29.6433488	0.423	0.648	0.29	0.27	0.84	1.36	…	…	41.68	18.08	<12.39
26	J133553.40+405459.2	203.9725041	40.9164534	0.354	0.631	0.34	0.31	1.38	2.71	27.57	57.40	50.62	32.21	25.29
27	J101653.99+390530.9	154.2249579	39.0919172	0.216	0.371	0.23	0.14	0.60	1.32	27.80	17.83	21.81	10.23	<12.39
28	J212914.75+001947.6	322.3114643	0.3298990	0.202	0.480	0.29	0.21	0.73	1.29	20.07	18.12	19.50	12.08	<12.39
29	J073322.45+313915.5	113.3435220	31.6543155	0.206	0.370	0.00	0.00	0.00	2.25	18.79	<16.89	14.16	<10.99	<12.39
30	J010625.81+005343.3	16.6075479	0.8953710	0.334	0.551	0.32	0.31	1.05	1.02	20.69	15.68	28.07	<10.99	<12.39
31	J010658.45+010146.8	16.7435422	1.0296640	0.092	0.149	0.09	0.11	0.38	1.02	<10.89	<16.89	23.89	13.73	<12.39
32	J010658.95+010438.3	16.7456271	1.0773157	0.143	0.215	0.20	0.18	0.99	7.44	15.46	11.92	8.55	<10.99	<12.39
33	J090016.83+205502.9	135.0701310	20.9174622	0.247	0.468	0.32	0.29	1.39	4.03	63.39	95.23	52.42	31.54	14.66
34	J090034.67+204013.2	135.1444618	20.6703248	0.196	0.411	0.47	0.64	1.54	4.80	20.43	15.60	13.99	<10.99	<12.39
35	J101805.93+385755.8	154.5247231	38.9655001	0.249	0.491	0.39	0.49	3.96	8.02	144.51	167.92	127.85	50.12	22.64
36	J213007.49+001419.1	322.5312077	0.2386458	0.143	0.314	0.23	0.25	0.86	1.98	34.77	19.10	36.70	18.21	<12.39
37	J101742.86+385540.9	154.4285880	38.9280170	0.077	0.142	0.13	0.11	0.38	2.09	12.80	<16.89	22.90	24.75	<12.39
38	J024858.24−032446.9	42.2426621	−3.4130394	0.085	0.159	0.16	0.17	0.88	3.50	16.52	52.37	41.91	27.90	12.31
39	J133241.05+502502.9	203.1710392	50.4174627	0.228	0.477	0.38	0.30	1.02	2.76	43.27	59.12	45.83	23.88	<12.39
40	J101800.18+385833.5	154.5007626	38.9759692	0.133	0.228	0.19	0.13	0.83	4.31	56.98	42.37	13.88	<10.99	<12.39
41	J083759.22+145557.1	129.4967515	14.9325181	0.064	0.134	0.13	0.09	0.71	1.36	…	…	41.79	34.80	21.29
42	J083244.18+654251.5	128.1840854	65.7143033	0.061	0.122	0.20	0.41	1.32	5.14	32.38	18.25	<10.19	<10.99	<12.39
43	J073258.91+313724.5	113.2454480	31.6234624	0.034	0.085	0.07	0.07	0.57	1.04	36.04	33.45	19.46	11.41	<12.39
44	J171919.29+262835.3	259.8303805	26.4764833	0.114	0.217	0.18	0.12	0.79	2.35	…	…	35.64	22.53	<12.39
45	J080049.66+360514.2	120.2069181	36.0872688	0.065	0.121	0.16	0.23	1.34	3.13	26.63	<16.89	18.13	<10.99	<12.39
46	J133616.50+405529.4	204.0687537	40.9248415	0.028	0.061	0.06	0.06	0.24	1.09	11.46	<16.89	32.09	37.36	28.90
47	J101714.14+390124.4	154.3089014	39.0234514	0.164	0.318	0.40	0.32	1.36	1.61	<10.89	<16.89	22.10	8.65	<12.39

Table 6
(Continued)

#	Source LIRAS	R.A. (J2000)	Decl. (J2000)	J (mJy)	K (mJy)	3.4 μm (mJy)	4.6 μm (mJy)	12 μm (mJy)	24 μm (mJy)	100 μm (mJy)	160 μm (mJy)	250 μm (mJy)	350 μm (mJy)	500 μm (mJy)
48	J101600.54+391049.3	154.0022496	39.1803572	0.143	0.278	0.25	0.20	0.56	1.12	⋯	⋯	104.50	56.55	28.51
49	J213011.84+000558.3	322.5493536	0.0995303	0.070	0.155	0.13	0.09	0.77	2.13	<10.89	<16.89	32.71	22.74	<12.39
50	J082927.84+654906.5	127.3660200	65.8184662	0.032	0.068	0.10	0.06	0.24	1.03	23.34	32.39	21.69	14.39	<12.39
51	J145635.24+222400.9	224.1468518	22.4002513	0.057	0.131	0.14	0.09	0.26	1.33	19.04	<16.89	17.88	<10.99	<12.39
52	J213015.48+000430.0	322.5645056	0.0752736	0.038	0.087	0.13	0.10	0.87	4.16	29.72	50.72	35.60	18.97	<12.39
53	J084317.56+293818.6	130.8231488	29.6385122	0.057	0.106	0.11	0.10	0.58	3.03	16.50	24.68	9.09	<10.99	<12.39
54	J015214.76+010705.7	28.0614845	1.1182565	0.064	0.121	0.14	0.15	1.16	9.26	58.47	46.49	41.03	12.97	<12.39
55	J090126.15+205632.1	135.3589767	20.9422619	0.033	0.098	0.15	0.08	0.73	1.29	26.69	43.98	49.10	26.55	12.88

Note.
[a] Upper limits are 3σ.

Table 7
Fluxes of the 24 μm-selected *Herschel*-non-detected Type-2 AGN Sample

#	Source LIRAS	R.A. (J2000)	Decl. (J2000)	z	J (mJy)	K (mJy)	3.4 μm (mJy)	4.6 μm (mJy)	12 μm (mJy)	24 μm (mJy)
1	J101813.08+390220.2	154.5544848	39.0389521	0.293	0.142	0.207	0.00	0.00	0.00	1.27
2	J083805.70+145152.9	129.5237579	14.8646849	0.345	0.097	0.263	0.79	1.30	3.30	9.08
3	J073301.63+314042.2	113.2567957	31.6783963	0.115	0.525	0.653	0.37	0.38	1.59	6.23
4	J024852.78−033551.5	42.2199003	−3.5976449	0.137	0.882	1.177	0.64	0.51	0.69	1.63
5	J101814.47+385217.0	154.5602787	38.8716572	0.147	0.160	0.199	0.12	0.07	0.53	1.52
6	J164119.41+462953.5	250.3308715	46.4981864	0.191	0.553	0.779	0.57	0.62	1.37	2.99
7	J010623.62+005143.0	16.5984100	0.8622204	0.195	0.725	1.022	0.54	0.36	0.55	1.73
8	J090048.78+204448.2	135.2032534	20.7467242	0.329	0.032	0.053	0.00	0.00	0.00	1.48
9	J084402.38+292747.1	131.0099067	29.4630889	0.357	0.136	0.282	0.00	0.00	0.00	2.97
10	J133236.79+503032.9	203.1532919	50.5091500	0.375	0.173	0.267	0.21	0.16	0.70	2.95
11	J142526.99+375011.2	216.3624572	37.8364343	0.380	0.140	0.269	0.19	0.17	0.35	1.26
12	J133453.29+404827.1	203.7220565	40.8075180	0.389	0.034	0.057	0.04	0.07	0.52	2.27
13	J213009.21+001734.1	322.5383587	0.2928049	0.395	0.070	0.133	0.10	0.12	0.71	1.79
14	J073247.97+313543.0	113.1998808	31.5955501	0.398	0.096	0.190	0.16	0.13	0.64	2.00
15	J172037.03+264035.7	260.1542920	26.6765741	0.401	0.130	0.206	0.12	0.12	0.67	3.67
16	J010613.11+010611.8	16.5546148	1.1032724	0.422	0.151	0.321	0.26	0.22	0.43	1.42
17	J084218.36+361351.9	130.5764959	36.2310866	0.426	0.052	0.101	0.00	0.00	0.00	1.24
18	J142616.99+380300.7	216.5707949	38.0501829	0.485	0.084	0.140	0.10	0.08	0.27	1.06
19	J083024.02+654246.6	127.6000689	65.7129349	0.491	0.055	0.095	0.09	0.07	0.26	1.05
20	J133509.26+404231.0	203.7885645	40.7088843	0.588	0.034	0.075	0.14	0.20	0.30	1.08
21	J145637.74+221632.2	224.1572603	22.2756202	0.595	0.051	0.102	0.12	0.14	0.85	3.08
22	J084326.25+293932.9	130.8593818	29.6591364	0.607	0.051	0.097	0.09	0.07	0.60	1.73
23	J084336.83+292502.9	130.9034782	29.4174803	0.611	0.076	0.135	0.00	0.00	0.00	1.05
24	J084323.35+293828.7	130.8472787	29.6412927	0.623	0.041	0.078	0.06	0.04	0.66	2.47
25	J142636.50+374921.3	216.6520843	37.8225701	0.649	0.067	0.120	0.11	0.10	0.51	1.19
26	J083229.03+654710.6	128.1209420	65.7862700	0.730	0.009	0.023	0.03	0.05	0.32	1.71
27	J024713.00−033745.1	41.8041692	−3.6291907	0.173	0.229	0.302	0.18	0.17	0.84	1.04
28	J172057.08+263051.4	260.2378232	26.5142879	0.187	0.862	1.009	0.48	0.44	1.46	3.27
29	J145733.19+221450.1	224.3883064	22.2472405	0.532	0.137	0.278	0.20	0.15	0.52	1.97
30	J133455.26+410724.7	203.7302636	41.1235413	0.633	0.068	0.131	0.17	0.14	0.31	1.36

data (4) or are sufficiently compact that no further morphological information can be derived. Most of the rest (38) are early-type spirals, lenticular galaxies, or elliptical galaxies. Only 5 are probable interacting systems, although a few of the ellipticals and lenticular galaxies also show hints of distortion and interaction. Therefore the majority of the AGNs reside in normal-appearing spheroidal and bulge-dominated galaxies. This result is consistent with the results of Pović et al. (2012) for a sample of X-ray-selected AGNs at $z < 2.0$ and with those reported by Villforth et al. (2014) for the CANDELS fields at $z \sim 0.7$.

4.3. Type-2 SED Decomposition

The Type-2 AGN sample does not extend to $z > 0.8$ because the critical emission lines move outside the range of our spectra; in fact, from the trend of detections with redshift, the sample becomes progressively less complete above $z = 0.6$. The sample includes many more galaxies at low redshift ($z < 0.3$) than for the Type-1 sample. Many of these low-redshift galaxies appear to be dominated by star formation at 24 μm, with AGNs both of relatively low luminosity (because of the low redshift) and, by themselves, not as bright as 1 mJy at 24 μm. To make these statements quantitative, we need to carry out the decomposition of the SEDs. Only then can we determine which sources can be compared directly with the members of the Type-1 sample.

4.3.1. Decomposition Approach

For both the individual *Herschel*-detected sources and the stacked results, we use SED decomposition to disentangle the AGN and star formation contribution in the FIR. Based on the arguments in Sections 3.2.3 and 3.3, we assume that star formation dominates the signals in the *Herschel* bands. Specifically, we model the observed SED as a linear sum of a stellar component, a star formation component, and an AGN component. We use Levenberg–Marquardt least-squares fitting to find the best stellar, star formation, and AGN templates and their normalizations.

The stellar population and FIR star-forming galaxy templates were identical to those used with the Type-1 sources. The *GALEX* data show UV excess emission in the majority of the Type-2 AGNs that cannot be produced by an old stellar population. This enhanced blue color is also reported in Sánchez et al. (2004) for early-type AGN hosts at $0.5 < z < 1.1$. SDSS images of Seyfert 2 galaxies at $z < 0.2$ show UV emission from young stars in the outer regions of the host galaxies (Kauffmann et al. 2007). Because the stellar-population SEDs did not allow for two distinct episodes of star formation widely separated in time, we added SEDs for a second population of very young UV-bright galaxies of age 0.1–1.0 Gyr to fit the UV emission.

The strong extinction associated with Type-2 nuclei makes it impossible to use a single template to fit their SEDs. We employ the numerical AGN templates from Fritz et al. (2006), which include cases with heavy absorption. These models assume a central point-like energy source with a broken power-law SED

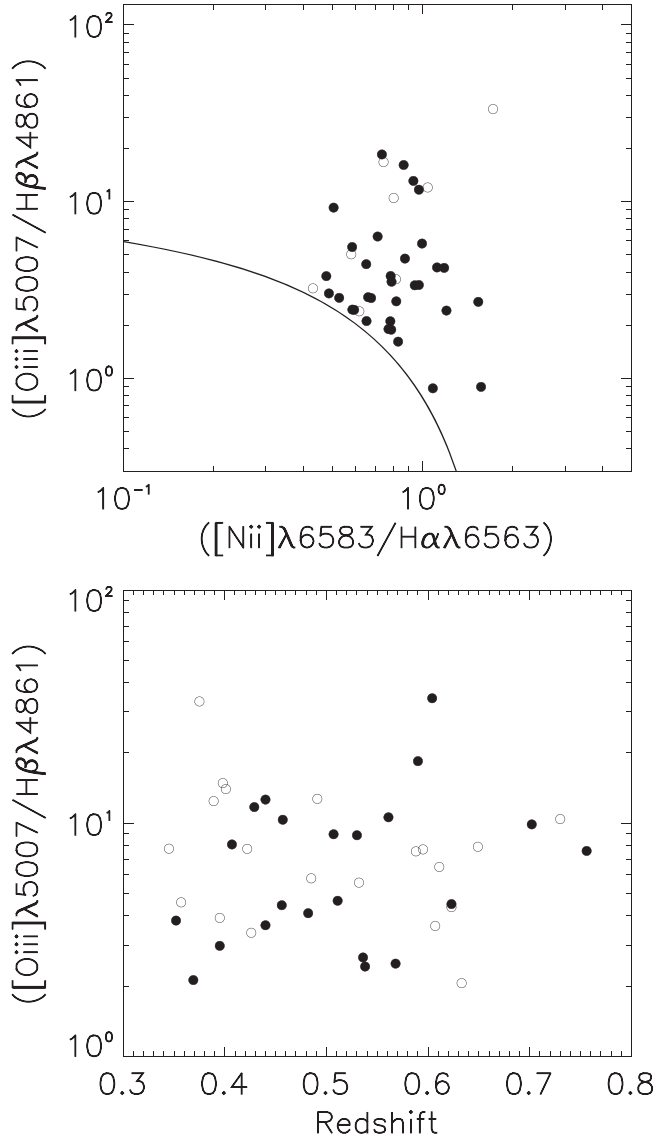

Figure 12. Upper: emission-line diagnostic diagram for sources at $z < 0.34$ taken from Kewley et al. (2001) (Equation (2)). Filled circles are *Herschel*-detected Type-2 AGNs. Unfilled circles are *Herschel*-non-detected Type-2 AGNs. Lower: the distribution of [O III]λ 5007/Hβ as a function of redshift for AGNs with $z > 0.34$.

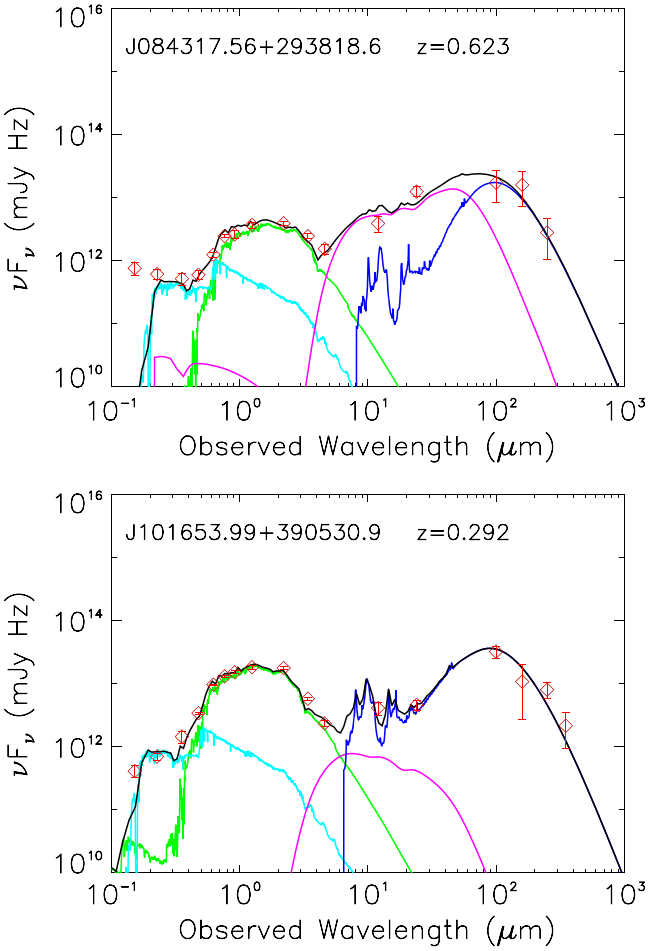

Figure 13. Examples of SED decomposition fits. Upper: SED dominated at 24 μm by the AGN. Lower: SED dominated at 24 μm by star formation. The cyan, green, magenta, and blue solid lines represent the best-fitting young stellar component, old stellar component, AGN component, and starburst component, respectively. The black solid line represents the total of the best-fitting models.

surrounded by a smooth dust distribution, and then solve the radiative transfer equation. Templates generated using this method depend on the dust distribution geometry and composition, and the inclination of the torus toward the observer. We put constraints on the AGN template library based on observations of the Seyfert 2 galaxy silicate 9.7 μm absorption features, for which it is found that $(F_f - F_c)/F_c > -0.85$, where F_f and F_c are the observed flux density and underlying continuum flux density at the minimum of the silicate absorption feature, respectively (Shi et al. 2006). Therefore, we do not use AGN templates with silicate 9.7 μm absorption $(F_f - F_c)/F_c < -0.85$. For comparison, Nenkova et al. (2008) have calculated models for clumpy dust distributions; the comparison of smooth and clumpy dust models in Feltre et al. (2012) shows that, although the two types of model give different outputs, for our purposes they are equivalent. For example, the Nenkova et al. (2008) models limit the silicate absorption depth, which we did also by imposing an additional constraint on those of Fritz et al. (2006).

Samples of the deconvolutions are illustrated in Figures 13 and 14. Table 8 lists the derived parameters for all 55 *Herschel*-detected sources.

4.3.2. Relative Roles of Star Formation and AGNs at 24 μm

All of the Type-1 AGNs are dominated by emission by the AGN at 24 μm (including the four at $z < 0.3$).[12] We classify a Type-2 AGN as AGN-dominated if the flux arising from the AGN component at 24 μm is larger than that from the SF component; otherwise, it is defined as 24 μm SF-dominated. Figure 13 shows examples of these two classifications. There are 17 AGN-dominated and *Herschel*-detected Type-2 galaxies, about 1/3 of the *Herschel*-detected sample. There is an approximate divide in this behavior at $z \sim 0.3$. Above this redshift, there are 50 Type-2 galaxies in our sample, of which 37 (74%) are dominated (or tied) by emission by the

[12] In some cases, the warm component is dominant. The origin of this component is not known, but it appears to be unique to AGNs.

Table 8
Redshifts and Derived Parameters for the *Herschel*-detected Type-2 Sources

#	Source LIRAS	z	$L_{\rm tot,IR}$ ($10^{11}L_{\odot}$)	$L_{\rm SB,IR}$ ($10^{11}L_{\odot}$)	$L_{\rm AGN,IR}$ ($10^{11}L_{\odot}$)	$L_{\rm AGN,total}$ ($10^{11}L_{\odot}$)	$M*$ ($10^{11}M_{\odot}$)	Type[d]
1	J101756.90+390528.0	0.054	0.10	0.09	0.01	0.03	0.33	S
2	J101805.64+385009.7	0.067	0.21	0.21	0.00	0.03	0.77	S0/E
3	J145753.24+222422.7	0.109	0.13	0.13	0.00	0.01	0.76	C
4	J133250.99+501816.1	0.110	0.12	0.11	0.01	0.32	0.31	S0/E
5	J083713.49+150037.4	0.141	0.23	0.22	0.01	0.13	0.80	E
6	J080102.09+355132.2[b]	0.160	0.34	0.19	0.15	2.14	0.60	E
7	J133644.33+405854.9	0.169	0.30	0.23	0.08	0.32	1.00	S
8	J101623.97+385840.1	0.169	4.75	4.72	0.03	0.70	0.68	E
9	J172109.90+263455.1	0.170	0.67	0.60	0.06	0.78	0.55	I
10	J172022.13+263626.6[b]	0.172	0.35	0.24	0.10	1.67	0.63	S
11	J212928.92+000415.0	0.180	0.38	0.30	0.09	0.35	0.84	E
12	J133323.14+503028.2	0.197	0.52	0.51	0.01	0.31	0.37	S
13	J073313.08+313954.6	0.198	0.38	0.29	0.09	1.15	0.53	S0/E
14	J073133.58+314113.0	0.210	0.48	0.44	0.05	0.19	0.73	E
15	J172004.43+262701.2	0.228	1.05	0.95	0.10	2.22	1.6	E
16	J080128.61+355046.1[a,b]	0.231	2.00	1.84	0.16	2.82	0.83	I
17	J142511.92+374729.5	0.233	1.13	1.07	0.06	1.06	0.71	S0/E
18	J084213.26+363020.5	0.243	1.17	1.13	0.04	0.90	0.54	S
19	J131130.41-013216.1	0.244	0.99	0.85	0.14	0.70	0.64	E
20	J084339.40+292025.2	0.248	0.97	0.92	0.05	0.18	0.34	E
21	J082644.54+040705.4	0.262	1.59	1.48	0.11	2.20	1.2	S
22	J171957.79+264027.3[a,b]	0.263	1.75	0.59	1.17	8.11	1.7	E
23	J133428.33+502829.0	0.266	0.62	0.47	0.15	1.69	1.1	…
24	J101641.15+384703.4	0.269	1.84	1.78	0.06	1.13	0.48	S
25	J084209.68+293836.1	0.279	0.83	0.74	0.09	1.91	1.5	S
26	J133553.40+405459.2	0.282	1.32	1.18	0.15	0.59	1.5	S
27	J101653.99+390530.9	0.292	1.03	1.00	0.02	0.43	1.0	S
28	J212914.75+001947.6	0.306	0.92	0.86	0.06	1.09	1.3	…
29	J073322.45+313915.5[b]	0.307	0.99	0.80	0.19	0.99	1.1	E
30	J010625.81+005343.3	0.313	1.09	1.03	0.06	1.30	1.6	E
31	J010658.45+010146.8	0.314	0.63	0.52	0.11	0.44	0.45	E
32	J010658.95+010438.3[a,b,c]	0.327	0.95	0.82	0.13	2.35	0.66	S0/E
33	J090016.83+205502.9	0.333	3.27	3.06	0.21	2.44	1.6	E
34	J090034.67+204013.2[a,b,c]	0.352	1.59	1.02	0.57	12.53	1.3	E
35	J101805.93+385755.8[a,c]	0.369	10.15	9.64	0.51	8.89		E
36	J213007.49+001419.1[a,b,c]	0.395	2.37	2.02	0.35	4.12	1.2	S0/E
37	J101742.86+385540.9[b]	0.407	1.32	1.04	0.28	1.13	0.84	E
38	J024858.24-032446.9[a,b,c]	0.429	2.45	1.86	0.59	2.43	1.0	…
39	J133241.05+502502.9	0.440	4.76	4.23	0.53	2.15	3.2	E
40	J101800.18+385833.5[a,b,c]	0.440	5.84	3.83	2.00	8.22	1.4	I
41	J083759.22+145557.1	0.456	2.57	2.25	0.32	1.31	1.0	E
42	J083244.18+654251.5[a,b,c]	0.457	4.33	1.97	2.35	9.60	0.92	C
43	J073258.91+313724.5	0.482	3.65	3.54	0.11	1.98	0.62	…
44	J171919.29+262835.3	0.507	9.70	9.27	0.42	2.87	1.9	E
45	J080049.66+360514.2[a,b,c]	0.511	3.95	3.26	0.69	12.12	1.0	C
46	J133616.50+405529.4	0.530	2.38	1.51	0.87	3.11	0.60	C
47	J101714.14+390124.4[a,b,c]	0.536	1.96	0.89	1.07	18.72	2.8	I
48	J101600.54+391049.3	0.538	4.88	4.78	0.10	2.07	2.6	I
49	J213011.84+000558.3[a,b,c]	0.561	4.62	2.33	2.28	9.35	1.5	E
50	J082927.84+654906.5[a,b,c]	0.568	4.14	3.98	0.16	2.76	0.74	C
51	J145635.24+222400.9[a,b,c]	0.590	3.95	3.09	0.86	4.77	1.8	C
52	J213015.48+000430.0[a,b,c]	0.604	7.43	6.57	0.85	4.43	1.2	C
53	J084317.56+293818.6[a,b,c]	0.623	5.21	2.77	2.44	12.56	1.3	E
54	J015214.76+010705.7[a,b,c]	0.702	15.12	12.96	2.16	11.22	2.1	C
55	J090126.15+205632.1	0.756	10.37	10.26	0.11	1.95	1.8	E

Notes.
[a] High-luminosity subsample (HLS).
[b] AGN-dominated at 24 μm.
[c] Comparison Sample (see text).
[d] S = spiral, E = elliptical, C = too compact to classify, I = interacting.

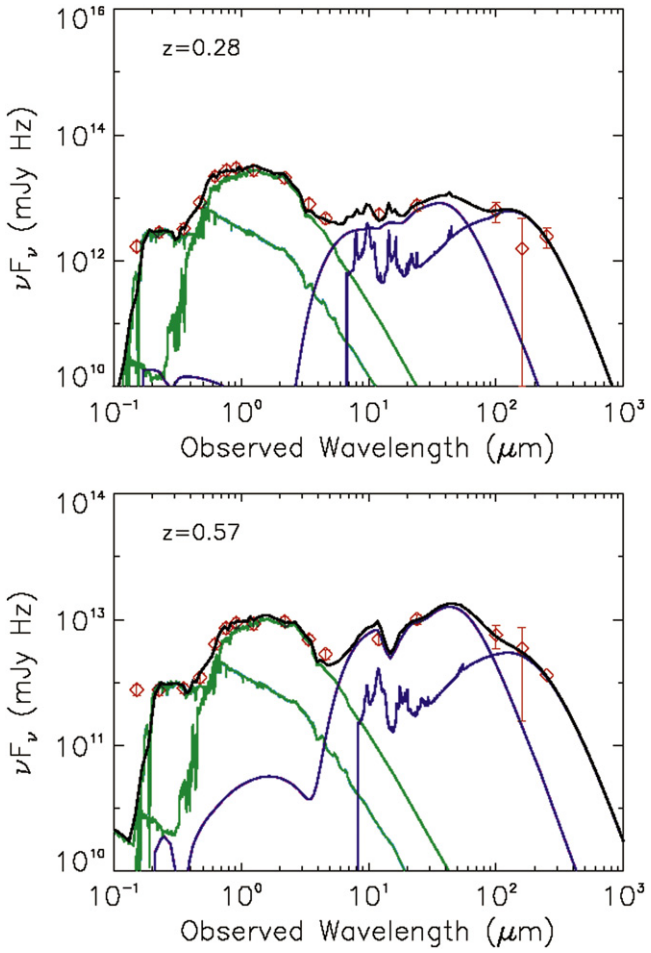

Figure 14. Average SEDs for Type-2 AGNs with no formal FIR detections in our sample in two discrete redshift bins: $z = 0.0$–0.4 (upper, 14 sources), and 0.4–0.8 (lower, 13 sources). Symbols and line colors are the same as in Figure 13.

AGN over that from star formation at 24 μm. (We include the *Herschel*-non-detected galaxies in this sample, since normalizing a star-forming template to the *Herschel* upper limits shows all of these to be AGN-dominated.) However, for the 35 cases at $z < 0.3$, only 13 (37%) are AGN-dominated at 24 μm (including the *Herschel*-non-detected cases). In Section 3 we showed that selection at 24 μm yielded a large number of Type-1 AGNs; it appears that for $z > 0.3$, selection at this wavelength is useful to generate candidate lists that are relatively unbiased in terms of AGN type (see also Mateos et al. 2013).

Because the 24 μm selection works relatively well at $z > 0.3$ in finding the most luminous AGN, we use it to compare the incidence of Type-1 and Type-2 sources. There are 50 Type-1 AGN with $0.3 < z < 0.8$ in the 5.2 square degrees surveyed for them; normalizing by surveyed area, we expect 35 in the 3.6 square degrees surveyed for Type-2 sources. In fact, we have found 37 dominant Type-2 sources. That is, the numbers of Type-1 and Type-2 quasars in this redshift range are similar. This result confirms the conclusion of Reyes et al. (2008), but with the initial selection on a completely different basis than the extinction-corrected [O III] luminosity used in that work.

4.4. Definition of the High-Luminosity and Comparison Samples

4.4.1. Sample Definition

We now derive a subsample of Type-2 objects suitable for comparison with the Type-1 AGNs. The Type-1 sources are very luminous, with massive black holes (77/91 = 85% have $M_{\rm BH} \geqslant 1 \times 10^8\ M_\odot$) and accreting at rates close to Eddington (66/70 = 94% at $\geqslant$3% of the Eddington rate).[13] To compare with them, we need to define a suitable sample of the Seyfert 2 AGNs, namely those indicated to have $M_{\rm BH} \geqslant 1 \times 10^8\ M_\odot$ and that are accreting at a minimum of 3% of the Eddington rate, leading to a minimum bolometric AGN luminosity of $10^{11}\ L_\odot$. We describe these objects as the high-luminosity sample (HLS) as indicated in Table 8. The HLS consists of 17 objects, all but two at $z > 0.3$. All but four of the 107 *Herschel*-detected Type-1 galaxies are also at $z > 0.3$. Yan et al. (2013) show that the incidence of star-forming galaxies bright enough to be within our 24 μm selection is low at $z > 0.3$, simplifying the task of identifying AGNs. Therefore, for the primary comparison sample with the Type-1 objects, we require $z > 0.3$; the 15 members of this sample are also flagged in Table 8.

Not surprisingly since both metrics emphasize high AGN luminosity, 13/17 of the AGN-dominated sources also belong to the HLS. By definition, the 15 sources in the Comparison Sample are all members of the HLS, but the Comparison Sample also includes 14/17 of the AGN-dominated examples. Thus, the various methods for isolating the most luminous AGNs largely overlap. However, because its membership is not linked to the host SFR and its threshold AGN IR luminosity is matched to that in the Type-1 sample, the Comparison Sample is best suited to complement the Type-1 sample.

4.4.2. Possible Biases in the Comparison Sample

The members of the Comparison Sample virtually all fall in the range where we identified the AGNs by the ratio of [O III] and Hβ line fluxes. We now consider the reliability of this identification procedure. Figure 15 shows the correlation between the line luminosity, $L_{\rm O\,III}$, and the AGN total luminosity, the latter from our SED decomposition. The two luminosities correlate as $L_{\rm AGN} \propto L_{\rm O\,III}^{0.74}$, even though it is generally believed that the strength of the [O III] line should be proportional to AGN luminosity. At the higher end of the redshift range, sources have higher $L_{\rm O\,III}$ than pure proportionality predicts. Since $L_{\rm O\,III}$ traces ionizing photons that can be created by star formation as well as AGNs, one possible reason for the $L_{\rm O\,III}$ excess at higher redshift is that the FOV of the fiber of the spectrograph includes significant amounts of [O III] emission from star formation in the host galaxy, as discussed further in Xu et al. (2015).

The possibility, particularly at high redshifts, that our [O III] measurements are contaminated by the host galaxies could result in a bias against AGNs in host galaxies with very strong star formation, since they might be expected to have reduced ratios of [O III] to Hβ and thus miss our selection criteria. However, we believe this is not a problem for a number of reasons. First, we have searched for candidate contaminated systems at $z > 0.34$ through the entire spectroscopic sample, by identifying galaxies with [O III]

[13] The denominators for both of these percentages are based on the number of objects with suitable measurements and do not represent the entire sample.

FWHM > 400 km s^{-1}, 1.5 < [O III]/Hβ < 2 (corresponding to 0.176 < log([O III]/Hβ) < 0.3, below the selection threshold in Equation (3)), and 24 μm flux density >1 mJy. Because all of our candidate galaxies have masses $>3 \times 10^{10} M_{\odot}$, this selection procedure would have identified all Type-2 AGN in our stellar mass range that would satisfy the MeX criteria (see Figure 4(c) in Juneau et al. 2011). We found only one candidate. This low yield is consistent with our only identifying five out of our sample of Type-2 AGNs above $z = 0.3$ with [O III]/Hβ between 2 and 3; it appears that our initial 24 μm selection generally yields AGNs with relatively large [O III]/Hβ. This result suggests that there are very few candidates that might have missed identification as Type-2 AGNs because of contamination. The low yield with a relaxed log([O III]/Hβ) threshold also indicates that the Type-2 sample is nearly complete to an AGN flux density of 1 mJy, at least for $z > 0.3$.

Second, consistent with this conclusion, if contamination were introducing significant biases, one would expect that the *Herschel*-detected systems would have a tendency to have low values of [O III]/Hβ because they have relatively strong star formation, but the lower panel of Figure 12 does not show a strong effect.

Third, it appears that our AGN samples include all potential contaminated galaxies. We have determined that the ratio of [O III] to 24 μm flux density is roughly the same or slightly higher for AGNs compared with star-forming galaxies.[14] In addition, the value of [O III]/Hβ intrinsic to AGNs is often significantly higher than our adopted theshold of 2. As an example, for the sample compiled by LaMassa et al. (2010), the median ratio is 9, while the sample of Juneau et al. (2011) has a typical ratio of 4. Taken together these results show that any host galaxy containing an AGN with an intrinsic flux density $\geqslant$1 mJy at 24 μm (i.e., above the luminosity threshold for our AGN samples) plus star formation sufficiently vigorous to contaminate the [O III]/Hβ ratio enough to cause it to fall below our threshold would have a total signal at 24 μm well above 1 mJy. However, above 2 mJy, the AGNs in our samples count for all of the detections, leaving no room for a population of luminous AGNs in very luminous star-forming galaxies.

Figure 15 is not the first finding of a departure from the expected 1:1 relation between [O III] and bolometric AGN luminosity in the direction of an increasing [O III] lluminosity for more luminous AGNs. LaMassa et al. (2010) found similar behavior relative to 12 μm luminosities; Shao et al. (2013) also saw this behavior when comparing the [O III] and 22 μm luminosities for a large sample of AGNs from the Sloan Digital Sky Survey; and Hainline et al. (2013) report a similar departure from a 1:1 relation using 8 μm luminosity as an indicator of AGN luminosity. However, Shao et al. (2013) show a 1:1 relation between [O III] and 4.6 μm luminosity. Taken together these results imply discrepancies in measuring the AGN luminosities from different single-color IR bands. It is therefore of interest that we find the effect based on the bolometric AGN luminosity, rather than an estimate of the luminosity based on a single spectral band.

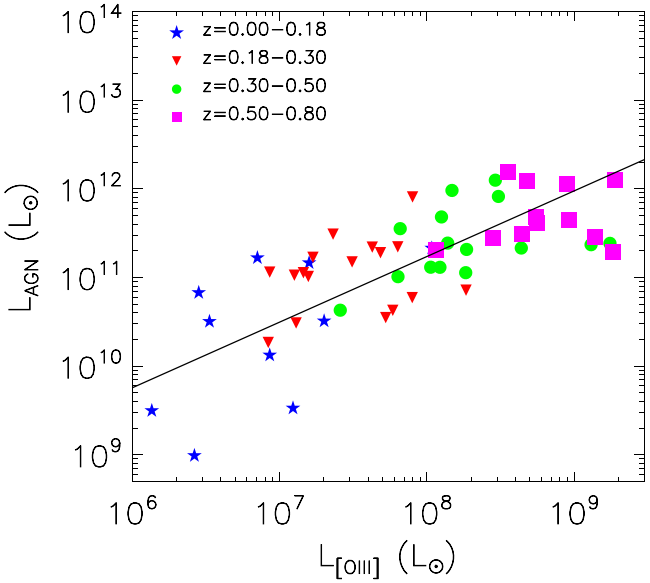

Figure 15. Relation between AGN total luminosity and [O III] λ5007 luminosity for *Herschel*-detected Type-2 AGNs in our sample. The fitted line (all points with equal weights) has a slope of 0.74.

5. INTRINSIC PROPERTIES

With the SED decompositions, along with other derived properties of the sources (e.g., line widths), we now derive the basic physical parameters of the sources in our sample.

5.1. IR Luminosities and Star Formation Rates

The SED decomposition disentangles the contributions from different source components. The IR luminosity from the star formation component ($L_{\rm SF,IR}$) is integrated over the rest-frame 8–1000 μm range of the best-fit star formation template. The IR luminosity from the AGN component ($L_{\rm AGN,IR}$) is integrated over the same range of the rescaled AGN template.[15] By integrating the full Elvis template, we set the total AGN luminosity of the Type-1 objects to be 5.28 times their IR luminosities. The Type-2 AGN bolometric luminosities are taken to be the rescaled total intrinsic luminosity of the best-fit

[14] For AGNs, we used the sample from Diamond-Stanic et al. (2009; nuclear 24 μm flux densities were provided by A. Diamond-Stanic 2015, private communication). We found an average value for the flux in [O III] (in aW) over the flux density at 24 μm (in Jy) of 513 ± 80 (492 ± 69 for Type-2 AGNs and 548 ± 118 for Type-1). For star-forming galaxies, we utilized the MIPS 24 μm measurements and the "radial strip" line results for the SINGS sample (Dale et al. 2005; Moustakas et al. 2010) to find a ratio of 457 ± 114 and the integrated galaxy spectra from Moustakas & Kennicutt (2006) with IRAS 25 μm data to obtain 426 ± 15. We have also used the "radial strip" spectra from Moustakas et al. (2010) for galaxies with $M_V < -20$ to find an average value of [O III]/Hβ = 0.98 for luminous star-forming galaxies. Relaxing the luminosity threshold to $M_V < -19$ has little effect: the average is then 1.03, so the value is not strongly sensitive to galaxy luminosity (and the accompanying range of relevant metallicity, based on the luminosity–metallicity relation). Caputi et al. (2008) find a similar average ratio, while the work of Moustakas & Kennicutt (2006) yields a value of 0.82, again in good agreement.

[15] The calculated luminosities are uncertain for a number of reasons, such as: (1) the underlying assumption that the emission by the central engine is isotropic, despite its complex geometry and optical depth (e.g., Koratkar & Blaes 1999); (2) the contamination of the AGN template in the FIR by star formation (see Appendix C); and (3) the inclusion of *both* the optical–UV–X-ray and the IR components of the SED (Marconi et al. 2004). It is difficult to make quantitative estimates of these effects, but other than the first, they appear to be modest (i.e., < a factor of 2 for the second two together, see Marconi et al. 2004 and Appendix C).

AGN template for each source.[16] The total IR luminosity ($L_{\rm IR}$) is the sum of $L_{\rm SF,IR}$ and $L_{\rm AGN,IR}$. The star formation fraction ($F_{\rm SF}$) is defined as $L_{\rm SF,IR}/L_{\rm IR}$. Of the *Herschel*-detected Type-1 sources, 21% have $F_{\rm SF} > 75\%$, 47% have $50\% < F_{\rm SF} < 75\%$, and 32% have $F_{\rm SF} < 50\%$. The corresponding values for the Type-2 Comparison Sample are $(60 \pm 20)\%$, $(27 \pm 13)\%$, and $(13 \pm 10)\%$, similar within the poor statistical weights of the latter (particularly allowing for the lower typical redshifts of the Type-2 objects). The star formation fractions of the stacked SEDs of *Herschel*-non-detected Type-1 AGNs (in three discrete redshift bins: $z = 0.1$–0.7, 0.7–1.2, and 1.2–1.9) are all below 40%.

The SFRs are calculated from $L_{\rm SF,IR}$ using the relation in Kennicutt (1998), adjusted for a "diet" Salpeter IMF (Bell et al. 2003) from the original Salpeter IMF, i.e.,

$$\frac{\rm SFR}{M_\odot\ {\rm yr}^{-1}} = 1.2 \times 10^{-10}\left(\frac{L_{\rm SF,IR}}{L_\odot}\right). \quad (4)$$

The adopted IMF reduces the proportion of low-mass stars to resemble, for example, the Kroupa IMF, and puts the SFRs on the same scale as our mass estimates in the following section. $L_{\rm SF,IR}$ ranges from $\sim 10^{10}$ to $3 \times 10^{12}\,L_\odot$ for the *Herschel*-detected galaxies; the average value for the stacked SEDs of the non-detected galaxies is several times lower. Nonetheless, star formation activity must be common even for the AGN hosts not individually detected by *Herschel*. However, as for the local sample of Palomar–Green (PG) quasars (Shi et al. 2014), it is possible that there are a number of quiescent galaxies among those we stacked, and therefore that elevated star formation is not ubiquitous.

5.2. Virial Black Hole Masses and Eddington Ratios

Type-1 AGN black hole masses, $M_\bullet$, have been measured directly by reverberation mapping (Blandford & McKee 1982; Peterson 1993; Kaspi et al. 2000), but it takes years to obtain results using this technique. However, reverberation mapping has also provided empirical scaling relations allowing us to estimate black hole virial masses efficiently from the quasar continuum luminosity and broad emission line widths, e.g., Hβ (4861 Å), Mg II (2800 Å), and C IV (1549 Å). We used the moderate resolution (~6 Å, corresponding to 300–400 km s^{-1}) Hectospec spectra to determine the FWHM of the broad emission lines. We followed the procedures in Vestergaard & Wilkes (2001) (for Mg II) and Peterson et al. (2004) (for Hβ and C IV) to fit these lines and measure the FWHM of the broad component. We took the mass-scaling relationship from Vestergaard & Peterson (2006; for Hβ and C IV) and from Vestergaard & Osmer (2009; for Mg II) to estimate black hole masses. In Appendix D, we list the three mass-scaling relationships we used, and show three examples of fitting results for Mg II, C IV, and Hβ, respectively.[17] The measured FWHMs and estimated BH masses are listed in Table 5.

[16] Uncertainties for them include: (1) the differences between clumpy and smooth models (Feltre et al. 2012); (2) in our fitting, the torus opening angle is poorly constrained; (3) variability; and (4) the underlying assumption that the emission by the central engine is isotropic, despite its complex geometry and optical depth (e.g., Koratkar & Blaes 1999).

[17] If both Hβ and Mg II are available, we adopt Hβ; and if both Mg II and C IV are available, we adopt Mg II.

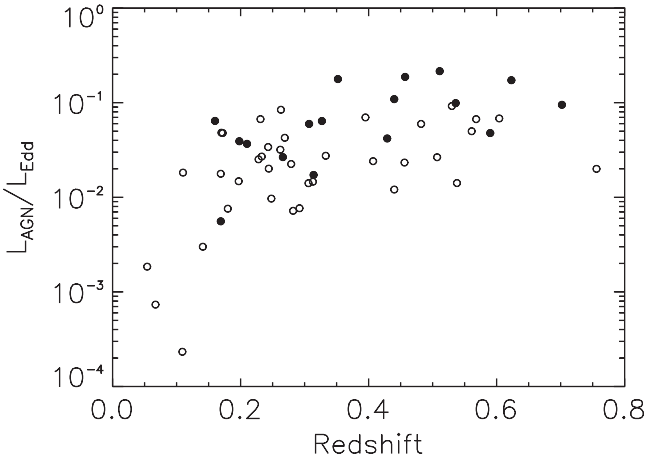

Figure 16. Ratio of AGN luminosity to Eddington luminosity for our Type-2 AGNs. Filled circles are for AGN-dominated sources, while open ones are for SF-dominated.

The Eddington luminosity from a black hole with mass $M_\bullet$ powered by spherical accretion is

$$L_{\rm E} = \left(\frac{4\pi G c m_p}{\sigma_e}\right) M_\bullet. \quad (5)$$

We obtained the AGN total luminosity from the SED decomposition, and calculated the ratio of AGN luminosity to Eddington luminosity. Of the Type-1 AGN, 94% emit at $\gtrapprox 3\%$ of the Eddington limit. The distribution of the bolometric luminosity as a fraction of the Eddington limit is consistent with that of the SDSS quasars (McLure & Dunlop 2004).

Assuming the local stellar mass (M_*) and black hole mass ($M_\bullet$) correlation (i.e., $M_* \approx 700 M_\bullet$; e.g., Bennert et al. 2011; Cisternas et al. 2011; Scott et al. 2013), we calculate the black hole masses, Eddington luminosities, and Eddington ratios of the Type-2 AGNs, with results shown in Figure 16. The 24 μm SF-dominated Type-2 AGNs have slightly lower ratios than the AGN-dominated ones at all redshifts. The 24 μm AGN-dominated Type-2 galaxies emit close to 10% of the Eddington rate (14/17, or 82% emit at $\gtrapprox 3\%$ of the Eddington rate); for $z > 0.3$, their behavior is similar to that of the Type-1 AGNs. Therefore, as expected (e.g., by the unified model), the behavior of the nuclei of the 24 μm AGN-dominated Type-2 galaxies is consistent with that of the Type-1 sample. The lower Eddington ratios in the star formation-dominated galaxies are expected, given that they have not been selected strictly on AGN luminosity.

5.3. Stellar Masses of AGN Host Galaxies

5.3.1. Stellar Masses from SEDs

Based on the SED decomposition, we can estimate the host galaxy stellar masses. Because the details of the stellar spectrum are difficult to disentangle from the AGN emission, we base the mass estimate on the NIR stellar luminosity, which has been shown to be an accurate approach (e.g., McGaugh & Schombert 2014). We use the relation between stellar mass, M_*, and K-band luminosity, L_k, for local field galaxies (Bell et al. 2003): $(\log_{10}(M_*/L_k) = -0.42 + 0.033 \log_{10}(M_c h^2/M_\odot)$,

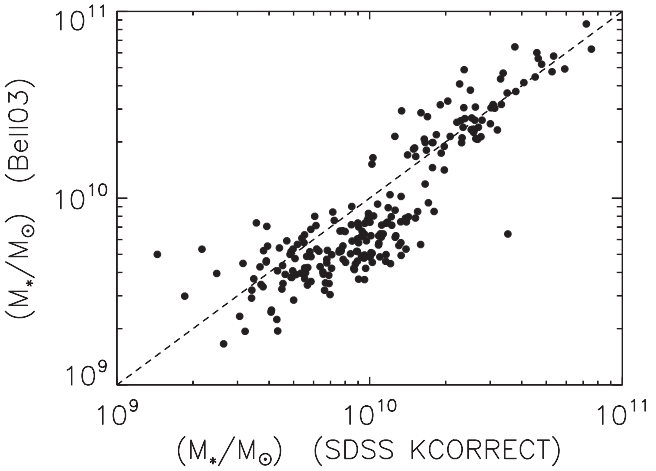

Figure 17. Comparison of the stellar mass calculated from Bell et al. (2003) and SDSS KCORRECT (K. Tyler 2015, private communication). The SDSS KCORRECT stellar masses are based on the Bruzual–Charlot stellar evolution synthesis. The stellar masses derived from Bell et al. (2003) are consistent with those from SDSS KCORRECT.

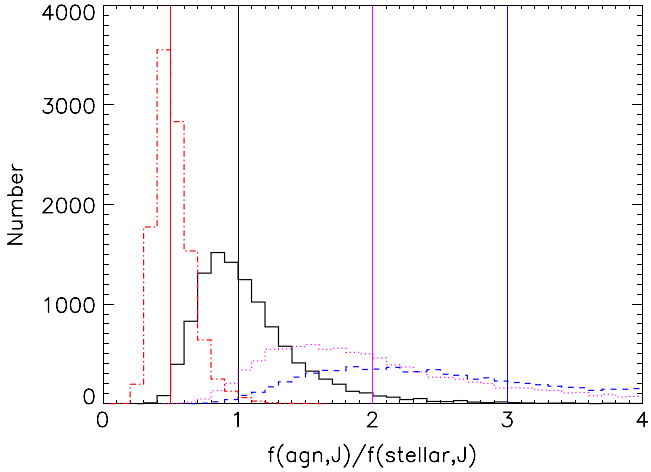

Figure 18. Simulation results for the ability of SED decomposition to constrain the stellar component in the NIR. The simulation is performed 10,000 times for each fixed value of AGN and stellar component in the rest-frame J-band. The derived results for the input flux ratio $\mathrm{flux}_{\mathrm{AGN},J}/\mathrm{flux}_{\mathrm{Stellar},J} = 0.5$, 1, 2, and 3, are shown in red dash–dotted, black solid, magenta dotted, and blue dashed lines.

where $M_c h^2$ is 10.63 averaged over all galaxy types (10.61 for early-type galaxies and 10.48 for late-type galaxies). The masses assume a "diet" IMF, defined by Bell et al. (2003). We need to be sure that our mass estimates are on a consistent scale with other approaches. This would be straightforward if the host galaxies were normal early types, but many of them have anomalously blue colors (e.g., Floyd et al. 2013). We therefore compare with a wide range of masses that include galaxies with a range of colors. We find that the masses are consistent with those using SDSS KCORRECT (Blanton & Roweis 2007)[18] for local galaxies (K. Tyler 2015, private communication; see Figure 17). Although photometrically determined masses can be subject to significant systematic errors, the agreement on average between our approach and the masses derived from full photometry puts our masses on the same scale as, e.g., those of Elbaz et al. (2011) and allows direct comparison of the host galaxy behavior in our sample with the field galaxy behavior described in that paper. The stellar component in the Type-2 galaxies is more accessible to our fitting than for the Type-1 cases, and we could attempt more detailed models. However, for consistency in comparing the samples, we use the same approach. We obtain the estimates of stellar mass in Table 8. Our AGNs reside in very massive galaxies with stellar masses around $10^{11}\,M_\odot$.

As a stellar population ages, its luminosity declines as its more massive stars die; i.e., a fixed K-band luminosity corresponds to smaller stellar mass at higher redshift. This passive evolution must be accounted for in estimating the masses of the stellar populations in high-redshift galaxies (e.g., Drory et al. 2003, 2004; van der Wel et al. 2006; also see van Dokkum & Franx 2001). We assume the AGN host galaxies evolve passively and follow van der Wel et al. (2006) to correct for this systematic evolution of the host stellar luminosity (i.e., $\Delta \ln (M_*/L_K) = (-1.18 \pm 0.10)z$). This correction can be applied to galaxies from the local epoch to $z \sim 1.2$, where the correction factor is equal to 4.1. For $z \sim 1.2-2$, we keep the value of the correction factor at 4.1.

Since the rest-frame J-band is near both the peak of the stellar SED and a minimum of the AGN SED, we use this band to quantify the stellar component output. Our fits constrain the J-band flux from the stars well for most low-z sources, where the AGNs are of relatively low luminosity and do not dominate in the rest NIR. At higher redshifts, we can usually only obtain upper limits for the stellar fluxes. We ran a simulation to test to what level we can trust the stellar flux from the SED decomposition. First, we renormalized the stellar and AGN SED templates to the desired flux ratio in the rest-frame J-band. Second, we applied dust extinction selected randomly over the range $A_V = 0$–1.0 to the AGN template and then added the two templates. Third, we convolved the bandpass transmission curves with the combined templates to simulate the photometry that we used for the SED decomposition. We added random noise to the simulated photometry in all bands, assuming a standard deviation of 20% in consideration of the photometry errors, AGN variability, and that the data in different bands were probably taken in different years. Fourth, we ran the SED decomposition procedures on this simulated photometry and calculated the recovered flux ratio of the AGN and stellar components in the rest-frame J-band. The input flux ratio was set to six discrete values: $\mathrm{flux}_{\mathrm{AGN},J}/\mathrm{flux}_{\mathrm{Stellar},J} = 0.5$, 1, 2, 3, 4, 5, and the calculation was repeated 10,000 times for each value. We compare the input and recovered flux ratios in Figure 18. If the stellar flux is twice the AGN flux in J band, 99% of the sources can be recovered accurately. If the stellar flux is equal to the AGN flux in J band, there is a larger scatter of the recovered flux ratio, and on average the stellar mass is overestimated by about 20%. However, >95% of the sources are recovered within a factor of 2. If the stellar flux is below the AGN flux in J band, the errors in the stellar flux are large. Based on this result, if the rest-frame J-band flux of the stellar component is equal to or above that of the AGN component, we can compute a valid stellar mass. If the J-band flux of the stellar component is smaller than that of the AGN component,

[18] Also see http://howdy.physics.nyu.edu/index.php/Kcorrect. The SDSS KCORRECT stellar mass is based on the Bruzual–Charlot stellar evolution synthesis and makes use of the multiband SDSS photometry.

we use the J-band flux of the AGN component to assign an upper limit to the mass of the stellar component.

The $J - K$ colors of early-type galaxy stellar populations are very similar, so the rest-frame K-band luminosity can be taken to be 0.85 times the J-band luminosity. Therefore we use 0.85 times the stellar component J-band flux to compute stellar masses, or of the AGN component to estimate upper limits to stellar mass. We then obtain the estimates of AGN host stellar mass as tabulated in Table 5.

5.3.2. Indirect Determination of Stellar Masses

We now estimate stellar masses from the black hole–stellar bulge relation. These estimates allow us to

1. extend the study of AGN host galaxies to a significant number at $z > 1$
2. test the passive evolution assumed to correct our mass estimates from observed NIR fluxes
3. investigate the possible bias toward massive host galaxies because requiring them to be sufficiently bright in the NIR to outshine the AGNs for photometric mass estimation will favor ones with massive hosts, at least at high redshifts

To lay the foundation for indirect mass estimates, we: (1) examine the possible extent of evolution of $M_\bullet/M_*$ over the relevant redshift range, $0 < z \leqslant 1.8$; and (2) calibrate the masses derived from $M_\bullet$ against those from NIR luminosity obtained in the preceding section. These two steps let us determine the maximum plausible deviations of the derived stellar masses from a nominal "best estimate."

The great majority of luminous AGNs are in galaxies with early-type morphologies (e.g., McLeod & Rieke 1995; Floyd et al. 2004). For such galaxies, the local value of $M_\bullet/M_*$ is well determined for galaxies with $M_\bullet > 3 \times 10^7\ M_\odot$ (Kormendy & Ho 2013). The majority of our AGN samples with $z \geqslant 0.3$ have $M_\bullet$ above this threshold, within the range where $M_\bullet/M_*$ is well behaved.

Most investigators agree that, within the errors, there is little evolution in the $M_\bullet/M_*$ ratio from $z = 1$ to $z = 0$ (Peng et al. 2006a; Shen et al. 2008; Somerville 2009; Cisternas et al. 2011; Zhang et al. 2012; Salviander & Shields 2013; Salviander et al. 2015). A small number of studies suggest some evolution in this range but are inconclusive regarding its significance (Woo et al. 2008; Canalizo et al. 2012). We will assume that the local ratio holds up to $z \sim 1.2$. For z between 1 and 2, the indications range from very little evolution (Peng et al. 2006b; Jahnke et al. 2009; Somerville 2009; Sarria et al. 2010; Schulze & Wisotzki 2014) to evolution by a factor up to about four (at $z = 2$; Peng et al. 2006a; Decarli et al. 2010; Merloni et al. 2010; Trakhtenbrot & Netzer 2010; Bennert et al. 2011). Particularly at $z > 1$, there are selection effects that bias the apparent evolution upward, correction for which reduces it significantly, to a factor of 2 or less (Lauer et al. 2007; Shen & Kelly 2010; Schulze & Wisotzki 2011; Portinari et al. 2012).[19] However, these same selection effects, e.g., the bias due to luminosity selection toward relatively massive black holes (Lauer et al. 2007), may apply to our use of the $M_\bullet/M_*$ ratio to estimate stellar masses,[20] so for our sample we will consider the possible extreme value of $M_\bullet/M_*$ at $z = 1.8$ to be four times the local value.

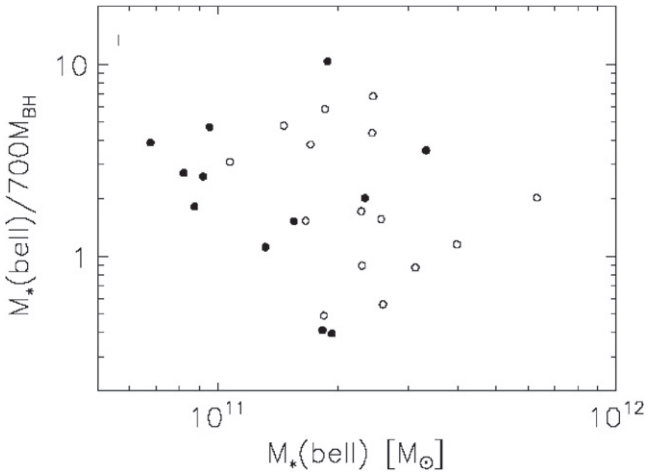

Figure 19. Comparison of the stellar masses estimated by K-band luminosity using the equation from Bell et al. (2003; see Section 6.4) and the stellar masses derived from the local mass ratio $M_*/M_\bullet = 700$. The filled and unfilled circles are AGNs at $z < 0.6$ and $0.6 < z < 1.2$, respectively.

To calibrate stellar masses from $M_\bullet/M_*$ against masses from NIR photometry, we assume the $M_\bullet/M_*$ relation has no evolution from the local value $M_* \approx 700M_\bullet$ up to $z \sim 1.2$ (e.g., Bennert et al. 2011; Cisternas et al. 2011; Scott et al. 2013). At $0 < z < 1.2$, there are 28 AGNs in our sample that have both $M_\bullet$ (derived from broad line width; see Section 5.2) and M_* (estimated via K-band luminosity). In Figure 19, we compare the K-band derived M_*s and those from $M_\bullet/M_*$. The large scatter is not surprising given the scatter in the σ–M relation (Kormendy & Ho 2013) and in the mass determinations from photometry (e.g., Shapley et al. 2001; Savaglio et al. 2005; Kannappan & Gawiser 2007), plus the additional uncertainties indicated by our simulation of the deconvolution uncertainties in NIR fluxes. The K-band derived M_* is on average two times higher than the bulge stellar masses predicted by the local $M_\bullet/M_*$ ratio. This offset is independent of redshift, which indicates that our correction for passive K-band evolution is roughly correct.[21]

The offset could arise if the galaxies have substantial disks, or if our photometric or BH masses have small systematic errors. However, there is also a selection bias toward relatively massive galaxies that have sufficiently bright NIR stellar fluxes to outshine their AGNs and allow mass estimates from their SEDs. Approximating this bias by assuming a normal intrinsic distribution with all of the cases with mass estimates from SED fits coming from the upper side indicates an offset by a factor of 1.7, in satisfactory agreement with what we find. Thus, the indirect stellar mass estimates serve the important function of removing this source of bias from our sample. The scatter is

[19] The factor of 2 is also consistent with the conclusion that half of the stellar mass observed today has formed since $z = 1.3$ (Madau & Dickinson 2014), assuming that any black hole growth over this period is negligible.

[20] See Matsuoka et al. (2014) for an example of about a two times bias for galaxies of similar mass to ours.

[21] One extreme outlier has been omitted; such outliers are also seen in other samples (Kormendy & Ho 2013).

0.38 dex rms.[22] We can estimate the intrinsic scatter in our NIR-based mass estimates of about 0.15 dex from Figure 17 corrected for the scatter in the masses with full photometric fits (Santini et al. 2015). If anything, 0.15 dex may be a low estimate (Courteau et al. 2014). We need to add the scatter due to having to measure the NIR fluxes from deconvolution of SEDs with significant contributions from the AGNs. The resulting total scatter is expected to be at least 0.2 dex. Subtracting this value quadratically from 0.38 dex, we estimate that the masses determined from $M_{\bullet}/M_{*}$ will have an intrinsic rms scatter of 0.32 dex. Given the uncertainties, we estimate the possible errors as 0.3 dex toward low values (from the rms scatter) but 0.6 dex toward high values above $z = 1.1$ (from possible evolution and/or selection effects), relative to the nominal values assuming the local $M_{\bullet}/M_{*}$ ratio. All the AGNs with stellar masses from photometry reside in very massive galaxies with stellar mass around 1–4 $\times 10^{11}\,M_{\odot}$. The masses estimated indirectly are also generally within this range.

6. SUMMARY

We studied the properties of a sample of 24 μm-selected, spectroscopically identified AGNs and their host galaxies, using a multiwavelength data set from *Chandra*, *GALEX*, SDSS, UKIRT, *WISE*, *Spitzer*/MIPS, and *Herschel*. Typical luminosities for these AGNs are above 10^{45} erg s^{-1} ($\sim 2 \times 10^{11} L_{\odot}$), and they generally lie between z of 0.3 and 2.5. We use SED decomposition from the optical to the FIR to estimate the AGN luminosities, SFRs, and stellar masses of the AGN hosts.

We summarize the results from this study as follows.

1. About 50% (107 out of 205) of the Type-1 AGNs in our sample are individually detected by *Herschel*. Among these AGNs, 68% show high levels of star formation (the star formation activity contributes over 50% in the FIR). *Herschel*-non-detected AGNs were studied using stacking analysis. On average, they have a similar level of AGN luminosity and similar optical colors, but the average star formation activity is several times lower than in AGNs individually detected by *Herschel*.
2. Similarly, about 65% (55 out of 85) of the Type-2 AGNs are individually detected by *Herschel*. However, these objects tend to be at relatively low redshift and some of the detections are a result of vigorous star formation, not nuclear activity. We have defined a sample of 15 Type-2 AGNs with properties ($M_{\rm BH}$, Eddington ratio, and redshift) that make them directly comparable with the Type-1 sample.
3. The FIR-detected Type-1 AGNs and matching Type-2 AGNs reside in massive galaxies ($\sim$1–2 $\times 10^{11}\,M_{\odot}$). They harbor SMBHs of $\sim 3 \times 10^{8}\,M_{\odot}$, which accrete at $\sim$10% of the Eddington luminosity.
4. A warm excess in the MIR was found for eight Type-1 AGNs compared with a local quasar template. This warm excess can be prominent at higher redshifts but is not seen in low-redshift quasars. It is not clear whether it changes due to evolution, or whether the warm excess is confined to very luminous quasars.
5. The 24 μm-selected sample of Type-1 AGNs includes about twice as many objects as are identified through the SDSS, including the majority of the SDSS identifications. The additional objects have redder optical colors than typical SDSS quasars, due to reddening or intrinsically red quasar continua.
6. As also found, e.g., by Hainline et al. (2013), the strength of the [O III]λ5007 line increases more rapidly than proportionately to bolometric AGN luminosity. At relatively high redshift (and hence high AGN luminosity), detection of [O III] emission from parts of the host galaxy within the spectrograph fiber may contribute to this effect.

These results are discussed further in Xu et al. (2015).

We thank Xiaohui Fan, Desika Narayanan, and Dan Stark for helpful discussions. Marianne Vestergaard provided template spectra and assisted us in spectral line fitting for black hole mass estimation. We also thank Yong Shi for communicating results on quasar aromatic band measurements in advance of publication. This work is based in part on observations made with *Herschel*, a European Space Agency Cornerstone Mission with significant participation by NASA. Additional observations were obtained with *Spitzer*, operated by JPL/Caltech. We acknowledge NASA funding for this project through an award for research with *Herschel* issued by JPL/Caltech. C.P.H. was funded by CONICYT Anillo project ACT-1122. G.P.S. acknowledges support from the Royal Society. Additional support was provided through contract 1255094 from JPL/Caltech to the University of Arizona. This paper also is based in part on work supported by the National Science Foundation under grant No. 1211349. Funding for the SDSS and SDSS-II has been provided by the Alfred P. Sloan Foundation, the Participating Institutions, the National Science Foundation, the U.S. Department of Energy, the National Aeronautics and Space Administration, the Japanese Monbukagakusho, the Max Planck Society, and the Higher Education Funding Council for England. The SDSS website is http://www.sdss.org/. The SDSS is managed by the Astrophysical Research Consortium for the Participating Institutions. The Participating Institutions are the American Museum of Natural History, Astrophysical Institute Potsdam, University of Basel, University of Cambridge, Case Western Reserve University, University of Chicago, Drexel University, Fermilab, the Institute for Advanced Study, the Japan Participation Group, Johns Hopkins University, the Joint Institute for Nuclear Astrophysics, the Kavli Institute for Particle Astrophysics and Cosmology, the Korean Scientist Group, the Chinese Academy of Sciences (LAMOST), Los Alamos National Laboratory, the Max-Planck-Institute for Astronomy (MPIA), the Max-Planck-Institute for Astrophysics (MPA), New Mexico State University, Ohio State University, University of Pittsburgh, University of Portsmouth, Princeton University, the United States Naval Observatory, and the University of Washington. This publication makes use of data products from the *Wide-field Infrared Survey Explorer*, which is a joint project of the University of California, Los Angeles, and the Jet Propulsion Laboratory/California Institute of Technology, funded by the National Aeronautics and Space Administration.

APPENDIX A
OPTICAL IMAGES

Figure 20 shows the optical images of the Type 2 host galaxies.

[22] This value is plausible given the expected errors in single-epoch black hole mass estimates found by Vestergaard & Peterson (2006), corrected for scatter in the reverberation mapping masses (Onken et al. 2004), or the single-epoch error limits estimated by Denney et al. (2009).

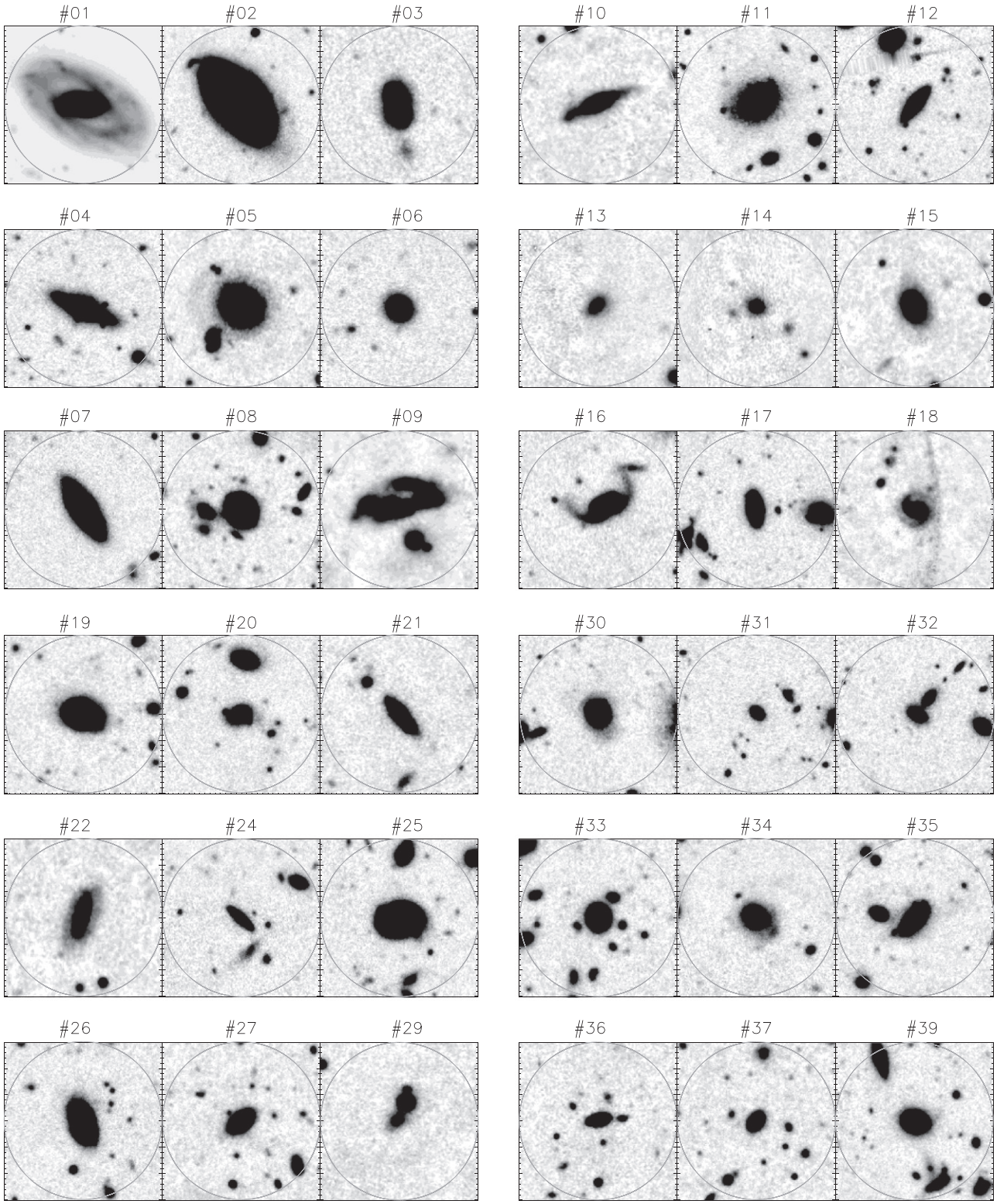

Figure 20. Subaru images of *Herschel*-detected Type-2 AGNs. The circle radius is 15″. The 1st part of a continued figure. Subaru images of *Herschel*-detected Type-2 AGNs. The circle radius is 15″. The second part of a continued figure.

APPENDIX B
24 μm-SELECTED TYPE-1 AGN SAMPLE IN THE LoCuSS FIELDS

In total, we detected 2439 sources with 24 μm flux above 1 mJy in the LoCuSS fields. Out of these, the following 541 sources were not included in the target list for the Hectospec spectroscopic follow-up:

1. 71 sources that were outside the available NIR images.
2. 168 sources that were identified as stars.

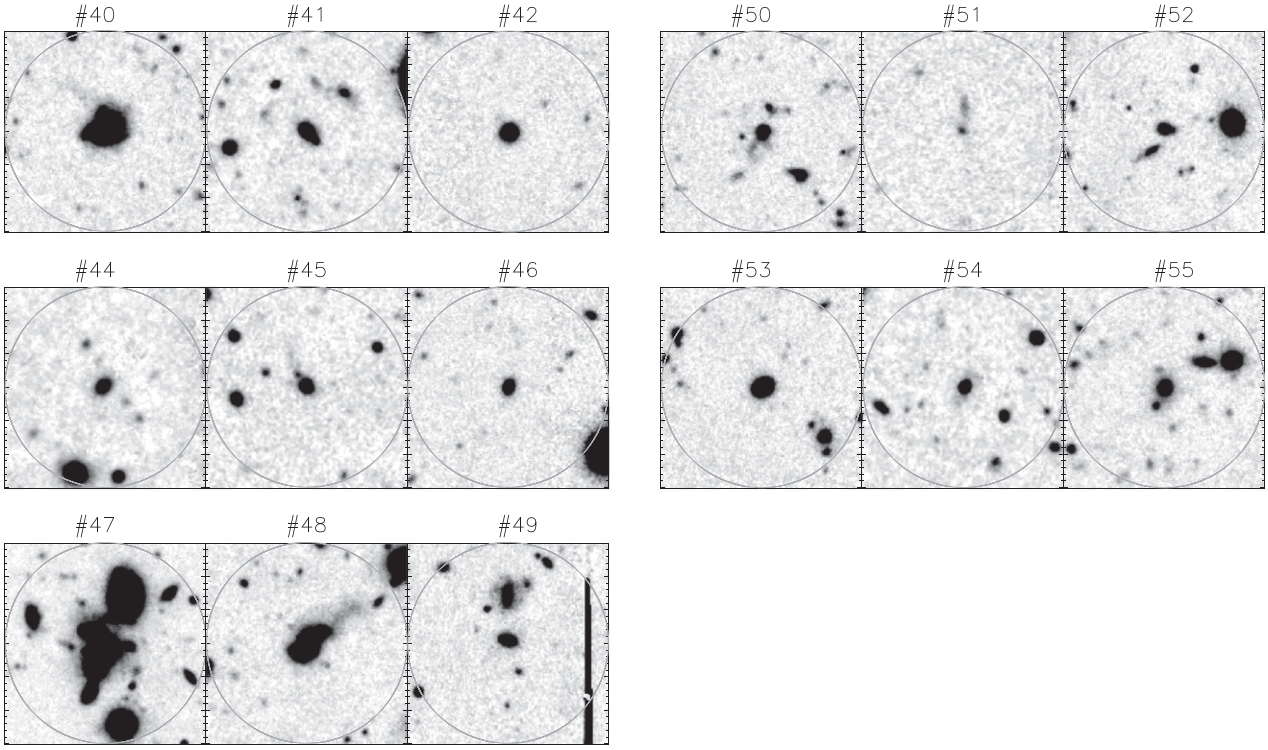

Figure 20. (Continued.)

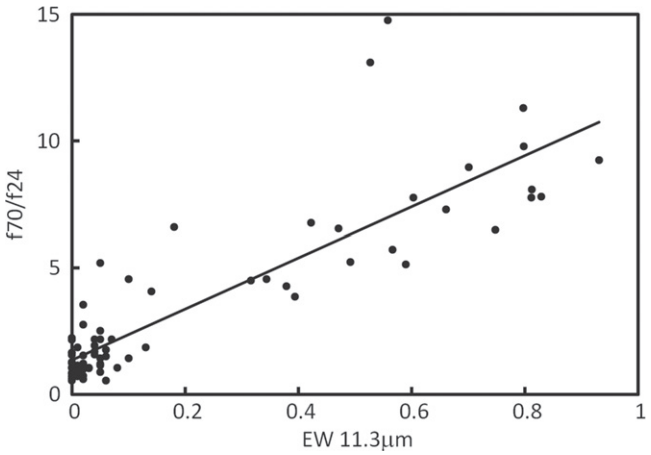

Figure 21. Relation between the equivalent width of the 11.3 μm aromatic feature and the ratio of flux densities at 70 and 24 μm (from MIPS) or at 60 and 25 μm (from IRAS, if MIPS measurements are not available). The data are from Shi et al. (2014) and Brandl et al. (2006).

3. 373 sources with no obvious optical/NIR counterparts. (The 5σ detection limit of the Subaru images in r or i band is ~25 mag and the 5σ detection limit at K-band is 19 mag (Vega).)

The remaining 1827 24 μm sources are likely to be extragalactic. We may have discarded a number of extragalactic sources with faint optical/NIR counterparts (category 3 above) although some fraction of the category 3 sources is expected to be asteroids.

Among these 1827 sources, 1729 were observed by Hectospec while another 18 sources have spectroscopic information from SDSS. The completeness of the spectroscopic coverage is therefore about 94.6%. Among the 1729 sources targeted by Hectospec, 1263 sources have produced spectroscopic redshifts with the corresponding success rate of 73%. However, the sources that did not produce spectroscopic redshifts are unlikely to be Type-1 AGNs. Therefore, our 24 μm-selected Type-1 AGN sample is expected to be complete at the ~94% level, which is the completeness of our spectroscopic coverage. Thus, we have 205 sources that satisfy our Type-1 AGN selection criteria (see Section 3), 177 confirmed with Hectospec spectra and 28 confirmed with SDSS spectra.

APPENDIX C
CORRECTION OF THE AGN TEMPLATE FOR STAR FORMATION

The template we use for the intrinsic AGN SED was built from a detailed set of observations of a representative set of optically selected quasars by Elvis et al. (1994). A more recent study by Richards et al. (2006) used a similar approach and derived a virtually identical template. The excellent agreement is encouraging; for example, our results are independent of which template we use. However, neither study attempted to correct the templates for the FIR emission due to star formation. Doing so is challenging because one needs an independent, extinction-free estimate of the rate of star formation in the quasar host galaxies. The 11.3 μm aromatic feature is an appropriate indicator, particularly since it is not strongly affected by an AGN (Diamond-Stanic & Rieke 2010). We have therefore used a large set of measurements of this feature in quasar spectra (Shi et al. 2014), along with a star-forming galaxy FIR template (Rieke et al. 2009) to estimate the necessary correction. The approach was to correlate the equivalent width of the 11.3 μm feature with the ratio of fluxes at 25 and 60 μm (IRAS) or at 24

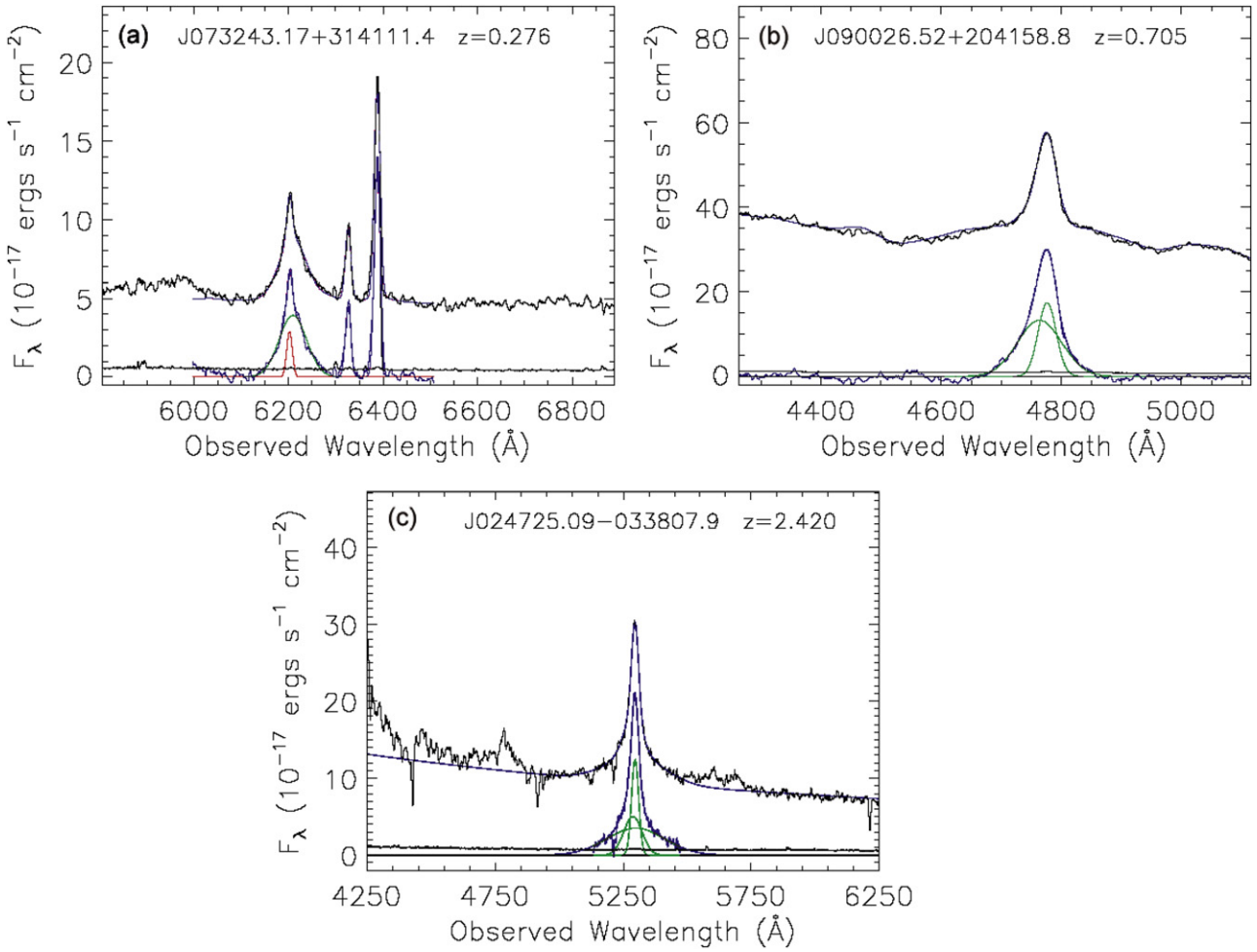

Figure 22. Examples of broad emission line fits. (a) Hβ; (b) Mg II; (c) C IV. For each panel, the upper black line shows the original SED. The lower blue line shows the continuum and Fe-subtracted SED. The upper magenta line shows the full fits; the lower magenta line shows the fits for the emission lines; the gray lines show the flux density errors; the green lines show the broad Gaussian components, while the red lines show the narrow Gaussian components.

and 70 μm (MIPS) to determine the influence of star formation on the FIR spectrum in a variety of galaxies with and without AGNs. We then used the relation derived from this correlation analysis and the average EW of the 11.3 μm feature for the quasar sample used by Elvis et al. (1994) to determine how to adjust their template in the FIR.

The initial template we used was for radio-quiet quasars; Elvis et al. (1994) list 19 of these sources with IRAS detections, and they would have been most influential in determining the FIR behavior of their template (we return to the IRAS upper limits later). Of those 19, we have 11.3 μm EW measurements for 15 (79%), with an average value of 0.037 μm (standard deviation of the mean = 0.007 μm). A linear fit to the dependence of EWs on IR flux ratios indicates that the ratio of IRAS 60–25 μm flux densities for the Elvis et al. (1994) template has been boosted by a factor of 1.24 due to star formation, relative to the case for an EW of 0.0. However, the baseline in EW is small, so we repeated the determination adding the galaxies from Brandl et al. (2006) (which we selected because the methodology for determining EWs was similar to the method for the quasars). This reference includes cases with EW up to ~0.9, thus extending the baseline and improving the determination of the slope of the relation. This fit indicated a star formation-induced boost in the FIR flux ratio for the Elvis template by a factor of 1.27. When we added the radio-loud quasars in the Elvis sample plus additional PG quasars with 11.3 μm and FIR measurements, and substituted MIPS for IRAS measurements when they were available, we got a value of 1.27. This last correlation is illustrated in Figure 21.

With a determination of the size of the star formation boost in the flux ratio, we subtracted a star-forming galaxy template (specifically for $L(\mathrm{TIR}) = 10^{11}\ L_\odot$, Rieke et al. 2009) from the Elvis AGN template. We used synthetic photometry on the f60/f25 flux density ratio to match the results from the correlation analysis based on the EW of the 11.3 μm feature.

The adjusted AGN template may be an extreme case, since we did not include the galaxies in the sample of Elvis et al. (1994) for which there were only IRAS upper limits. These galaxies should include those with the weakest star formation relative to the AGNs, as well as some that are just fainter than the detected ones at all wavelengths. It is not possible to reconstruct exactly what effect the upper limit cases would have had on the published template, but presumably they tended to make it fainter in the FIR than it would have been based only on the IRAS-detected cases. Thus, we consider our adjusted AGN template to be a limiting case for the maximum plausible FIR contribution from star formation, and take the

unadjusted template to be the limiting case in the other direction.

This approach provides a correction out to 100 μm (rest). Beyond this wavelength, the Elvis template is a power-law interpolation to the radio regime. There are very few examples of quasars that can be shown to have very low levels of star formation and at the same time have sufficiently sensitive measurements of upper limits at wavelengths longer than 100 μm. Two examples, PG 1501+106 and PG 1411+442, indicate that the power law substantially overestimates the fluxes in this region. Therefore, a more realistic replacement is a blackbody of 118 K, with a wavelength-dependent emissivity proportional to $\lambda^{-1.5}$ and scaled to match smoothly to the corrected SED at wavelengths short of 100 μm.

APPENDIX D
BLACK HOLE MASS ESTIMATE

The following methods were used to estimate black hole masses from our spectra:

1. FWHM(Hβ) and L_λ(5100 Å). For the optical continuum luminosity and FWHM of the Hβ broad component

$$\log\ M_{\rm BH}({\rm H}\beta) = \log\left[\left(\frac{\rm FWHM(H\beta)}{1000\ {\rm km\ s^{-1}}}\right)^2 \times \left(\frac{\lambda L_\lambda(5100\ {\rm \AA})}{10^{44}{\rm erg\ s^{-1}}}\right)^{0.50}\right] + (6.91 \pm 0.02). \quad (6)$$

   The sample standard deviation of the weighted average zero-point offset is ±0.43 dex (Vestergaard & Peterson 2006).
2. FWHM(Mg II). For a given wavelength, λ, the black hole mass based on Mg II was obtained according to

$$M_{\rm BH} = 10^{{\rm zp}(\lambda)}\left[\frac{\rm FWHM(Mg\ II)}{1000\ {\rm km\ s^{-1}}}\right]^2\left[\frac{\lambda L_\lambda}{10^{44}\ {\rm erg\ s^{-1}}}\right]^{0.5} \quad (7)$$

   where zp(λ) is 6.72, 6.79, 6.86, and 6.96 for λ1350, λ2100, λ3000, and λ5100 Å, respectively. The 1σ scatter in the absolute zero-points, zp, is 0.55 dex (Vestergaard & Osmer 2009).
3. FWHM(C IV) and L_λ(1350 Å). For the ultraviolet continuum luminosity and the FWHM of the C IV line

$$\log\ M_{\rm BH}({\rm C\ IV}) = \log\left[\left(\frac{\rm FWHM(C\ IV)}{1000\ {\rm km\ s^{-1}}}\right)^2\left(\frac{\lambda L_\lambda(1350\ {\rm \AA})}{10^{44}{\rm erg\ s^{-1}}}\right)^{0.53}\right] + (6.66 \pm 0.01). \quad (8)$$

   The sample standard deviation of the weighted average zero-point offset is ±0.36 dex (Vestergaard & Peterson 2006). The L_λ(1450 Å) luminosity is equivalent to L_λ(1350 Å) in the equation above without error or penalty in precision (Vestergaard & Peterson 2006).

Figure 22 shows the examples of broad emission line fits for Hβ, Mg II, and C IV.

REFERENCES

Ballantyne, D. R. 2008, ApJ, 685, 787
Ballantyne, D. R., Shi, Y., Rieke, G. H., Donley, J. L, Papovich, C., & Rigby, J. R. 2006, ApJ, 653, 1070
Bell, E. F., McIntosh, D. H., Katz, N., & Weinberg, M. D. 2003, ApJS, 149, 289
Bennert, V. N., Auger, M. W., Treu, T., Woo, J.-H., & Malkan, M. A. 2011, ApJ, 742, 107
Bertin, E., & Arnouts, S. 1996, A&AS, 117, 393
Blandford, R. D., & McKee, C. F. 1982, ApJ, 255, 419
Blanton, M. R., & Roweis, S. 2007, ApJ, 133, 734
Brand, K., Dey, A., Weedman, D., et al. 2006, ApJ, 644, 143
Brandl, B. R., Bernard-Salas, J., Spoon, H. W. W., et al. 2006, ApJ, 653, 1129
Brotherton, M. S. 1996, ApJS, 102, 1
Bruzual, G., & Charlot, S. 2003, MNRAS, 344, 1000
Canalizo, G., Wold, M., Hiner, K. D., et al. 2012, ApJ, 760, 38
Caputi, K. I., Lilly, S. J., Aussel, H., et al. 2008, ApJ, 680, 939
Cardamone, C. N., Urry, C. M., Damen, M., et al. 2008, ApJ, 680, 130
Casali, M., Adamson, A., Alves de Oliveira, C., et al. 2007, A&A, 467, 777
Cisternas, M., Jahnke, K., Bongiorno, A., et al. 2011, ApJL, 741, 11
Courteau, S., Cappellari, M., de Jong, R. S., et al. 2014, RvMP, 86, 47
Czerny, B., Li, J., Loska, Z., & Szczerba, R. 2004, MNRAS, 348, 54
Dale, D. A., Bendo, G. J., Engelbracht, C. W., et al. 2005, ApJ, 633, 857
Decarli, R., Falomo, R., Treves, A., Labita, M., Lotilainen, J. K., & Scarpa, R. 2010, MNRAS, 402, 2453
Denney, K. D., Peterson, P. M., Dietrich, M., Vestergaard, M., & Bentz, M. C. 2009, ApJ, 692, 246
Dey, A., Soifer, B. T., Desai, V., et al. 2008, ApJ, 677, 943
Diamond-Stanic, A., & Rieke, G. 2010, ApJ, 724, 140
Diamond-Stanic, A. M., Rieke, G. H., & Rigby, J. R. 2009, ApJ, 698, 623
Dicken, D., Tadhunter, C., Morganti, R., et al. 2008, ApJ, 678, 712
Donley, J. L., Rieke, G. H., Pérez-González, P. G., & Barro, G. 2008, ApJ, 687, 111
Drory, N., Bender, R., Feulner, G., et al. 2003, ApJ, 595, 698
Drory, N., Bender, R., Feulner, G., et al. 2004, ApJ, 608, 742
Dunne, L., & Eales, S. A. 2001, MNRAS, 327, 694
Elbaz, D., Dickinson, M., Hwang, H. S., et al. 2011, A&A, 533, 119
Elvis, M., Wilkes, B. J., McDowell, J. C., et al. 1994, ApJS, 95, 1
Fabricant, D., Fata, R., Roll, J., et al. 2005, PASP, 117, 1411
Feltre, A., Hatziminaoglou, E., Fritz, J., & Franceschini, A. 2012, MNRAS, 426, 120
Floyd, D. J. E., Dunlop, J. S., Kukula, M. J., et al. 2013, MNRAS, 429, 2
Floyd, D. J. E., Kukula, M. J., Dunlop, J. S., et al. 2004, MNRAS, 355, 196
Fritz, J., Franceschini, A., & Hatziminaoglou, E. 2006, MNRAS, 366, 767
Gaskell, C. M., Goosmann, R. W., Antonucci, R. R., & Whysong, D. H. 2004, ApJ, 616, 147
Gordon, K. D., Clayton, G. C., Misselt, K. A., et al. 2003, ApJ, 594, 279
Gordon, K. D., Rieke, G. H., Engelbracht, C. W., et al. 2005, PASP, 117, 503
Gordon, K. D., Galliano, F., Hony, S., et al. 2010, A&A, 518L, 89
Griffin, M. J., Abergel, A., Abreu, A., et al. 2010, A&A, 518, L3
Haas, M., Klaas, U., Müller, S. A. H., et al. 2003, A&A, 402, 87
Haines, C. P., Smith, G. P., Egami, E., et al. 2009, ApJ, 704, 126
Haines, C. P., Pereira, M. J., Sanderson, A. J. R., et al. 2012, ApJ, 754, 97
Haines, C. P., Pereira, M. J., Smith, G. P., et al. 2013, ApJ, 775, 126
Haines, C. P., Pereira, M. J., Smith, G. P., et al. 2015, ApJ, 806, 101
Hainline, K. N., Hickox, R., Greene, J. E., Myers, A. D., & Zakamska, N. L. 2013, ApJ, 774, 145
Hao, L., Spoon, H. W. W., Sloan, G. C., et al. 2005, ApJL, 625, L75
Hatziminaoglou, E., Omont, A., Stevens, J. A., et al. 2010, A&A, 518, 33
Hildebrand, R. H. 1983, QJRAS, 24, 267
Hopkins, P. F., Strauss, M. A., Hall, P. B., et al. 2004, AJ, 128, 1112
Hwang, H. S., Elbaz, D., Magdis, G., et al. 2010, MNRAS, 409, 75
Jahnke, K., Bongiorno, A., Brusa, M., et al. 2009, ApJL, 706, 215
Juneau, S., Dickinson, M., Alexander, D. M., & Salim, S. 2011, ApJ, 736, 104
Kannappan, S. J., & Gawiser, E. 2007, ApJL, 657, 5
Kaspi, S., Smith, P. S., Netzer, H., Maoz, D., Jannuzi, B. T., & Giveon, U. 2000, ApJ, 533, 631
Kauffmann, G., Heckman, T. M., Tremonti, C., et al. 2003, MNRAS, 346, 1055
Kauffmann, G., Heckman, T. M., Budavari, T., et al. 2007, ApJS, 173, 357
Kennicutt, R. C., Jr. 1998, ARA&A, 36, 189
Kenter, A., Murray, S. S., Forman, W. R., et al. 2005, ApJS, 161, 9
Kewley, L. J., Dopita, M. A., Sutherland, R. S., Heisler, C. A., & Trevena, J. 2001, ApJ, 556, 121
Koratkar, A., & Blaes, O. 1999, PASP, 111, 1

Kormendy, J., & Ho, L. C. 2013, ARA&A, 51, 511
Krawczyk, C. M., Richards, G. T., Mehta, S. S., et al. 2013, ApJS, 206, 4
LaMassa, S. M., Heckman, T. M., Ptak, A., Martins, L., Wild, V., & Sonnentrucker, P. 2010, ApJ, 720, 786
Lauer, T. R., Tremaine, S., Richstone, D., & Faber, S. M. 2007, ApJ, 670, 249
Lawrence, A., Warren, S. J., Almaini, O., et al. 2007, MNRAS, 379, 1599
Leipski, C., Meisenheimer, K., Walter, F., et al. 2013, ApJ, 772, 103
Leipski, C., Meisenheimer, K., Walter, F., et al. 2014, ApJ, 785, 154
Lusso, E., Comastri, A., Simmons, B. D., et al. 2012, MNRAS, 425, 623
Madau, P., & Dickinson, M. 2014, ARA&A, 52, 415
Magorrian, J., Tremaine, S., Richstone, D., et al. 1998, AJ, 115, 2285
Marconi, A., Risaliti, G., Gilli, R., et al. 2004, MNRAS, 351, 169
Mateos, S., Alonso-Herrero, A., Carrera, F. J., Blain, A., Severgnini, P., Caccianiga, A, & Ruiz, A. 2013, MNRAS, 434, 941
Matsuoka, Y., Strauss, M. A., Price, T. N., III, & DeDonato, M. S. 2014, ApJ, 780, 162
McGaugh, S. S., & Schombert, J. M. 2014, AJ, 148, 77
McLeod, K. K., & Rieke, G. H. 1995, ApJL, 454, 77
McLure, R. J., & Dunlop, R. S. 2004, MNRAS, 352, 1390
Merloni, A., Bongiorno, A., Bolzonella, M., et al. 2010, ApJ, 708, 137
Moustakas, J., & Kennicutt, R. C. 2006, ApJS, 164, 81
Moustakas, J., Kennicutt, R. C., Jr., Tremonti, C. A., Dale, D. A., Smith, J.-D. T., & Calzetti, D. 2010, ApJS, 190, 233
Mullaney, J. R., Alexander, D. M., Goulding, A. D., & Hickox, R. C. 2011, MNRAS, 414, 1082
Mullaney, J. R., Pannella, M., Daddi., E., et al. 2012, MNRAS, 419, 95
Nenkova, M., Sirocky, M. M., Ivezic, Z., & Elitzur, M. 2008, ApJ, 685, 147
Okabe, N., Takada, M., Umetsu, K., Futamase, T., & Smith, G. P. 2010, PASJ, 62, 811
Okabe, N., & Umetsu, K. 2008, PASJ, 60, 345
Omont, A., Cox, P., Bertoldi, F., McMahon, R. G., Carilli, C., & Isaak, K. G. 2001, A&A, 374, 371
Onken, C. A., Ferrarese, M., Peterson, E., Pogge, B. M., Vestergaard, R. W., & Wandel, A., M. 2004, ApJ, 615, 645
Ott, S. 2010, in ASP Conf. Ser. 434, Astronomical Data Analysis Software and Systems XIX, ed. Y. Mizumoto, K.-I. Morita & M. Ohishi (San Francisco, CA: ASP), 139
Peng, C. Y., Impey, C. D., Ho, L. C., Barton, E. J., & Rix, H.-W. 2006a, ApJ, 640, 616
Peng, C. Y., Impey, C. D., Rix, H.-W., et al. 2006b, ApJ, 649, 114
Peterson, B. M. 1993, PASP, 105, 247
Peterson, P. M., Ferrarese, L., Gilbert, K. M., et al. 2004, ApJ, 613, 682
Pilbratt, G. L. A., Riedinger, J. R., Passvogel, T., et al. 2010, A&A, 518, L1
Poglitsch, A., Waelkens, C., Geis, N., et al. 2010, A&A, 518, L2
Polletta, M., Courvoisier, T. J.-L., Hooper, E., & Wilkes, B. J. 2000, A&A, 362, 75
Portinari, L., Kotilainen, J., Falomo, R., & Decarli, R. 2012, MNRAS, 420, 732
Pović, M., Sanchez-Portal, M., Perez Garcia, A. M., et al. 2012, A&A, 541, 118
Reyes, R., Zakamska, N. L., Strauss, M. A., et al. 2008, AJ, 136, 2373
Richards, G., Fan, X., Newberg, H. J., et al. 2002, AJ, 123, 2945
Richards, G., Hall, P. B., Vanden Berk, D. E., et al. 2003, AJ, 126, 1131
Richards, G., Lacy, M., Storrie-Lombardi, L. J., et al. 2006, ApJS, 166, 470
Rieke, G. H. 1978, ApJ, 226, 550
Rieke, G. H., & Lebofsky, M. J. 1985, ApJ, 288, 618
Rieke, G. H., Young, E. T., Engelbracht, C. W., et al. 2004, ApJS, 154, 25
Rieke, G. H., Alonso-Herrero, A., Weiner, B. J., et al. 2009, ApJ, 692, 556
Rosario, D. J., Trakhtenbrot, B., Lutz, D, et al. 2013, A&A, 560, 72
Rujopakarn, W., Rieke, G. H., Weiner, B. J., et al. 2013, ApJ, 767, 73
Sajina, A., Yan, L., Fadda, D., Dasyra, K., & Huynh, M. 2012, ApJ, 757, 13
Salviander, S., & Shields, G. A. 2013, ApJ, 764, 80
Salviander, S., Shields, G. A., & Bonning, E. S. 2015, ApJ, 799, 173
Sanderson, A. J. R., Edge, A. C., & Smith, G. P. 2009, MNRAS, 398, 1698
Sánchez, S. F., Jahnke, K., Wisotzki, L., et al. 2004, ApJ, 614, 586
Santini, P., Ferguson, H. C., Fontana, A., et al. 2015, ApJ, 801, 97
Sarria, J. E., Maiolino, R., La Franca, F., Pozzi, F., Fiore, F., Marconi, A., Vignali, C., & Comastri, A. 2010, A&A, 522L, 3
Savaglio, S., Glazebrook, K., Le Borgne, D., et al. 2005, ApJ, 635, 260
Schneider, D. P., Richards, G. T., Hall, P. B., et al. 2010, AJ, 139, 2360
Schulze, A., & Wisotzki, L. 2011, A&A, 535, 87
Schulze, A., & Wisotzki, L. 2014, MNRAS, 438, 3422
Scott, N., Graham, A. W., & Schombert, J. 2013, ApJ, 768, 76
Shao, L., Kauffmann, G., Li, C., Wang, J., & Hecikman, T. M. 2013, MNRAS, 436, 3451
Shao, L., Lutz, D., Nordon, R., et al. 2010, A&A, 518, L26
Shapley, A. E., Steidel, C. C., Adelberger, K. L., Dickinson, M., Giavalisco, M., & Pettini, M. 2001, ApJ, 562, 95
Shen, Y., & Kelly, B. C. 2010, ApJ, 713, 41
Shen, Y., Vanden Berk, D. E., Schneider, D. P., & Hall, P. B. 2008, AJ, 135, 928
Shi, Y., Rieke, G., Hines, D. C., et al. 2006, ApJ, 653, 127
Shi, Y., Rieke, G. H., Ogle, P. M., Su, K. Y. L., & Balog, Z. 2014, ApJS, 214, 23
Smith, G. P., Haines, C. P., Pereira, M. J., et al. 2010, A&A, 518L, 18
Somerville, R. S. 2009, MNRAS, 399, 1988
Stanway, E. R., Eldridge, J. J., Greis, S. M. L., Davies, L. J. M., Wilkins, S. M., & Bremer, M. N. 2014, MNRAS, 444, 3466
Symeonidis, M., Kartaltepe, J., Salvato, M., et al. 2013, MNRAS, 433, 1015
Thompson, T. A., Quataert, E., & Murray, N. 2005, ApJ, 630, 167
Trakhtenbrot, B., & Netzer, H. 2010, MNRAS, 406L, 35
Tremaine, S., Gebhardt, K., Bender, R., et al. 2002, ApJ, 574, 740
van Dokkum, P. G., & Franx, M. 2001, ApJ, 553, 90
van der Wel, A., Franx, M., van Dokkum, P. G., et al. 2006, ApJL, 636, L21
Vestergaard, M., & Osmer, P. 2009, ApJ, 699, 800
Vestergaard, M., & Peterson, B. 2006, ApJ, 641, 689
Vestergaard, M., & Wilkes, B. J. 2001, ApJS, 134, 1
Villforth, C., Hamann, F., Rosario, D. J., et al. 2014, MNRAS, 439, 3342
Werner, M. W., Roellig, T. L., Low, F. J., et al. 2004, ApJS, 154, 1
Woo, J.-H., Treu, T., Malkan, M. A., & Blandford, R. D. 2008, ApJ, 681, 925
Xu, L., Rieke, G. H., Egami, E., Haines, C. P., Pereira, M. J., & Smith, G. P. 2015, ApJ, 808, 159
Yan, L., Donoso, E., Tsai, C. W., et al. 2013, AJ, 145, 55
Yuan, F., & Narayan, R. 2014, ARA&A, 52, 529
Zakamska, N., Strauss, M. A., Krolik, J. H., et al. 2003, AJ, 126, 2125
Zakamska, N. L., Schmidt, G. D., Smith, P. S., et al. 2005, AJ, 129, 1212
Zhang, X., Lu, Y., & Yu, Q. 2012, ApJ, 761, 5